THE UNIVERSITY
of LIVERPOOL

Automatic Detection and Characterisation of Cylindrical Objects Using Ground Penetrating Radar

Sufyan Shihab

Thesis submitted in partial fulfillment
of the requirements for the degree of
Doctor of Philosophy
at
The University of Liverpool

March 2005

Abstract

In a typical GPR survey, a great amount of data is collected, while only a small percentage of this amount represents useful data (i.e target data). The targets of interest sought in this study are extended cylindrical objects such as pipes, cables, and tanks. The data processing which rely heavily on a skilled operator, involve a number of stages starting with pre-processing of the data followed by detecting the areas that are thought to contain targets, and then making a final interpretation of these targets and their related information such as depth, dimensions, orientation, and dielectric constant of the medium. Each one of these stages consumes considerable amounts of time and effort, apart from the fact that the existence of the human factor is a source for inconsistency and error. This study automates these stages to a large extent via presenting a robust and consistent processing regime that would meet the increasing pace in the GPR industry.

The detection stage constitutes a consistent, highly accurate, and rapid procedure, which is based on a multi-stage neural classifier that uses a combination of first-order statistics and regional features to distinguish between the desired targets and other redundant data. As a result, the collected data is highly reduced and hence the processing domain is crucially narrowed for the subsequent stages. Image processing techniques are used to extract enhance the detected data and prepare it for further processing.

Furthermore, a novel general equation which models the GPR hyperbolic reflections resulting from buried cylinders is presented. It combines the effect of the radius, depth, and vertical and horizontal orientations of the buried cylinder, in addition to the dielectric constant of the medium. This overcomes the weakness of the existing

procedures followed to define such targets where broad assumptions are made. This model is used in conjunction with the a modified hyperbola-specific fitting procedure to accurately calculate target-related values of the radius, depth, vertical inclination and azimuthal orientation, in addition to the dielectric constant of the host medium.

In the final stage of the presented system, the information extracted from various cues from within the data are combined in a manner that minimises the reliance on ready-made assumptions, rules of thumb and conjecture. This stage combines the information extracted from individual radar images, in a novel and effective manner in which aligned points are sought in three-dimensional space via adaptive non-accumulative Hough Transform (ANHT). As a result, the orientations of the detected lines are found and used to correct for target information, from the previous stages, in an iterative procedure. Each stage of the presented system is successfully applied on field data and the results are presented and shown to correspond to the interpretation of a human expert. Furthermore, The full automatic procedure is applied to a synthetic site specially built for this purpose with all its parameters controlled, and the application result shows a high efficiency and accuracy in retrieving the original target-parameters in addition to the relative permittivity of the medium. The proposed system in this study constitutes the first comprehensive automatic procedure for buried cylinders detection and interpretation, and hence effectively contributes to the development of GPR industry.

Acknowledgements

I want to express my deep gratitude and appreciation to my supervisor Dr. Waleed Al-Nuaimy for providing me with the opportunity for this research, and for his continuous guidance, advice and encouragement. I am also grateful to Dr. Yi Huang for his continuous support and help throughout this project.

It is my pleasure to express my gratitude to Dr. Asger Eriksen of Zetica both for funding this project, and for his precious help and for providing his company's expertise and services. Thanks are also due to all the staff at the Department of Electrical Engineering and Electronics for their support and assistance. Special thanks are to my parents and to my wife without whose patience, encouragement and support none of this would have been possible.

Contents

List of Figures

List of Tables

Nomenclature

j_{bg}	Scan number corresponding to background clutter
$s(t)$	Analytic signal
$\sigma(s)$	Variance or the second moment of a signal $s(t)$
s_i	The i^{th} element in a vector s of length n
$\bar{s}$	The mean value of a vector s
MAD	Mean absolute deviation of a signal $s(t)$
m_4	Fourth moment of a signal $s(t)$
$R^2(p_1, p_2)$	Euclidean distances between the two points $p_1 = (x_1, y_1)$ and $p_2 = (x_2, y_2)$in a plane
$\text{STFT}_s^w(i,p)$	Short-time Fourier Transform of time series s using window w
$\text{SPEC}_s^w(i,p)$	Spectrogram of time series s using window w
$P(c)$	Periodogram power spectral density estimate
$S(c)$	Discrete Fourier Transform of time series
B	Number of Discrete Fourier Transform bins
b	Length of time series scan in samples
$W_s(t,f)$	Wigner-Ville distribution of time-series s
$R_s(\tau,t)$	Autocorrelation function of a signal $s(t)$
$D_s(f,t)$	Instantaneous spectral density function

$u(t)$	Real square-integrable signal in time
$v(t)$	The Hilbert transform of $u(t)$
$h(i)$	Pixel intensity distribution in an image
μ_h	Mean of the pixel intensity distribution in an image
N_h	The number of horizontal windows of size $x \times y$ across the image
N_v	The number of vertical windows of size $x \times y$ down the image
p	Fractional degree of overlap between windows
A_R	Area of a region
ED_R	Equivalent diameter of a region
$A_{rectangle}$	Area of the smallest rectangle containing a segmented region
R_k	The k^{th} region in an image that contain N regions
net	Neuron activation signal
w_i	Neuron input weight values
in_i	Neuron input values
out	Output value of neuron
f_{sig}	Logistic neuron transfer function
$f_{\tan}$	Hyperbolic tangent sigmoidal transfer function
T_p Rate	Classifier true positive rate
F_p Rate	Classifier false positive rate
F_n Rate	Classifier false negative rate
$\hat{t}$	The two-way travel time
$\hat{v}_s$	Velocity of propagation of GPR electromagnetic waves
z_0	Depth to the top of a buried cylinder
z	Apparent depth of the reflection from a buried cylinder at

	a position x displaced from the position of the cylinder x_0
R	Radius of a buried cylinder
e	Eccentricity of a hyperbola is the ratio between the focal length and the distance from the apex to the origin
n	Ratio between the horizontal offset part where the asymptotes of the two models intersect and the depth of the target
$\frac{R}{b}$	The radius-to-depth-to-centre ratio
α	Azimuthal orientation of a buried cylinder with respect to the direction of scanning
β	Vertical inclination of a buried cylinder with respect to the plane that contains the ground surface
γ	The angle that combines both α and β via the relation $\cos\gamma = \cos\alpha \cdot \cos\beta$
θ	Azimuth orientation angle in spherical coordinates and is related to α via: $\alpha = \theta - 90°$
ϕ	Vertical orientation angle in spherical coordinates and is related to β via: $\beta = 90° - \phi$
ϵ_r	Relative permittivity of the medium
ϵ_s	Relative permittivity of the soil or transmission medium
$F(\mathbf{m};\mathbf{x})$	An implicit second order polynomial representing a general conic
$\mathbf{D}$	The *design matrix* for the least-square hyperbola fitter
$\mathbf{S}$	The *scatter matrix* for the least-square hyperbola fitter
$\mathbf{C}$	The *constraint matrix* for the least-square hyperbola fitter
	Lagrange multiplier

ξ_x	Conversion constant to convert lateral distances
ξ_t	Conversion constant to convert travel time
ξ_v	Conversion constant to convert propagation velocity
c	Speed of electromagnetic propagation in free space
r	Position vector relative to the origin O
$\overrightarrow{l}$	Direction vector in spherical coordinates

Chapter 1

Introduction

Despite the rapid growth in the ground-penetrating radar (GPR) sector of the geophysical industry and the increasing demand for its use as a successful non-destructive testing tool, the post-processing procedures leading to the final interpretation are still plagued by major shortcomings. These shortcomings mainly emanate from factors such as the excessive reliance on human intervention, the scan-by-scan processing and interpretation of site data, and the host of broad assumptions that are often made regarding the nature and geometry of the targets.

In order to bring the GPR displays into a better condition that is suitable for interpretation, some pre-processing as well as post processing operations are carried out. Usually, these operations are manually handled by human operators, and consequently these would consume considerable amounts of time and effort. In addition, those operations are exposed to human inconsistency and error factor. To resolve this issue, it became necessary to find an automatic mechanism to carry out all the processing on the path of presenting the desired operation.

This study has the aim of producing an automated system that is capable of

detecting, characterising, mapping, and interpreting GPR data in near real-time. For this purpose, an automatic system is produced; it contains several stages in which pre-processed radar data are subjected to different processes leading towards the achievement of the goal of presenting a final interpretation report about the site under investigation and the related information to the detected targets.

1.1 Ground-Penetrating Radar (GPR)

Ground Penetrating Radar (GPR) provides an effective way to image the first few meters of the subsurface. The GPR is an electromagnetic technique ranging in the radio frequencies from 30 MHz to 2 GHz, its source is composed by a surface transmitter antenna emitting a series of electromagnetic pulses which propagate in the ground, then reflections of these pulses from the subsurface anomalies will be recorded by a receiving antenna. GPR has the potential of detecting a variety of metallic and non-metallic buried objects of different shapes. In addition, GPR provides reasonable resolution of the scanned-areas under various environmental conditions. As the GPR is advanced in the direction of travel, a 2-dimensional image of the scanned subsurface is generated (referred to as *B-scan*) with vertical and horizontal axes representing the two-way travel time and scan number. The radar returns that indicate the existence of objects are often overshadowed by artifacts due to the effects of the unwanted signals. The aim of object detection processes is to emphasise, detect, and recognise the desired signal while skipping unwanted signals.

These *B-Scans* or *radargrams* are complex and difficult to realise, thus these require expert interpretation. Much of the skill of the successful operator comes from combining observations drawn from the radar images, with knowledge of the host

medium, and the nature of the targets. Although this manual processing and interpreting of the scanned data is accompanied by limited automated processes, it consumes considerable amounts of time and effort, in addition to the problem of inconsistency resulted from human error factor specially when large volumes of data are involved.

Data processing implies separating out clutter, and accounting for various environmental, system and subsurface effects in order to perform the necessary analysis and arrive at the final interpretation. The processing aids which are used to aid in data interpretation typically involve either complex geophysical inversion algorithms, image processing, forward modelling or iterative migration, resulting in awkward and computationally expensive systems inadequate for on-site application.

In the particular case of buried cylindrical targets, this processing is normally based on making broad assumptions with regard to the radii of the cylinders, and both their horizontal and vertical orientations, in addition to the dielectric constant of the host medium. Consequently, this would result in an inaccurate system that cannot be trusted specially when the desired information requires high precision.

1.2 System Outline

The basic concept behind ground penetrating radar is that a transmitter is used to send electromagnetic energy into the ground that then reflects from geologic interfaces where a dielectric contrast exists. The reflected energy is recorded by a receiver and produces a picture of the reflected waves. Traces from adjacent source locations are generally plotted side-by-side to form a time-depth profile. GPR can be used with different antenna providing different frequencies, varying between 30 and 2000 MHz.

A lower frequency antenna provides greater penetration depths but lower resolution. A higher frequency antenna provides less depth penetration but has better resolution.

GPR has an enormously wide range of applications, ranging from planetary exploration to the detection of buried cylinders such as pipes and tanks. The selection of a range of frequency operations, a particular modulation scheme, and the type of antenna and its polarisation depends on a number of factors, including the size and shape of the target, the transmission properties of the intervening medium, and the operational requirements defined by the economics of the survey operation, as well as the characteristics of the surface. The specification of a particular type of system can be prepared by examining the various factors which influence detectibility and resolution.

To operate successfully, ground penetrating radar must achieve:

- Adequate signal to clutter ratio
- Adequate signal to noise ratio
- Adequate spatial resolution of the target, and
- Adequate depth resolution of the target

The radar system used in this study is the Geophysical Survey Systems Inc Surface Impulse Radar®System-2 shown in Figure 1.1 (see Appendix A for detailed specifications). The system comprises a digital control unit, the antennae mounted in a partially-shielded casing, a portable battery and a co-axial cable connecting the control unit and the antennae. The control unit is usually stationary and contains the transmitting and reception circuitry, and the computer which performs the on-line processing, display and storage.

The transmitter generates a low power (< 100 mW) 150 V pulse with a rise time of less than 2 ns [1]. The pulse repetition frequency is between 25 and 50 kHz, and the received waveform is sampled with a strobing or coherent sampling procedure whereby a single sample is taken from each waveform. It is therefore necessary to transmit an equivalent number of pulses as the number of samples per waveform to fully reconstruct the reflected signal.

The antennae used are typically twin dipole or bow-tie antennae with fractional bandwidth in the region of 100 %, i.e. possessing a centre frequency equal to the half-peak power bandwidth. The angular width of the main radiation lobe beneath the surface is approximately 90° from back to front (along the direction of movement) and 60° from side to side. The physical dimensions of the antenna casing and shielding vary; the 400 MHz antenna casing shown in Figure 1.1 is cuboid in shape, approximately 25 cm high and 40 cm each side. The 100 MHz antenna is larger, with the largest dimension 95 cm.

Figure 1.2 depicts a typical site survey scene with the SIR-2 digital control unit in the back of the van. Shown are the radar operator operating the digital control unit and recording relevant site information, and the survey practitioner towing the antenna along the survey lines delineated by painted grid markers. The radar survey is interrupted at certain stages and the partial digital data sets downloaded onto a portable computer. Interpretation experts are shown at the front of the van examining the results of preliminary on-site processing of this data, in order to obtain an immediate assessment of the subsurface environment. The success and effectiveness of the survey depends to a considerable extent on the speed and robustness of this on-site interpretation software, the two factors which form the focus of this study.

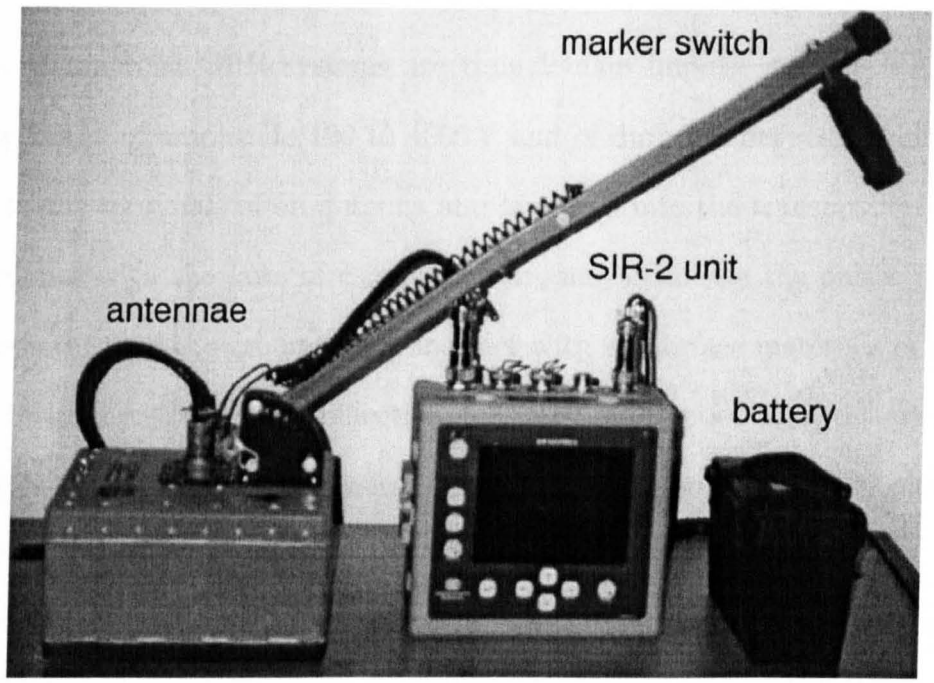

Figure 1.1: The GSSI Surface Impulse Radar System-2

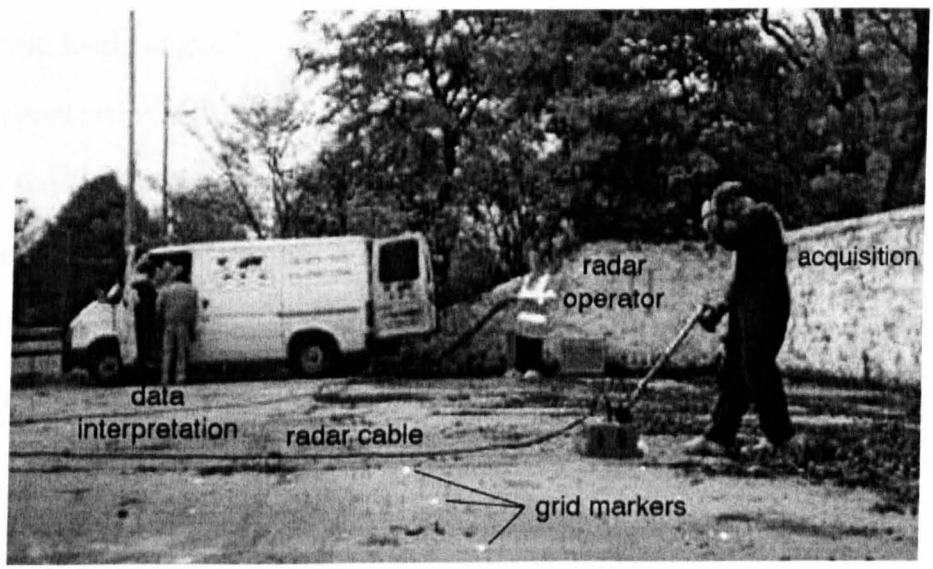

Figure 1.2: Data acquisition with the SIR-2 at a former service station

1.2.1 Data Acquisition

Most commercial GPR systems are time-domain impulse systems. A train of pulses typically of amplitude 100 to 1000 V and of duration between 1 and 10 ns is applied to the terminals of an antenna and launched into the transmission medium. In accordance with the laws of classical electromagnetism, as the pulses propagate downwards through the ground, they interact with subsurface materials in a variety of ways, including attenuation, reflection, refraction, diffraction and scattering. However, the two most important physical conditions which impact on the behaviour of radar waves are the material dielectric properties and conductivity.

The most common antenna arrangement is with the electric fields of the transmitter and receiver antennas aligned in parallel with each other, parallel with the earth, and towed in a traverse direction perpendicular to the magnetic field direction. This results in a wave propagating perpendicular to the surface of the earth, into the earth. If such an arrangement is pulled across a buried metallic pipe (or wire or rebar) with the electric fields aligned parallel to the length of the pipe, the pipe appears in the ground penetrating radar data as an excellent reflector, with a hyperbolic shape (the shape is the result of the antenna pattern and geometry of traverse motion). If the antennas are rotated 90 degrees, so they cross the pipe with the electric field direction at right angles to the long axis of the pipe, the pipe disappears (it's still there, but very tough to see). In general, three sets of measurements are required with antennas oriented (relative to the electric fields) parallel to the surface of the earth and:

1. Parallel to each other and perpendicular to traverse direction,

2. Parallel to each other and parallel to traverse direction, and

3. Perpendicular to each other (cross-polarised)

The dielectric constant of the medium determines the speed of the electromagnetic wave; the lower the value of this coefficient the faster the propagation of the wave. A sudden reduction in the relative permittivity such as might occur at a geological boundary, will lead to a corresponding increase in the speed of the wave and a consequent reflection of some of the energy back to the surface. Slowing of the wave also results in a concomitant energy loss.

The conductivity of the substrata is the most important factor determining the rate of signal attenuation. Materials with high conductivities will cause rapid dissemination of the transmitted pulse through the transformation of the electromagnetic energy into heat as ions within the medium become excited. Signal loss is consequently greater in clayey soils. Signal loss can also result from scatter of the transmitted pulse during interaction with large inhomogeneities within the subsurface, such as cobbles or bricks.

The reflected energy is gathered by a receiving antenna (as shown in Figure 1.4), which is usually similar to the transmitting antenna. The antennae used in a GPR survey are selected on the basis of the depth of interest and the size of the target. Penetration depth varies inversely with frequency and the higher the central frequency of the antenna, the smaller the size of the objects that can be resolved. Although some older radar systems store the data in analogue form, most modern systems digitise the data for subsequent display and storage. As few available analogue-to-digital converters would be able to keep up with the received signal in the high MHz region, the received waveforms are first coherently sampled (typically into 512 or 1024 time intervals) and then quantised before being digitised (usually to 8 or 16 bits). This

signal, an example of which is shown in Figure 1.3 is referred to as an *A-scan*, or simply a *scan*.

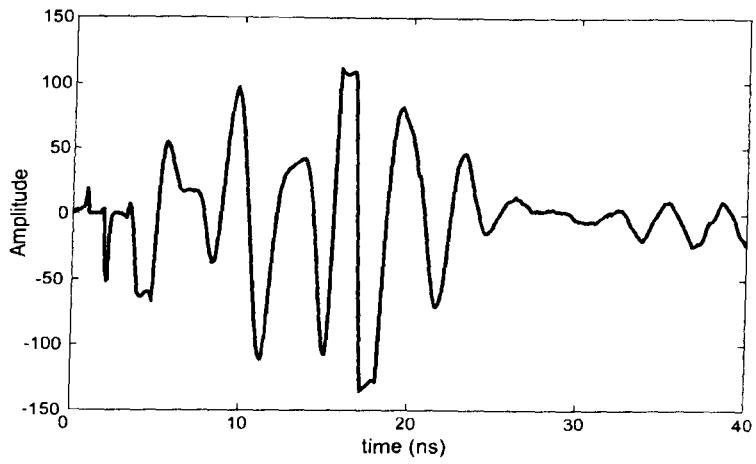

Figure 1.3: Example of a single A-scan

In most commercial GPR systems, this "raw" digital data is recorded onto magnetic storage media for future recovery and off-line processing. In the GSSI SIR® System-2 system used in the present study however, on-site processing is performed *before* storage, as shown in Figure 1.4.

1.2.2 Acquisition parameters

The SIR-2 system provides a data acquisition setup facility allowing the user to select a number of parameters. These settings determine the operation of the receiver (such as the levels of quantisation and the range), and control the on-board signal processing operations (such as the filtering and range-gain functions), and are stored in a setup file, with the former also included in the radargram file header. The structure of GSSI's `dzt` radar data format is detailed in Appendix D, and in addition to the system setup information, contains field information such as the acquisition

date, site location and direction of the survey lines. This information can be retrieved at a later stage to further process the data or to generate reports. Some of the more important of these settings are described below.

Signal conditioning parameters

The form of the digitised signal is selected by setting the number of samples_per_scan and the number of `bits_per_sample`. The former is typically set to 512, and depending on the volume of the survey data and the storage limitations, the latter, which determines the resolution of the data, can be set to either 8 or 16.

The `range` is a time setting, measured in nanoseconds, which determines the length of the time series to be recorded, and the A-scans last only as long as this two-way travel-time. The range will also directly determine the depth of penetration, and a typical value for 400 MHz operation in an urban environment is 60 ns corresponding to an approximate penetration of 3 m.

The horizontal sampling rate along the ground is controlled by the `scans_per_second` value, establishing the density of the scans. This is determined to a large extent by the speed at which the practitioner wishes to conduct the survey, and for on-foot surveying 32 scans/second is usually adequate.

Pre-processing parameters

The digital data is band-pass filtered by the combination of an internal low-pass and high-pass filter, both of which are three-pole IIR (infinite impulse response) filters which operate on each incoming "vertical" A-scan. The low-pass filter is used to eliminate high frequency noise (appearing as "snow") from the data, and is defined by setting the cutoff frequency, in MHz. The higher this frequency, the less the data

removed by the filter. The setting recommended by the manufacturer GSSI [1] is twice the antenna centre frequency. The high-pass filter is used to eliminate low-frequency noise and some of the system ringing from the data, and is also defined in terms of the cutoff frequency in MHz, and the recommended setting is one sixth of the antenna centre frequency.

Attenuation caused by the propagation medium and by the path and spreading losses causes the received signal to be significantly diminished in amplitude compared with the transmitted signal. A digital range-gain function is available to process the A-scans to make the signal strength independent of depth or travel-time, thus improving the detectability of deeper reflections. This is achieved by multiplication of the sampled signal in time by a time-varying gain function. Figure 1.5 illustrates the effect of this range-gain function. The function is defined on a logarithmic scale by linear segments between uniformly-spaced (in time) gain points. The number of these nodes is decided by the radar operator, and their values in decibels can either be adjusted manually, or automatically by the acquisition software. These are stored in the `.dzt` file header so that the gain can be later compensated for and modified off-line.

1.2.3 Range

The range of a GPR can be simply defined as the maximum depth from which a reflection can be detected by the receiving antenna. Range is mainly governed by the total path loss which is mainly caused by material loss, spreading loss, and target reflection loss or scattering loss [2]. The signal that is detected by the receiver undergoes various losses in its propagation path from the transmitter to the receiver

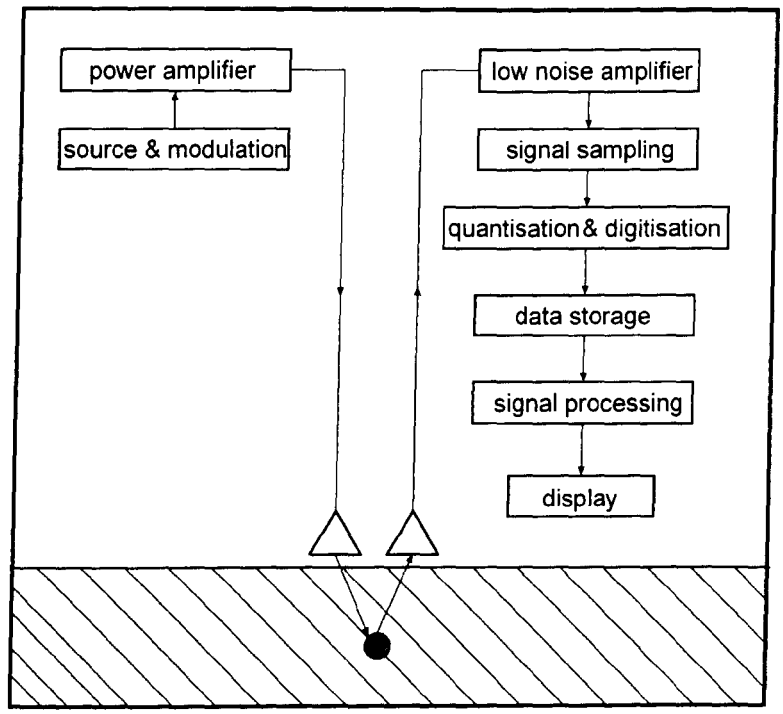

Figure 1.4: SIR-2 ground penetrating radar system components

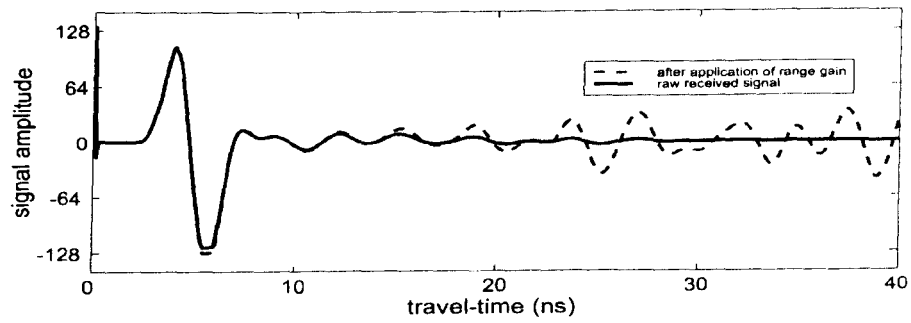

Figure 1.5: Radar scan before and after application of range-gain function

as this can be seen in Figure 1.6.

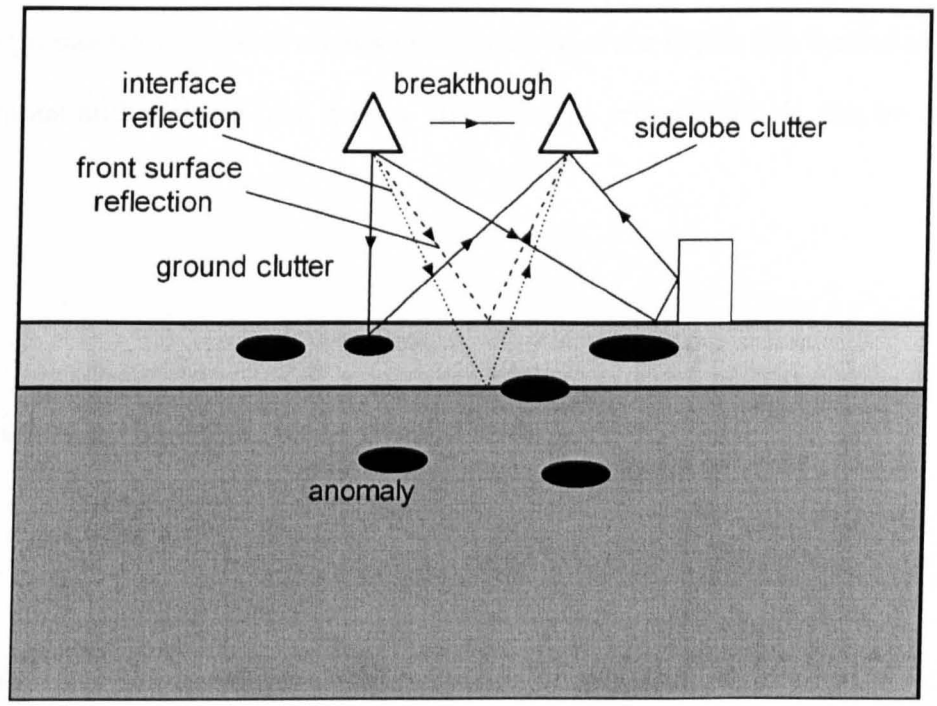

Figure 1.6: Exaggerated illustration of multi-path propagation

It is these loses which limit the detectibility rage of a ground penetrating radar. Furthermore, the desirable demand of a high resolution data-images would strongly participate into this limitation, as it requires higher frequencies and hence shallower penetration depths. In the cases where automatic detection of certain shaped targets (such as pipes or landmines) is involved, high resolution images are a crucial demand as the automatic processing of data relies to a high extent on the clarity of the reflections obtained from such targets. This is of course achieved at the expense of a very limited depth of no more than few meters. In other applications where the detection process is not highly dependent on the clarity of the obtained image, then high resolution can be compromised for the sake of a deeper detectability range. Examples for such applications are soil disturbances, voids, and cavities.

1.2.4 Speed of Propagation

The propagation speed is an absolute measure of the depth of a buried object. For homogenous and uniform host media, the speed of propagation $\hat{v}_s$ can be calculated from

$$\hat{v}_s = \frac{c}{\sqrt{\epsilon_r}} \tag{1.1}$$

Accordingly, the depth can be derived from

$$d = \frac{\hat{v}_s \hat{t}}{2} \tag{1.2}$$

where here c is the speed of electromagnetic propagation in free space[1], ϵ_r is the relative permittivity of the medium,while $\hat{t}$ is the two-way travelling time, to and from the target.

In most practical situations the relative permittivity will be unknown. The normal procedure for estimating $\hat{v}_s$ is done either by means of direct measurement of the depth to a physical interface or target (i.e. by trail holing), calculation by means of multiple measurements, or broadly estimating it depending on the knowledge of the medium type.

An alternative method of calculating the depth of a single planar reflector is by means of the *common depth point method.* If both transmitting and receiving antennae are moved equal distance from the common centre point the same apparent reflection position will be maintained [2].

The variation of permittivity with frequency in wet dielectrics implies that there will be some variation in the speed of the propagation with frequency. A dielectric

[1] The speed of light is approximately 0.299792458 mns^{-1}.

exhibiting this characteristic is said to be 'dispersive'. Where the material has different propagation characteristics in different directions it is said to be anisotropic, and an example is coal in the seams prior to excavation, where the propagation characteristics normal to the bedding plane are different from those parallel to the plane. In sub-surface radar work the elapsed time between the transmitted and received pulses is measured in nanoseconds because of the short travel path lengths involved. It could be seen from Equation 1.1 that $\hat{v}_s$ is inversely proportional to the square-root of the relative permittivity.

The uncertainty about the value $\hat{v}_s$ could lead to disastrous consequences when application such as mines detection or major utility pipes and cables detection are involved, as a wrongly estimated $\hat{v}_s$ directly affects the calculation of the depth of target as this will be shown in Chapter 3.

1.2.5 Clutter

The clutter that affects GPR data scans can be defined as the set of signals that are not related to the target though they have similar spectral characteristics to target reflections. Clutter can be caused by breakthrough between the transmitting and receiving antennae as well as multiple reflections from the ground surface to the receiving antennae. Local variations in the characteristic impedance of the ground can also cause clutter, as can inclusions of groups of small reflection sources within the material. In addition, reflections from targets (which could be above the surface) in the side lobes of the antenna can be another source for clutter. The effect of clutter is more significant to the near-range GPR performance while it decreases at longer ranges. This problem can be overcome by careful antenna design and incorporating

radar absorbing material to attenuate the side and back lobe radiation from the antenna [2].

1.2.6 Data presentation

The objective of GPR data presentation is to provide a display of the processed data that closely approximates an image of the subsurface, with the anomalies that are associated with the objects of interest located in their proper spatial positions. Data display is central to data interpretation. In fact, producing a good display is an integral part of interpretation.

There are three of displays of surface GPR data, including:

- One-dimensional trace
- Two dimensional cross-section, and
- Three-dimensional display

The raw data acquired from the above GPR configuration is in the form of a two-dimensional image consisting of a lateral ensemble of sampled time series with horizontal and vertical dimensions of scans and two-way travel-time respectively. These waveforms can either be plotted side-by-side in the form of a "waterfall" or "wiggle" plot, or colour-coded by representing each waveform by a vertical line with the amplitude of each sample represented by a pixel intensity level or colour. This two-dimensional image display is called a *radargram* or *B-scan* profile. To enhance the visibility of certain features, a number of options may be customised, such as the density of the waterfall traces, the number of colours and the colour table. A contour plot showing points of equal amplitude is also commonly used on monochrome

displays. To emphasise or de-emphasise certain features, arithmetic transformations such as the square root or absolute value are often applied. The square root for instance, assigns low amplitude samples a larger range of colours than higher amplitude samples, enhancing the sensitivity of the display to lesser reflections.

Three dimensional displays are fundamentally block views of GPR traces that are recorded at different positions on the surface. Data are usually recorded along profile lines, in the case of a continuous recording system, or at discrete points on the surface in fixed-mode recording. In either case, the accurate location of each trace is critical to producing accurate 3D displays. Normally, 3D block views are constructed, then they may be viewed in a variety of ways, including as a solid block or as block slices.

Figures 1.7 and 1.8 show the radargram of two pipes buried in soil (see Appendix B) presented with a variety of display options.

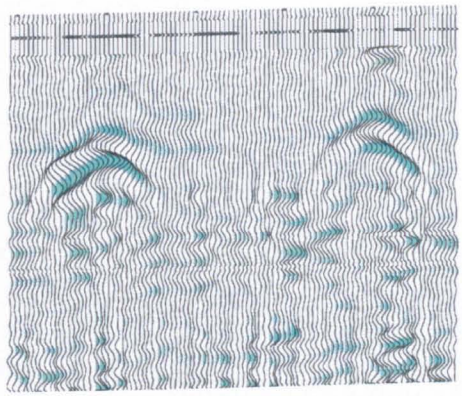

(a) "waterfall" display (close-up)

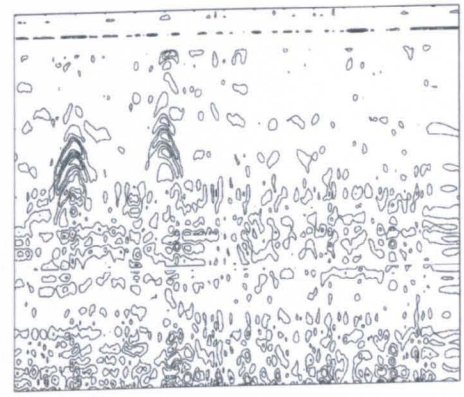

(b) contour display

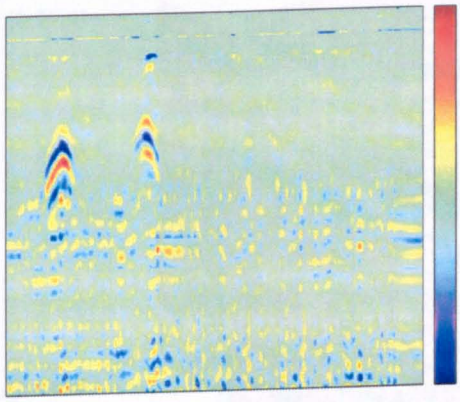

(c) colour-amplitude format (128 colours)

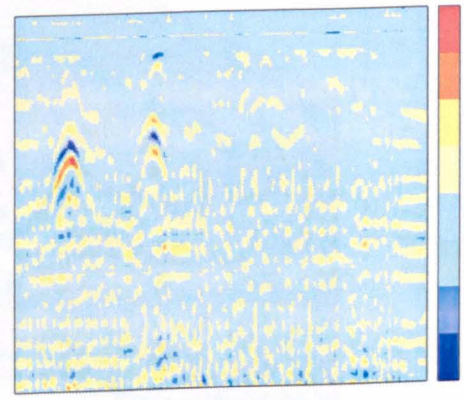

(d) 8 colour display

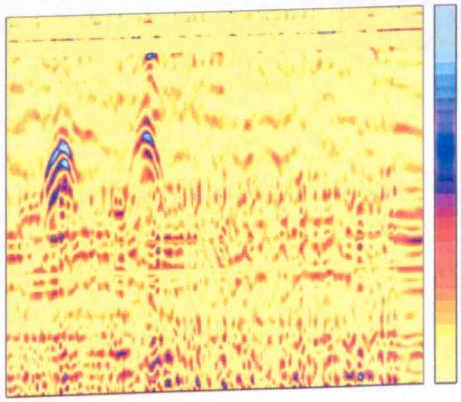

(e) absolute value

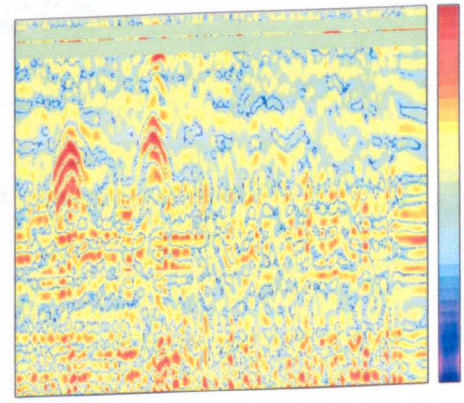

(f) square root

Figure 1.7: Effects of various B-scan display options

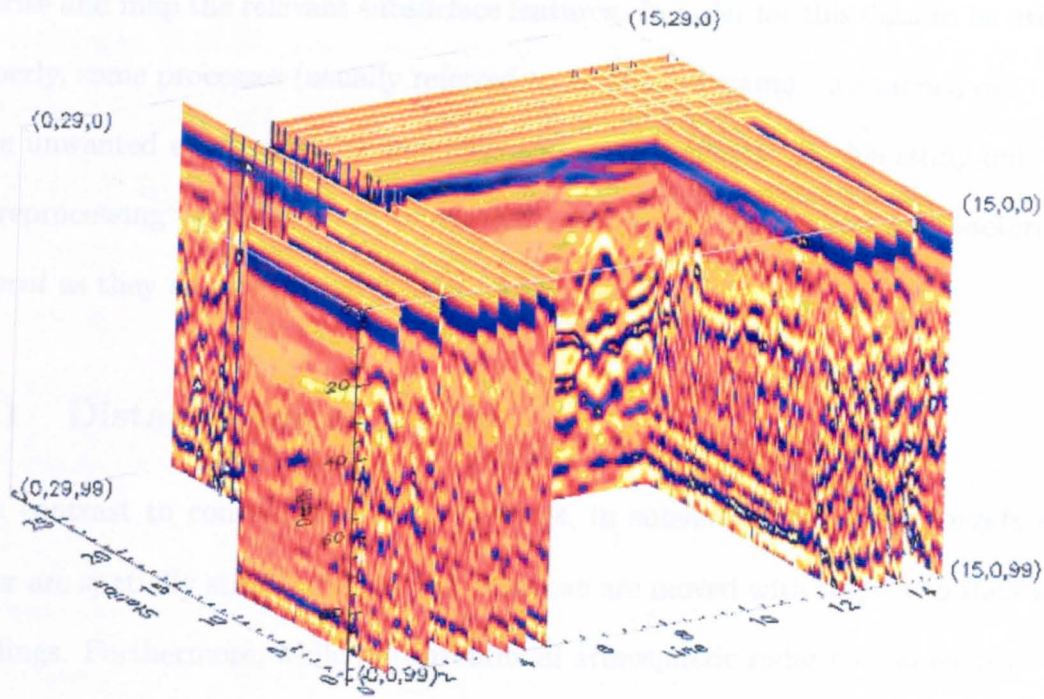

Figure 1.8: Three-dimensional display of part of an orthogonal grid of B-scans

1.3 Off-line Processing

Although the visual radargram display can often give the operator an initial on-site impression of the subsurface environment, only in very rare situations such information is sufficient for an adequate assessment of subsurface features. The recorded digital radar files are subsequently downloaded from the radar system onto a personal computer and subjected to further analysis and processing to accurately locate, characterise and map the relevant subsurface features. In order for this data to be utilised properly, some processes (usually referred to as *pre-processing*) are carried out to remove unwanted environmental, operator and system effects. In this study only two of preprocessing operations are considered; *distance normalisation* and *background removal* as they are considered crucial for the study.

1.3.1 Distance normalisation

In contrast to conventional radar systems, in subsurface radar the targets and clutter are spatially stationary and the antennae are moved with respect to their surroundings. Furthermore, while in conventional atmospheric radar the target position is sought relative to the transmitting and/or receiving antenna, in ground-probing radar the positions must be given in relation to surrounding objects or to a reference grid on the ground surface. Thus in order for the acquired data to be of any practical use, there must exist enough spatial positioning information in the data to correlate any detected features with these surface co-ordinates. With the radar operating in continuous mode, the most common method for incorporating this spatial positioning information into the radar file is by placing fiducial event markers in the data whenever the antenna covers a given lateral distance.

In practice, these markers are often introduced by a manual switch or button controlled by the radar operator, with the distance calibrated by means of a measuring tape, regularly-spaced survey pegs or spray markers, or in certain circumstances by human estimation. Alternatively, a wheel odometer or other dynamic distance measurement device can simplify this task; its electrical readout is used to place fiducial marks in the record in place of the operator's button.

The SIR-2 system records these fiducial markers as spikes of amplitude 90% of the maximum dynamic acquisition range, positioned at the second sample of the time series. The spacing between consecutive markers is governed by the speed of the movement of the transducer, and the uncertainties of the survey environment rarely permit uniform radar movement. Interpretation is most effective when the spatial axis of an image is linear and data is of uniform spatial density.

To remove the distortions created by the variations of speed, a process of distance normalisation is developed to locally compress or stretch the image segments between markers resulting in a linear array of markers corresponding to the true survey coordinates. This normalisation is often referred to as "rubber band" processing or "rubber sheeting". The scans between each two fiducial markers separated in an array of scans f_1 by s_1, are either stacked or interpolated to render a regular spacing of s_2 scans. In this and all subsequent flowcharts, the default direction of flow is downwards.

The marker spikes are then removed from the data, and the modified file information is logged in the file header for future reference. If the distance in meters between the markers is known (`metres_per_mark` in the header), then the corresponding header entry for `scans_per_metre` is calculated directly as

$$\texttt{scans\_per\_metre} = \frac{\texttt{scans\_per\_mark}}{\texttt{metres\_per\_mark}} \tag{1.3}$$

In addition to attaining spatial uniformity, the distance normalisation procedure can also used to reduce the size of the radar files to facilitate processing and storage. Furthermore, stacking has the desirable effect of reducing the effects of random noise by averaging several radar signal returns over the same point.

1.3.2 Background clutter removal

Very often the radargram interpretation problem involves the extraction of a localised wavelet function from data with very similar time domain characteristics to the wavelet. These spurious reflections can be caused by breakthrough between the transmitting and receiving antennae, poor coupling with the ground, reflection from the surface, layered geology, antenna ring-down or system effects within the radar system. Removal of horizontal commonalties facilitates extracting useful information from the signals, and has the effect of a high-pass filter. This is apparent in Figure 1.9, where the high contrast of the coupling pulse causes the lesser reflections to be obscured. This situation is referred to as *blanking*.

When the characteristic impedance of the transmitting antenna is not matched to that of the medium, some of the energy is stored in standing waves within the antenna elements and radiated over an extended period of time, causing the antenna to "ring". This ring-down effect is made worse by the limited fractional bandwidth of the antenna, and combined with the pulse breakthrough, coupling and surface reflections, often completely obscures less intense reflections from shallow targets.

It is possible to remove this "background" banding or clutter by subtracting from

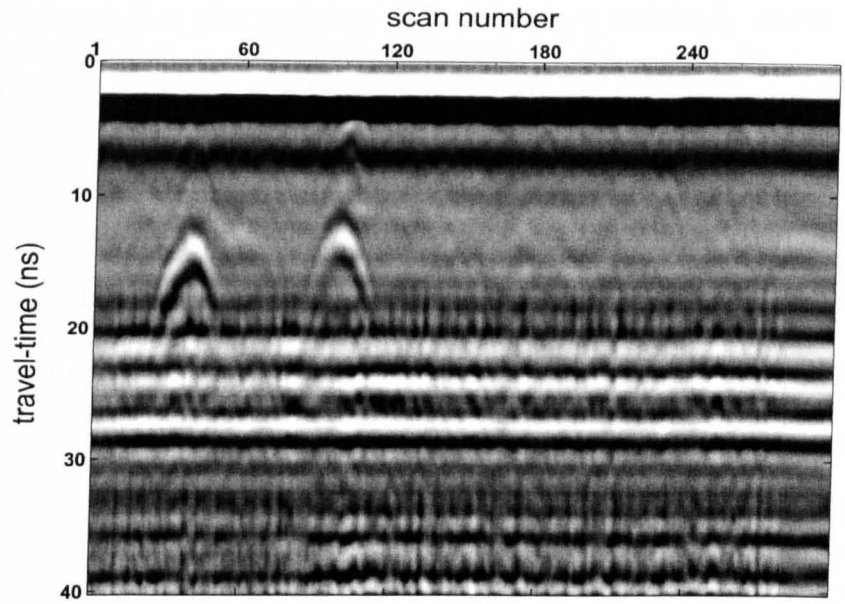

(a) Radargram before background removal

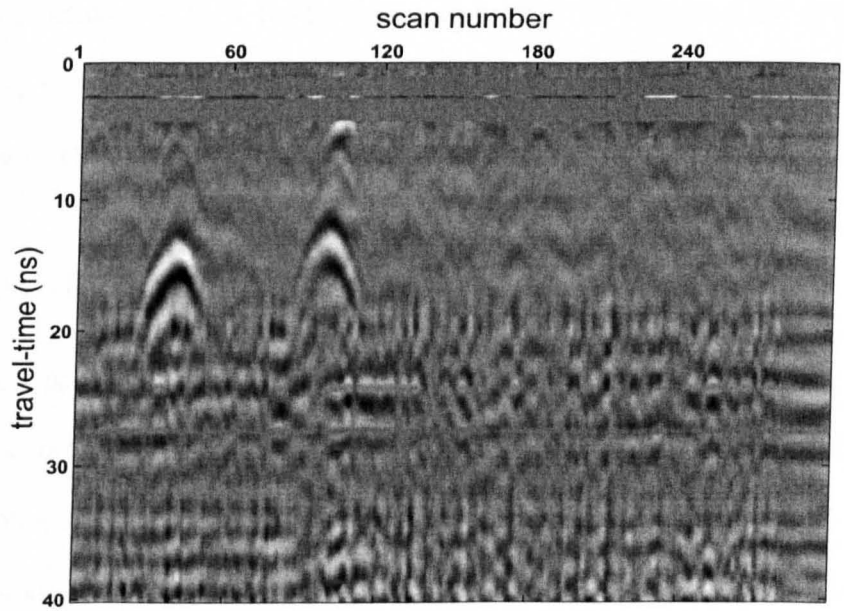

(b) After background removal

Figure 1.9: Contrast-enhancement caused by background removal

each scan an ensemble average of the stack of A-scans over the region of interest. Here it is assumed that the material properties vary randomly about a location-independent mean, and that the target indications are present in a relatively small number of measurements. Thus the mean of a large number of measurements can be considered to be a measure of system clutter. The image is divided into vertical strips of approximately 60 scans (or the equivalent of three meters), and then the ensemble mean of each row of pixel intensities across each strip is subtracted. Using the same notations as before, with $s(i)$ the unprocessed A-scan and win the width of the strip of scans starting from scan number j_{bg}, the processed A-scan $\bar{s}(i)$ is calculated using

$$\bar{s}(i) = s(i) - \frac{1}{win} \sum_{j=j_{\text{bg}}}^{j_{\text{bg}}+win-1} s(j) \tag{1.4}$$

Clutter associated with a particular region may be removed by specifying the corresponding values of j_{bg} and win. This technique is particularly well-suited for instances where the targets are well-separated.

1.3.3 Post-Processing

The notion *post-processing* usually refers to the set of processes that take place after the collected data is processed to remove unwanted environmental, operator and system effects. These processes usually start with pointing out the targets of interest (manually or automatically) throughout the whole collected data scans, then comes the crucial stage of interpreting the detected data in terms of their types, dimensions, and depth. Until now, this interpreting stage is still highly dependent on the experience of a professional operator and subjected to broad assumptions in the majority of cases where the lack of ground truth is the standard case.

Target Detection

A common procedure in the target detection stage is for a human operator to go through the collected radargrams to point out any target of interest. This procedure is still widely followed despite being subjected to the human slowness, error-judgments, and inconsistency. There could be few reasons for this, among them is the lack of confidence in machine-decisions specially when critical applications involved such as mine detection, the expensive computational demands and limited accuracy of many automatic detection procedures. Although human interference is still heavily involved, yet semi-automated procedures are applied to rapid up data-processing with human operator intervention. Many GPR data-processing softwares include a variety of options regarding off-line procedures, data-enhancement procedures, in addition to signal processing, image processing procedures to help the operator to optimism his work in terms of speed and consistency.

The collected data could be looked at as *B-scans* or in *three dimensional slices*, whereas *A-scans* are not suitable for human-eye detection. Simplifying the image, by eliminating the noise and clutter, is the most important factor for optimising the detection. Image simplification may be achieved by:

- Assigning the amplitude-colour ranges.
- Displaying only one polarity of the GPR signals.
- Using a limited number of colours.
- Decreasing the size of the data set that is displayed as the complexity of the target increases.
- Displaying a limited range (finite-thickness time slice) and

- Selecting the viewing angle (in case of 3-dimensional processing)

Some of these image simplification methods are used in Figures 1.7 and 1.8 resulting in different views for the collected data.

Interpretation

The interpretation stage is the last and most important stage among the GPR data-processing procedures, as it brings out the final decision regarding the data under investigation. This interpretation process is often characterised by uncertainty, subjectivity, inconsistency, assumptions and rules-of-thumb. This is mainly due to the existence of the human-factor and the many unknowns with regard to the investigated site. The interpretation stage usually involves connecting the detection information from individual radargrams and accompany them with broad assumptions and rules of thumb or ground truth (which is very rarely available). This could be achieved with the aid of a computer software.

The available softwares for GPR data processing deal with the acquired data on either one-dimensional signals (A-scans) basis, or two-dimensional date (B-scans) basis. For the A-scans case, several methods may be included such as inverse filtration, wavelet-correlation, and auto-correlation processing. Methods of signals require calibrating signals, measured in advance. Correlation and auto-correlation processing enable to compare measured reflected signals and calibrating signals, reflected from various objects, and choose the best suite waveform [2]. In case of the B-scans based processing, the problem is dealt with as an image processing one and hence a variety of image processing techniques can be applied such as features extraction and segmentation and edge detection and processing. Three-dimension image of objects can

be obtained by migration. Different GPR researchers have different opinions about which approach is more adequate.

Despite the variety of commercial softwares for processing GPR data and the continuous developments of these softwares, the human-factor is still heavily involved in almost every stage. Moreover, all the crucial decisions regarding the detection and interpretation are made by human operators. This process consumes significant amount of time (and hence money) and this often delay detracts from the desirability of GPR as a rapid non-invasive site-investigation tool. This problem is compounded by the added problems of inconsistency and human error.

When the accuracy is critical in mapping buried services and plant, there is added premium on the need for reliable accurate interpretation of this data, exploiting the knowledge of the data-acquisition geometry. This necessitates the need for a complete data-processing automatic system that requires minimum human intervention. This system has to be able to detect the desired targets, analyse them, and present a final interpretation report rapidly and consistently.

1.4 Previous Work

The interests of GPR researchers are usually divided between the areas of radar system and technology, problem inversion and modelling, and data processing, vision, and analysis. A general review of ground penetrating radar background, theory, and implementation considerations as well as a description of various available system approaches and equipment is presented by Daniels [3, 4, 2].

Sai and Ligthart [5] present a comprehensive two-dimensional technique for pre-processing the data acquired by a continuously moving ultra wideband impulse ground

penetrating radar. The operations include DC-offset removal, frequency filtering, background removal, gain compensation, and data interpolation. The results showed enhanced GPR images suitable for further detection and interpretation processes.

Merwe et al. [6] present a clutter-reduction technique for GPR data from mine like targets. The basic concept of this technique lies in treating the clutter as an unknown deterministic component. An equation derivation is made that represents the GPR desired target contributions, as well as the clutter contributions, then it was applied in an iterative technique to eliminate the clutter effect, without taking into consideration the effect of the subsurface inhomogeneities. This suggested technique has two main disadvantages: it is time-consuming, and is based on estimating values for the desired signals, and neglecting the clutter effects.

Carevic [7] presents a method for simultaneous clutter suppression and signal detection in GPR data. It computes a running estimate of the background signal and detects abrupt changes from the estimated signal, assumed to correspond to the returns from a buried object, using a translation invariant (TI) wavelet packet decomposition. This paper lacks any results of applying the method on real GPR data. While Carevic et al. [8] present a Gaussian mixture modelling procedure for target-specific feature extraction from GPR signatures along with a Bayseian classification technique to identify mine-like targets.

Ulug et al. [9] describe the application of radial basis function (RBF) classifiers to feature-based automatic target recognition using Synthetic Aperture Radar data. They produce a performance comparison between the RBF and several other classifiers, and make a conclusion that the RBF network performs better and is more robust to this type of noise when compared to the other feature-based classifiers they considered. The paper does not show a quantitative measure for the obtained results,

besides the crucial issue of time-cost is not addressed.

Gamba and Lossani [10] present a simple feed-forward neural network, that has the job of detecting the hyperbolic shapes within the pre-processed images and according to a certain thresholding arrangement, the network would decide whether the certain shape represents a part of a pipe or not. Lotlikar and Kothri [11] present a simple dimensionality reduction criteria, which is based on using a neural network classifier to produce a reduced image containing the data of interest, and applying this criteria to some feature extraction techniques to make a comparison between them. The efficiencies of the proposed neural networks are not quantified and the time-cost issue is not addressed.

Al-Nuaimy et al. [12] present an automatic detection regime for buried utilities and solid objects combining artificial neural network-based classifier and pattern recognition technique. Furthermore, the authors in [13] present a novel multi-resolution texture discrimination technique based on unsupervised neural network and capable of identifying four types of classes. A main limitation for these techniques is their high time cost.

Grandjean et al. [14] present a computer software package with a modelling routine that generates synthetic hyperbolae to compare with GPR-resulted hyperbolic shapes, with the possibility of a number of iterations to achieve a match. The program is for off-line processing and requires human involvement, and hence unsuitable for an automatic near real-time requirement. The way by which the program deals with data files and the iterative method leads to a limitation in dealing with large volumes of radar data, and makes it rather slow. It is also noticed that there was no specific examples indicating the efficiency of the proposed program in dealing with real data.

Al-Nuaimy et al. [15] present an interesting automatic technique for mapping

of linear structures in 3-dimensional space in GPR using a 3-dimensional Hough Transform. This technique is applied in the final stage of the automatic system presented in this study.

Capineri et al. [16] present a theoretical development and application of a data visualisation method that uses Hough Transform for locating straight lines and hyperbolic arcs in 2-dimensional images. They have used this method to locate buried objects in GPR images. The technique requires human operator intervention and has a high computational cost.

In [17] the authors produce a multi-component imaging algorithm that takes into account the properties of the vectorial character of the electromagnetic field and the radiation characteristics of the source and the receiver. This imaging algorithm employs four source-receiver configurations to obtain a bounded imaging operator.

Smith and Brown [18] present a data analysis and visualization software to process directional borehole radar data. It consists of a suite of signal and image processing routines written in Interactive Data Language (IDL). Examples are presented of laboratory data acquired with the prototype tool from two different experimental settings. The first experiment imaged plastic pipes in a macro-scale sand tank. The second experiment monitored the progress of an invasion front resulting from oil injection.

Roberts and Cits [19] present a method of GPR data- imaging using orthogonal profile line data. A 3-D image generated from a migrated and concatenated data-file is manipulated to detect linear and finite-size targets. Moreover, they present comparisons of the data visualization capabilities between one-direction and orthogonal profile line data. A major problem with migration techniques is their high time-consumption which makes them less attractive for on-site processing requirements.

Scheers et al. [20] proposes a migration method for GPR data that integrates the

time domain model of the GPR in the migration scheme. The method suggests the calculation of a synthetic 3-dimensional point spread function of the GPR by forward modelling. They show the results of this migration method on real data obtained reconstruct the top contour of small targets, in some cases even with the correct dimensions.

Binningbo et al. [21] present results obtained from applying a 3-dimensional migration algorithm to ground penetrating radar data collected with a switched antenna array. They use the Stolt wavenumber migration algorithm for 3-dimensional processing of the radar data. The migration is performed in the wavenumber domain, assuming constant wave velocity for waves travelling in the soil, and this assumption limits the efficiency of this method. With the signal antenna pair, the system could resolve the size and location of buried objects to within 5 cm in dry sand, while using the antenna array, the resolution was fully maintained, but with an increased noise level.

Despite the fact that Hayakawa et al. [22] do not present any theoretical or mathematical background to their work, they show some interesting results. They present a position measurements method to determine the position of GPR on the road by measuring the distance and direction in which it has moved, where survey data can be obtained by operating the GPR in arbitrary directions, while maintaining a survey speed corresponding to normal walking speed. In addition to that, the paper shows the results of a 3-dimensional visualization software to compile data of cross section and reconstruct the structure of buried objects based on a time-costing migration process. The results are not quantified and there is no mention of the time cost or the degree of human intervention.

Kruk and Slob [23] propose a method to deal with wavelets via introducing an

effective wavelet that incorporates the influence of the finite-length antennae, where, knowledge of the wavelet has the potential to improve the imaging and interpretation of GPR data. To obtain effective wavelet, the impulse response for a point source-receiver antenna system is calculated using the medium properties, that are obtained from the isolated air- and ground-waves observed on the actual common midpoint data. The deconvolution of this impulse response with the actual common midpoint data, yields an effective wavelet. They conclude that properties of the shallow sub-surface can be extracted from the ground-wave with reasonable accuracy.

In [24], Lee examines the structure of an image reconstruction algorithm for synthetic-aperture GPR systems operating with pulse-echo and step-FMCW (frequency modulated continuous wave) illumination schemes. The main structure of the image formation algorithms is based on the framework of the backward propagation image formation technique. The paper includes mathematical modelling, theoretical analysis, and results form full-scale experiments.

Barkat et al. [25] show that the processing of image data under varying assumptions can be used to adaptively determine the ground permittivity, which determines the propagation speed through the medium. Then they suggest that by considering the permittivity to be an unknown scalar parameter, several images can be formed as a function of the unknown parameter leading to a choice which maximises the sensitivity and resolution of the resulting image. After GPR image is segmented, the above concept is used to assign a relative permittivity value for each segment so that the range and cross-range location of a given scatterer are matched, then a single image is formed using adaptive permittivity values applied to each data segment.

Stolte and Nick [26] investigate the relationship between cylinder radius and hyperbola eccentricity for the purpose of migration, while Olhoeft attempts in [27] to

derive radius information from the curvature of the hyperbola apex with human intervention.

Despite the large number of site investigations and case studies relating to the detection and interpretation of buried cylinders, yet the attempts to automate these detection and interpretation processes are still limited and not been adequately satisfied. Moreover, the problem of making broad assumptions with regard to buried cylinders information and the host medium dose not seem to be thoroughly addressed, not to mention solving it. For these reasons, further research is needed in order to provide robust and reliable automatic data processing system based on a scientific foundation. This system provides a full description of the detected targets and the medium, in addition to eliminating any unnecessary assumptions.

1.5 Objectives and Scope of Work

This study addresses the problem of lacking a comprehensive and rapid automatic procedure for processing collected GPR data to detect cylindrical objects and present an interpretation report about the detected targets and their corresponding information such as depths, dimensions, and orientations.

To cover this subject, various image and signal processing techniques are investigated for detection and segmentation of reflections from cylindrical targets. Furthermore, a detailed modelling and characterisation procedure of buried cylinders representations in GPR images is presented for individual and collective images. This constitutes, in addition to the detection stage, a robust automatic detection and interpretation system with minimum human-interference requirement and can be used effectively by untrained radar operators for on-site data-processing purposes. The

main objectives achieved by this study can be summarised as follows:

1. Highlighting of feature zones using unsupervised segmentation of radar data.
2. Unsupervised estimation of diameter and orientation of cylindrical targets.
3. Unsupervised discrimination of number and geometry of clustered features.
4. Automatic combination of multiple data scans.
5. Unsupervised mapping of features and utilities in three dimensions incorporating site data and ground truth.
6. On-site applications in near real-time.

The input to the completed system would be a set of radar files covering a particular site along with the necessary information about the scanning grid, and present a reliable interpretation map of the detected subsurface anomalies, indicating the spatial extent, depth, dimensions information in addition to a dielectric constant profile map of the investigated site. This information is required within a short period of time, preferably on-site. The requirements thus stress a high degree of automation, robustness and computational efficiency.

These issues are addressed in the following four chapters of this thesis. Chapter 2 discusses detection and segmentation techniques that are used to discriminate the desired targets from other unwanted data. A few classification procedures are discussed in detail highlighting their points of strength and weakness. In Chapter 3, target reflections resulting from buried cylinders are modelled in a novel general equation. Furthermore, the derivation of a novel hyperbola-specific fitter is detailed and the combination of this fitter and the presented model for targets is used to calculate

crucial target parameters from individual radargrams. Chapter 4 discusses the processing of multiple radargrams to find linear cylindrical targets via the application of an adaptive non-accumulative 3D Hough Transform. Moreover, it is shown how this information is combined with information obtained from individual radargrams in an iterative manner to correct for target parameters and find further linear targets. Furthermore, a novel technique is discussed for creating a 3-dimensional profile of the dielectric constant of the site under investigation. Finally, Chapter 5 covers the overall conclusions of the project and the accomplished work in addition to some recommendations regarding any future work.

1.5.1 Published Work

Since this study was started, a number of journal and conference papers were published in scientific journals and proceedings of national and international conferences. These papers are listed below:

1. W. Al-Nuaimy, H. Lu, S. Shihab, and A. Eriksen. Automatic mapping of linear structures in 3-dimensional space in ground penetrating radar data. Proceedings of IEEE/ISPRS Joint Workshop on Remote Sensing and Data Fusion Over Urban Areas, Rome, 2001 [28].

2. S. Shihab, W. Al-Nuaimy, Y. Huang, and A. Eriksen. Neural network target identifier based on statistical features of GPR signals. in Ninth International Conference on Ground Penetrating Radar, Steven K. Koppenjan and Hua Lee, Editors, Proceedings of SPIE, 4758:135-138, 2002 [29].

3. S. Shihab, W. Al-Nuaimy, and A. Eriksen. Image processing and neural network techniques for automatic detection and interpretation of ground penetrat-

ing radar data. Proceedings of 6th WSEAS International Multi-conference on Circuits, Systems, Communications and Computers, Crete, 2002 [30].

4. S. Shihab, W. Al-Nuaimy, and A. Eriksen. Image processing and neural network techniques for automatic detection and interpretation of ground penetrating radar data. WSEAS Advances in Circuits, Systems and Signal Processing, pages 360-363, 2002 [31].

5. S. Shihab, W. Al-Nuaimy, Y. Huang, and A. Eriksen. Neural networks classifier for detecting subsurface objects. Proceedings of IEE/EPSRC Joint National Conference PREP2002, Nottingham, 2002 [32].

6. W. Al-Nuaimy, H. Lu, S. Shihab, and A. Eriksen. Automatic 3-dimensional mapping of features using GPR. in Ninth International Conference on Ground Penetrating Radar, Steven K. Koppenjan and Hua Lee, Editors, Proceedings of SPIE, 4758:121-124, 2002 [33].

7. W. Al-Nuaimy, Y. Huang, S. Shihab, and A. Eriksen. Automatic target detection in GPR data. in Ninth International Conference on Ground Penetrating Radar, Steven K. Koppenjan and Hua Lee, Editors, Proceedings of SPIE, 4758:139-143, 2002 [34].

8. W. Al-Nuaimy, Y. Huang, S. Shihab, and A. Eriksen. Unsupervised segmentation of subsurface radar images. in Ninth International Conference on Ground Penetrating Radar, Steven K. Koppenjan and Hua Lee, Editors, Proceedings of SPIE, 4758:635-638, 2002 [35].

9. S. Shihab, O. Zahran, and W. Al-Nuaimy. Time-frequency characteristics of ground penetrating radar reflections from railway ballast and plant. Proceed-

ings IEEE 2002 High Frequency Postgraduate Student Colloquium, Imperial College, London, U.K, IEEE catalogue no.: 02TH8642, 2002 [36].

10. O. Zahran, S. Shihab, and W. Al-Nuaimy. Comparison between surface impulse ground penetrating radar signals and ultrasonic time-of-flight diffraction signals. Proceedings IEEE 2002 High Frequency Postgraduate Student Colloquium, Imperial College, London, UK, IEEE catalogue no.: 02TH8642, 2002 [37].

11. O. Zahran, S. Shihab, and W. Al-Nuaimy. Recent developments in ultrasonic techniques for rail-track inspection. Proceedings of the annual conference of the British Institute of Non-Destructing Testing NDT 2002, Southport, UK, pages 55-60, 2002 [38].

12. S. Shihab, W. Al-Nuaimy, Y. Huang, and A. Eriksen. Automatic region-based shape discrimination of ground penetrating radar signatures. Proceedings of the Symposium on the Application of Geophysics to Environmental and Engineering problems SAGEEP2003, San Antonio, USA, 2003 [39].

13. S. Shihab, W. Al-Nuaimy, Y. Huang, and A. Eriksen. A comparison of segmentation techniques for targets extraction in ground penetrating radar data. Proceedings of the 2nd International Workshop on Advanced Ground Penetrating Radar (IWAGPR), Delft, Netherlands, 2003 [40].

14. W. Al-Nuaimy, Y. Huang, and S. Shihab. Multi-channel Filtering approach for unsupervised segmentation of subsurface radar images. Environmental and Engineering Geophysics, 8:93-101, 2003 [41].

15. O. Zahran, S. Shihab, and W. Al-Nuaimy. Time-frequency techniques applied to TOFD for the automation of rail-track inspection. Railway Engineering 2003

conference proceedings, UK, 2003 [42].

16. S. Shihab and W. Al-Nuaimy. A comparison of segmentation techniques for targets extraction in ground penetrating radar data. Near-Surface Geophysics, 2(1):49-57, 2004 [43].

17. O. Zahran, S. Shihab, and W. Al-Nuaimy. Discussion of the ability of defect classification in weld inspection using ultrasonic time-of-flight-diffraction technique. Proceedings of the IEE/EPSRC joint national conference PREP2004, UK, 2004 [44].

18. S. Shihab, W. Al-Nuaimy, and A. Eriksen. Radius estimation for subsurface cylindrical objects detected by ground penetrating radar. Proceedings of the Tenth International Conference on Ground Penetrating Radar, 1:319-322, Delft, Netherlands, 2004 [45].

19. W. Al-Nuaimy, S. Shihab, and A. Eriksen. Data fusion for accurate characterisation of buried cylindrical objects using gpr. Proceedings of the Tenth International Conference on Ground Penetrating Radar, 1:359-362, Delft, Netherlands, 2004 [46].

20. S. Shihab and W. Al-Nuaimy. Radius estimation for subsurface cylindrical objects detected by ground penetrating radar. Journal Subsurface Sensing Technologies and Applications, 6(1):1-16, 2005 [47].

21. W. Al-Nuaimy and S. Shihab. Data fusion for accurate characterisation of buried cylindrical objects using gpr. Submitted paper to the IEEE Transactions on Geoscience and Remote Sensing, 2005 [48].

1.6 Conclusions

This chapter described a basic time-domain impulse GPR system, its data acquisition procedure and the associated acquisition and processing parameters. Some off-line processes are described which are applied to compensate for system, operator and environmental effects, and the main *post-processing* procedure is discussed with the areas of weaknesses pointed out. Furthermore, a representative survey over the published literature was presented and discussed. The objectives for this study are outlined, in addition to a list of the author's published work. This chapter sets the framework for the problem this study is addressing as to be seen in following chapters.

Chapter 2

Target Detection

The techniques developed in this study for the automated detection of desired targets in GPR radargrams involve a considerable degree of signal and image processing techniques combined with artificial intelligence classification techniques. Artificial neural networks have been chosen in particular to replace the role of expert operators in recognising potential targets and rejecting unwanted data. In the following sections, a detailed description is presented of all the targets discrimination and classification techniques that were tested.

2.1 Introduction

In order to bring the GPR displays into a better condition that is suitable for interpretation, some pre-processing as well as post processing operations are carried out. Usually, these operations are manually handled by human operators, and consequently they would consume considerable amounts of time and effort. In addition, those operations are exposed to human inconsistency and error factor. To resolve this issue, it became necessary to find an automatic mechanism to carry out all the

processing on the path of presenting the desired operation.

Typically GPR data is processed off-line by a combination of manual and automated processing stages. Separating out genuine targets from background clutter and accounting for various environmental, system and subsurface effects require operator skill, experience and, most significantly, time. The analysis and interpretation of the large volumes of data generated by practical GPR surveys are extremely challenging and often presents an implementation bottleneck influencing the cost-effectiveness and applicability of the technique.

GPR images are unlike conventional images in that they can be treated both as images and as ensembles of time series, thus both signal processing and certain image processing procedures can be applied to them. It is important to know that a very small percentage of a typical GPR survey contains useful reflections, and thus these techniques often impose a prohibitive computational burden. Automatic selection of these anomalous zones can significantly reduce the dimensions of the data set with which one must deal, hence alleviating the computational burden during later processing and pattern recognition stages.

The work outlined in this chapter overcomes this problem by reducing the dimensionality of the data by outlining two-dimensional and three-dimensional regions within the data containing target reflections based on specific properties of the signal (A-scan) or image (B-scan). Through the analysis of these attributes, only those segments with specific characteristics of the radargram sought are retained, while the remainder of that radargram is discarded. This reduction permits more exhaustive image processing to be applied to the image, and results in improved computational efficiency in estimating target position and geometry.

In order to automate this selection process, attributes must be identified that

characterise the sought signals or images and distinguish them from other undesirable reflections. Figure 2.1 shows the stages which constitute an automatic detection and interpretation system for GPR data. Later in Chapter 4, it will be shown how this system is enhanced by combining information from multiple radargrams across the site in order to accurately determine the pipe parameters.

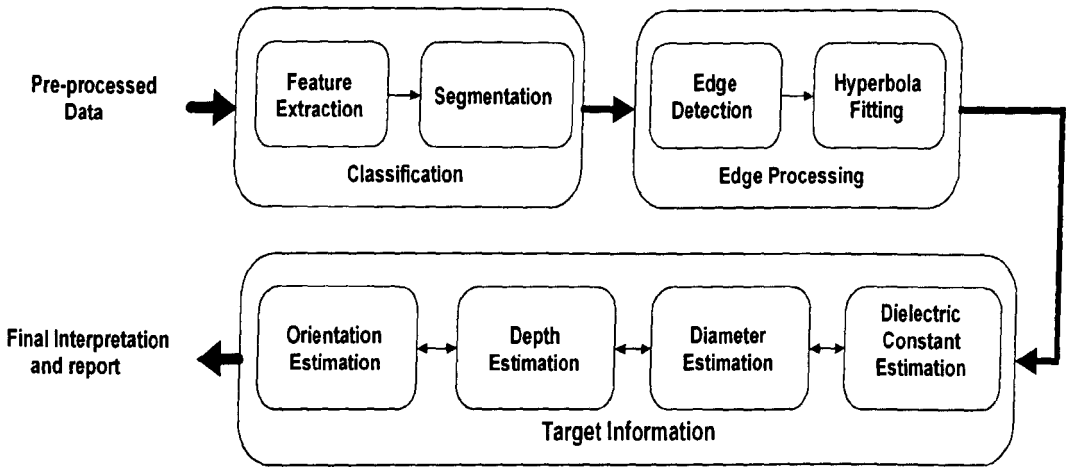

Figure 2.1: Block diagram of the automatic detection and interpretation system

2.2 Feature Extraction

In the ideal case, a signal received by the receiving antenna at a particular point should correspond to an anomaly that is located right beneath that point. In reality, the transmitted signal propagates along more than one path before being captured by the receiving antenna due to the nature of the antennae and the geometry of the data acquisition arrangement. Consequently, the received signal would be a combination of the different reflections along the different paths as was illustrated in Figure 1.6. The target detection process thus aims at distinguishing between the real targets and other undesired reflections.

Figure 2.2 shows a typical radargram collected at a controlled geophysical test site [49], at a location where two pipes are buried at a known depth within an uniform clayey soil (see Appendix B). It can be seen clearly that the region of interest is that where the hyperbolic signatures exist, as they represent the pipe, while the rest of the radargram is redundant. Hence, the first and most important step towards a robust and rapid automatic detection, characterisation, and interpretation system is to successfully identify the target related data and reject the rest in order to reduce the amount of the data set with which the subsequent stages would deal, and this would inevitably limit further computation cost to the useful data during later processing stages.

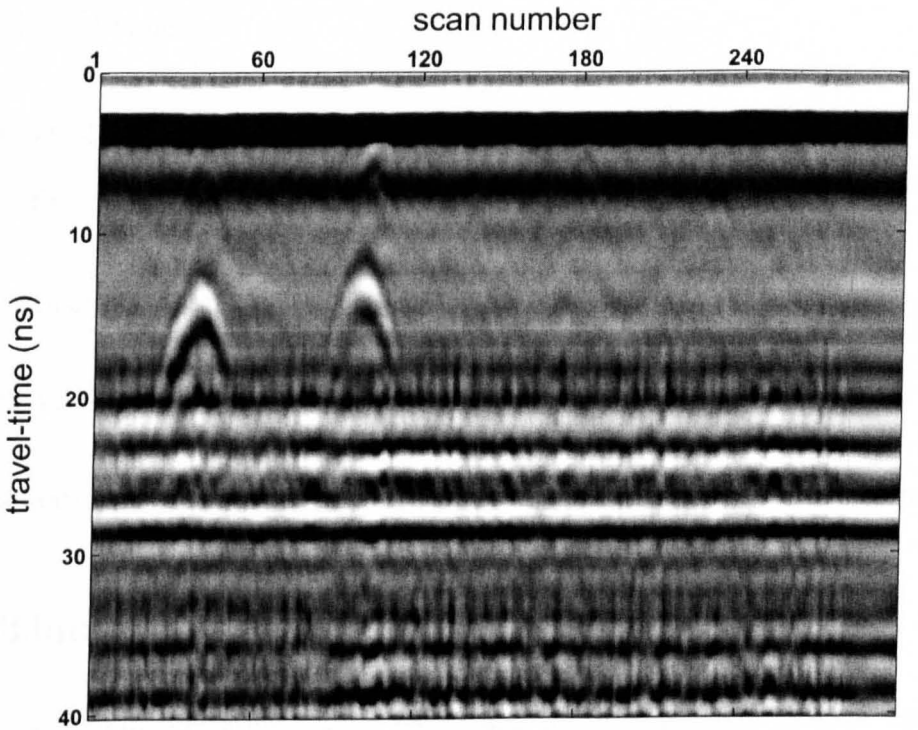

Figure 2.2: Typical ground-penetrating radar image

Based on the way in which the data are considered (i.e either A-scans or B-scans), the investigated segmentation-techniques can be divided into two major categories;

1. Time-series features and

2. Spatial features

With regard to the time-series features, after investigating several features of the reflected signals and examining the corresponding results, the following A-scan manifestations are considered

1. Statistical features

2. Spectral features

   a) Periodogram

   b) Time-frequency

As for the spatial features case, a similar procedure to the one that is followed in the time-series case leading to the following B-scan manifestations

1. Statistical features

2. Regional features

Theses features will be discussed independently in the forthcoming sections.

2.2.1 Time-Series Features

Although human operators find it easier and more convenient to deal with GPR data in the form of B-scans, it is interesting to mention that all subsurface information about the scanned areas are contained within individual reflections (A-scans). Despite this fact, it is almost impossible for an operator to differentiate between genuine reflections representing targets and other non-useful reflections. The reason can be

clearly seen in Figure 2.3 below, where both the target and non-target signals (which are drawn to the same scale) look much alike. Based on this, it becomes crucial to find the features of these A-scans that can provide good discrimination between targets and non-targets.

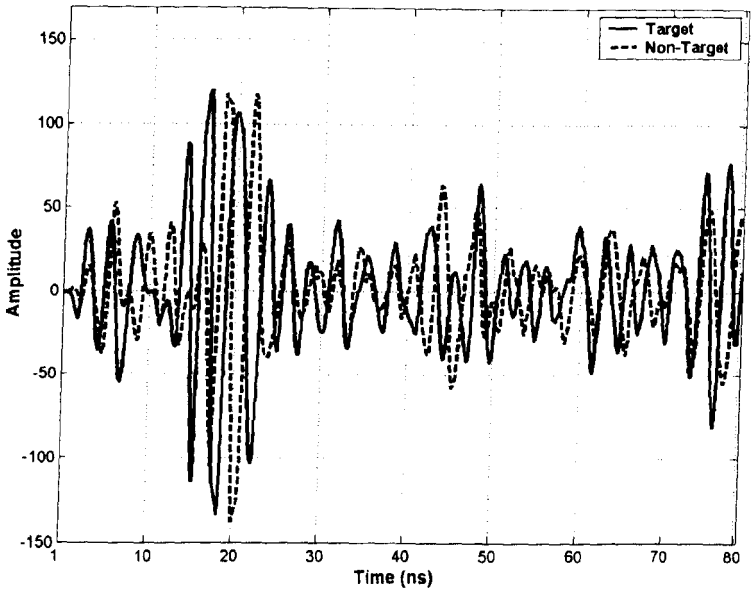

Figure 2.3: Two GPR scans, one of a target and other of a non-target

The selection process of suitable descriptors for a signal is one of the most critical and important tasks. There are two points one should keep in mind when searching for such descriptors. The first point is the nature of the signal, as some descriptors may be useful in some applications and not in others. The second is that the selected descriptor should, in some manner, emphasise a feature of a signal which is almost unique to that class of signals, so it can be discriminated from other classes. In addition to the above two factors, a third one of concern in this study is the time consumption.

During the recent years, many attempts were made by a number of researchers to produce automatic segmentation techniques (for example [12] and [13]), and these

techniques vary from one to another in many aspects such as accuracy, reliability, and speed.

Statistical features

Statistical features of signals are always tempting for providing unique information about different types of signals, either individually or collectively.

Here, an important question is raised; which features are to be selected? The answer to that depends on the type of the signal and the ability of each feature to provide discriminating basis for that particular type of signals from other types. In addition, and as mentioned before, the time-consumption issue is of a great importance here, and this might mean a tradeoff in the process of choosing the most suitable features between efficiency and complexity.

Based on the above, some statistical features are extracted from radar reflections to present discrimination basis between reflections generated from genuine targets and those representing clutter and noise. A number of statistical features are investigated on a data set that is specially built for this purpose. The data set consists of an equal number of different targets non-targets reflections that represent real data collected from a number of different sites.

A data set was built, in order to investigate the statistical descriptors properly. It consists of 50 target and 50 non-target signal-segments. It was noticed from various GPR data that effective data-content of targets and non-targets existed in an average 64-pixels of the A-scans. Consequently, the collected data set segments were chosen to be 64-pixels long each, and were collected from different sites and represented different kinds of targets such as pipes, reinforced concrete, tanks, and voids. Non-target scans, on the other hand represented different non-useful data such as clutter,

shallow reflections, noise, and attenuation.

The investigation of a variety of features [50], and [51] has led to the selection of three main descriptors, as they have proven to produce a good discrimination between signals returned from targets and other reflections. These three features are

1. Variance (second moment)

$$\sigma = \frac{1}{n-1}\sum_{i=1}^{n}(s_i - \bar{s})^2 \tag{2.1}$$

where s_i is the i^{th} element in the vector s of length n, and $\bar{s}$ is the mean value of s.

2. Mean absolute deviation

$$\text{MAD} = \frac{1}{n}\sum_{i=1}^{n}|s_i - \bar{s}| \tag{2.2}$$

3. Fourth moment

$$m_4 = \frac{1}{n-1}\sum_{i=1}^{n}(s_i - \bar{s})^4 \tag{2.3}$$

The selected features then were investigated for unsupervised clustering to test their ability to produce distinguishable clusters; targets, and non-targets. A hierarchical tree is used as a unsupervised clustering measure for the collected data set. This hierarchical tree is shown in Figure 2.4 and was formed as follows

- Calculation of feature matrix for the data-set, where each value in the matrix is considered an observation.

- Calculation of Euclidean distances between observations, which is given by

$$R^2(p_1, p_2) = \sqrt{(x_2 - x_1)^2 + (y_2 - y_1)^2} \tag{2.4}$$

where p_1 and p_2 are two observations in the matrix and $= (x_1, y_1)$ and (x_2, y_2) are their corresponding coordinates.

- Linking pairs of observations (using the $\cap$-shape connections) that have the nearest distances then linking the linked pairs with nearest distances to each other and so on.

- Forming clusters using linkage trees.

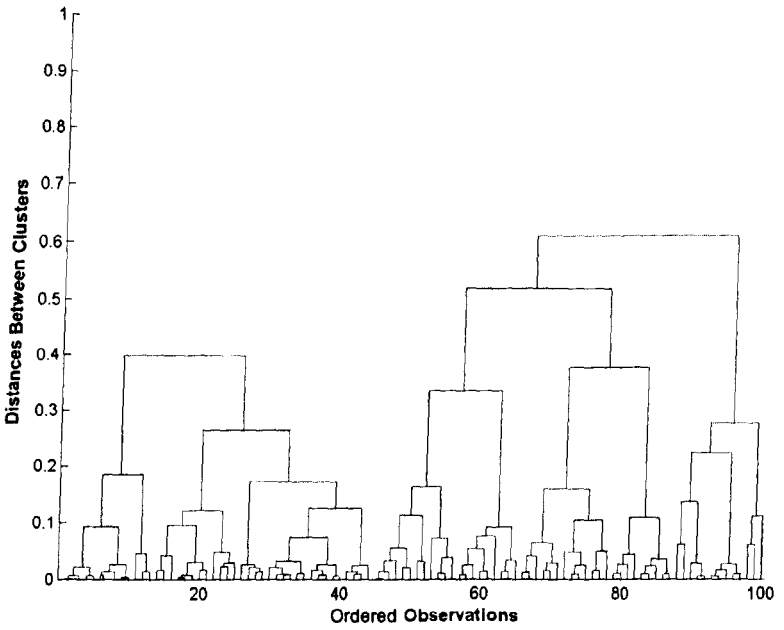

Figure 2.4: Hierarchical tree test showing targets and non-targets clusters

It is expected that the there should be 50 clusters corresponding to targets and 50 corresponding to non-targets, but this is not the result shown in Figure 2.4. This is

because the classification is unsupervised and was done without using an intelligent tool (such as artificial neural networks). Nevertheless, the obtained tree has shown good classification rates when mapped-back to the data set, and consequently, the classification accuracy will rise when a neural network classifier is used.

Spectral features

Pattern recognition techniques are used to discriminate between reflections from buried targets and other spurious ones. Different frequency-domain representations of the time-series data facilitate the pattern recognition task by extracting different features of the signal. As it is not known which features are directly relevant to the above discrimination, various spectral representations are investigated.

Periodogram

The two scans shown in Figure 2.3 are representatives of the two categories we wish to distinguish; one contains a target reflection and one contains only spurious clutter and noise. A sequence of samples may be represented by a set of spectral coefficients called the power spectral density (PSD), which provides a meaningful measure of the distribution of the average power in a time-series. One PSD estimate called the periodogram is defined by

$$P(c) = \frac{S(c)S^*(c)}{B} \qquad c = 0, 1, \cdots, \frac{B}{2} \tag{2.5}$$

where $S(c)$ is the B-bin Discrete Fourier Transform (DFT) of the b-sample time-series $s(n)$, and is given by

$$S(c) = \frac{2}{b}\sum_{n=0}^{b-1} s(n)e^{-j\frac{2\pi}{B}} \qquad c = 0, 1, \cdots, \frac{B}{2} \tag{2.6}$$

where the global domain is that of frequency and (*) indicates the complex conjugate.

It has been found [52] that retaining the first 12 spectral bins of a 64-bin DFT is sufficient to capture the most significant spectral information in these signals. Each 512-sample scan is thus transformed into a 12-point PSD estimate.

The vertical uncertainty of the results is reduced by localising the detected reflections along the time axis. this is achieved by segmenting the scan into sections, and extract spectral information of only those sections containing legitimate target reflections. Each scan is sectioned into eight contiguous 64-sample segments, as illustrated in Figure 2.5. For each signal segment, the logarithm of the 64-point windowed power spectral density is extracted as a discriminating feature, and only the first 12 spectral samples are retained. The chosen window for this application is the Hanning window given by

$$w(n) = \begin{cases} \frac{1}{2}\left(1 + \cos\frac{n\pi}{J}\right) & |n| \leq win \\ 0 & |n| > win \end{cases} \tag{2.7}$$

where *win* is the length of the window.

The periodogram suffers from several drawbacks [53], among them an excessive variance. Bartlett [54] suggested that the variance would be reduced if the time-series segment is divided into subsets, with the periodogram then computed for each subset and the average energy density obtained for each frequency in order to obtain a greater reduction in variance. This was implemented on the radar data, and as a result, the segmentation has become more sensitive to the presence and the location of the target.

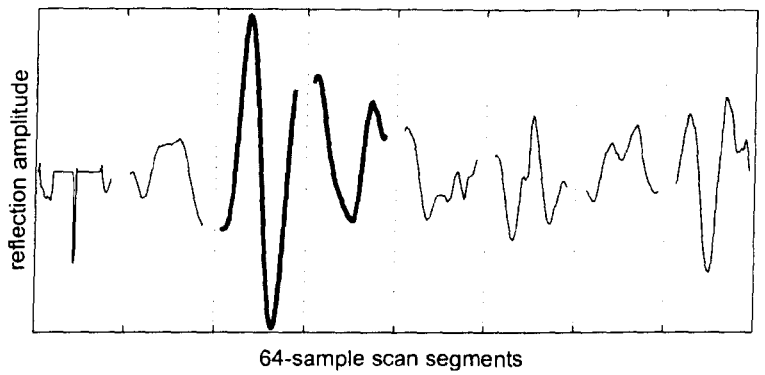

Figure 2.5: Illustration of an A-scan sectioned into eight 64-sample segments

Time-frequency techniques

The Wigner-Ville distribution (WVD) is a widely-applied time-frequency technique in a variety of applications. It is defined as

$$W_s(t,f) = \int_{-\infty}^{+\infty} s(t+\tau/2)s^*(t-\tau/2)e^{-j2\pi f\tau}d\tau \tag{2.8}$$

Knowing that the instantaneous autocorrelation function $R_s(\tau,t)$ of a signal $s(t)$ is given by

$$R_s(\tau,t) = s(t+\tau/2)s^*(t-\tau/2) \tag{2.9}$$

The Fourier transform of $R_s(\tau,t)$ provides the instantaneous spectral density function

$$D_s(f,t) = \int_{-\infty}^{+\infty} e^{-j2\pi f\tau}d\tau R_s(\tau,t) \equiv W_s(t,f) \tag{2.10}$$

It can be seen that the Wigner-Ville distribution function of a signal can be viewed as an instantaneous spectral density.

The reason that makes the WVD so special in many signal-processing applications is that it better characterises a signal's frequency changes than any other schemes [55]. In addition, the WVD possesses many useful properties for signal processing, many of which are related to the average of the WVD. One of the major deficiencies of the WVD is the cross-term interference. This was reduced by using the so called *analytic signal* (or *pre-envelope*) associated with the real signal. Let $u(t)$ be a real square-integrable signal in time, then the corresponding analytic signal is defined as

$$s(t) = u(t) + jh(t) \tag{2.11}$$

where $h(t)$ is *Hilbert Transform* of $u(t)$.

This method would reduce the cross-term interference but on the expense of losing useful properties. Figure 2.6 shows two distributions, one of a cylindrical target-signal and the other of a non-target signal.

After the WVD-distribution is found for a certain GPR reflection, the magnitude of the peak corresponding to each instant of time is taken as one feature. A second feature is extracted, which represents the magnitude of the peak corresponding to the maximum frequency value in the WVD. Figure 2.7 shows plots of these two features for signals reflected from target and non-target objects. Because of the high time-cost of the WVD, each signal is divided into 64-bit segments (similar to the periodogram case) and the chosen features were extracted correspondingly.

A major drawback in the WVD method is its extremely-high time cost when compared to other methods presented in this study (as this will be shown later in this chapter), which makes it unsuitable for the automatic detection system as it eliminates the crucial objective of near-real time performance.

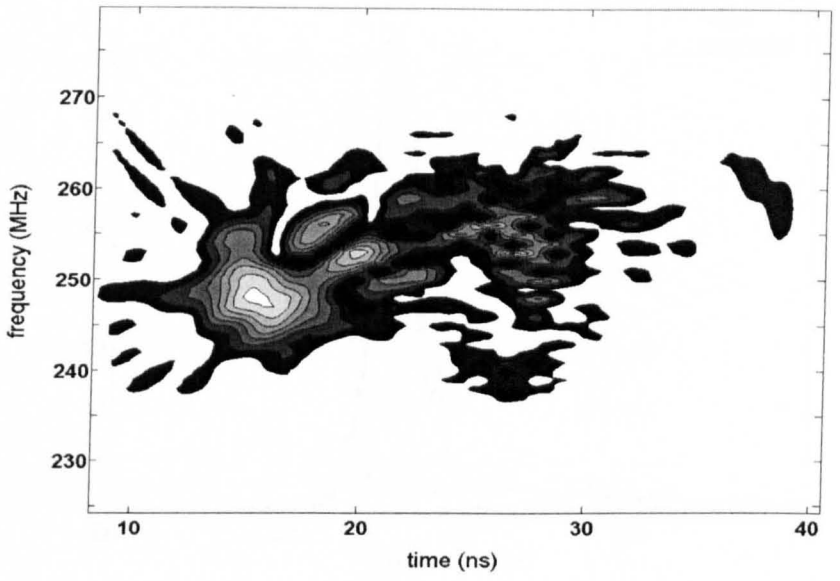

(a) WVD of an A-scan containing a target reflection

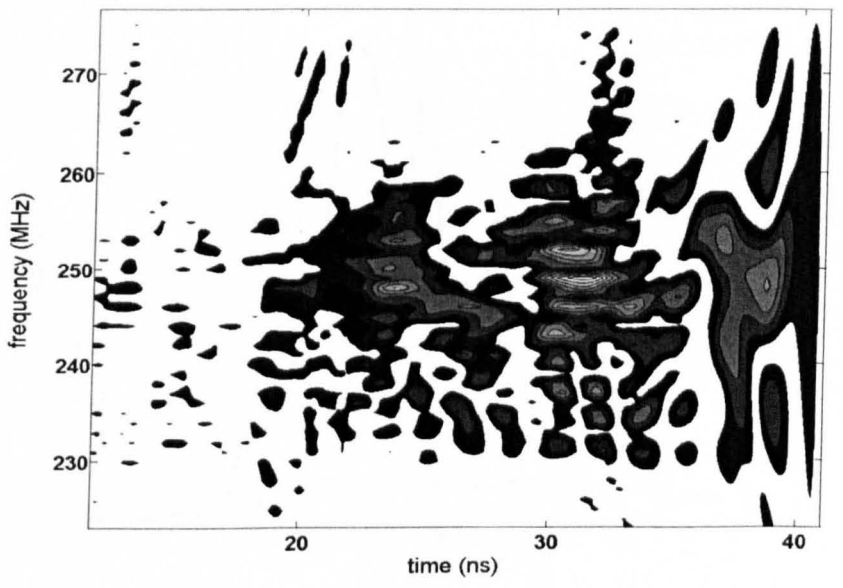

(b) WVD of an A-scan containing no target reflections

Figure 2.6: Wigner-Ville distribution for A-scans with and without target

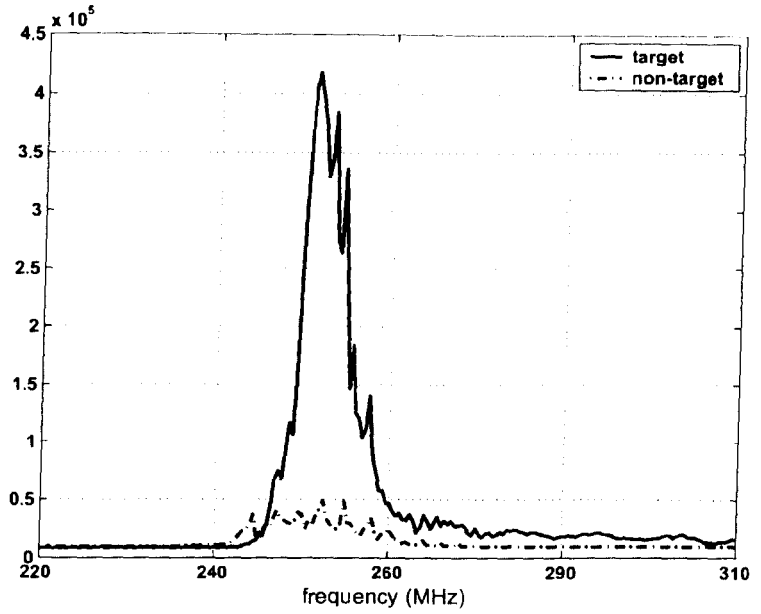

(a) Magnitude of the peak of maximum frequency

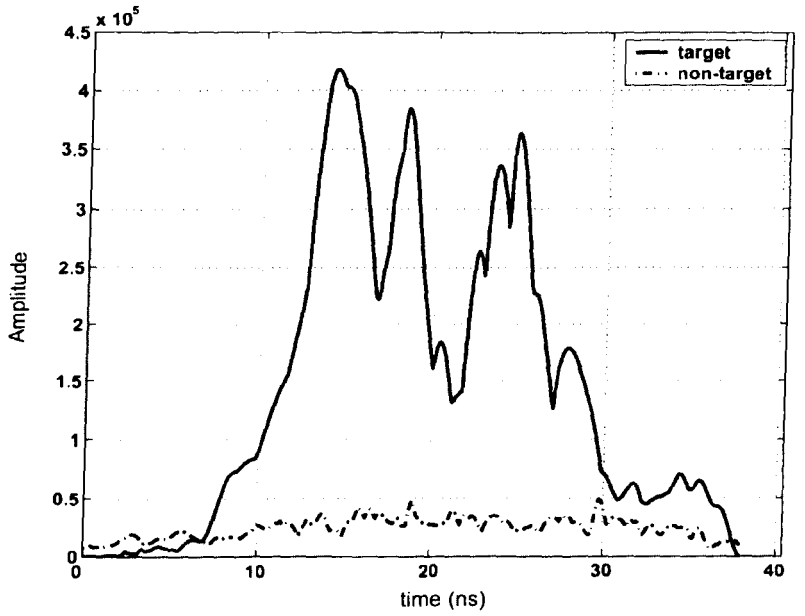

(b) Magnitude of the peak for time instants

Figure 2.7: Magnitudes of peaks corresponding to frequency and time values in WVD for target and non-target signals

Another widely-applied time-frequency distribution is the short-time-fourier-transform (STFT). Although Fourier analysis allows passage from the time domain to the frequency domain, its use is concerned mainly with stationary signals whose properties do not evolve with time. It does not allow a combination of the two domains, and in particular, most *temporal* information is not easily accessible in the frequency domain. While the spectrum shows the overall strength with which each frequency is contained in the signal, it does not generally provide information about the time localisation of spectral components [56]. Any abrupt change in time in a non-stationary signal is spread out over the whole frequency axis of the Fourier transform. Fourier analysis is based on global information which is not adequate for the study of compact or local patterns. Therefore an analysis adapted to non-stationary signals requires more than the Fourier transform [55]. The STFT is one of the commonly used time-frequency techniques for this purpose. It is defined by

$$\underset{s}{\text{STFT}}^{w}(t,f) = \int_{\tau} s(\tau)w(\tau - t)e^{-j2\pi f\tau}\, d\tau \tag{2.12}$$

and in discrete form for a time-series $s(n)$ consisting of b samples,

$$\underset{s}{\text{STFT}}^{w}(i,p) = \sum_{n=0}^{b} s(n)w(i-n)e^{-j\frac{2\pi ci}{b}} \tag{2.13}$$

where $i, p = 0, 1, 2, \cdots, b-1$

The STFT, or windowed Fourier transform introduces a frequency dependence with time by filtering a signal "at all times" with a band-pass filter centred at each individual frequency and whose impulse response is that of the window function $w(i-n)$. This produces a "local spectrum" of the signal $s(n)$ around the analysis

time i. The ensemble of the corresponding power spectra for all times produces a two dimensional time-frequency representation known as a *spectrogram.*

$$\mathrm{SPEC}_{s}^{w}(i,p) = \left|\mathrm{STFT}_{s}^{w}(i,p)\right|^{2} \tag{2.14}$$

which is a very common tool in signal analysis because it provides a distribution of the energy of the signal in the time-frequency plane.

The choice of window length is critical in this form of spectral analysis. As stationarity is assumed within the window. The smaller the window size, the better the time resolution. However the smaller the window size also, the more the number of discrete frequencies which can be represented in the frequency domain will be reduced, and therefore the more weakened will be the discrimination-potential between frequencies. The choice of window thus leads to an uncertainty trade-off. Figure 2.8 shows the effect of different window sizes on the time and frequency resolutions when STFT is applied to a typical A-scan reflected from a buried cylinder using an 400MHz radar.

There are two values that are retrieved from the radar file header (see Appendix D), one relating to the acquisition hardware, while the other is concerned with the radar acquisition settings. These are the transmitting antenna centre frequency `antenna_name` (in MHz) and the `range` (in ns). From these values, and knowledge of b, the number of samples in each scan (equivalent to `samples_per_scan` in the file header), the optimum window length can be computed as shown below

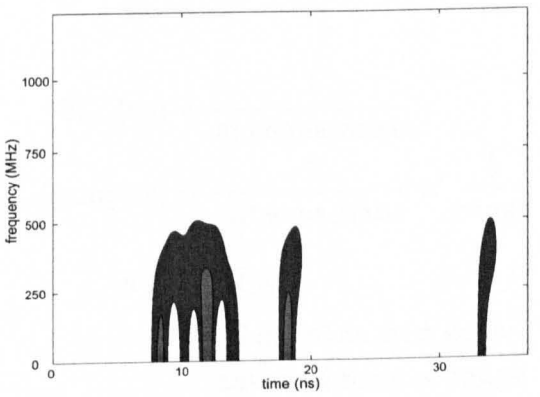

(a) Window length of 30 samples

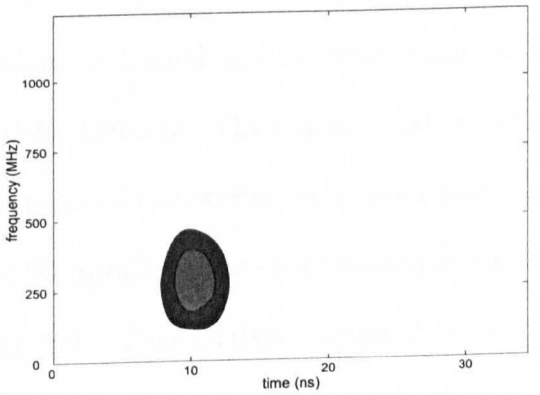

(b) Window length of 64 samples

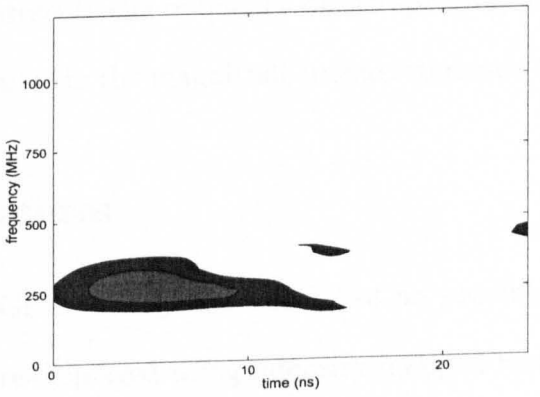

(c) Window length of 200 samples

Figure 2.8: Effect of choice of window length on the spectogram time and frequency resolutions

$$T_{ant}(\text{ns}) = \frac{1}{\texttt{antenna\_name}} \tag{2.15}$$

$$T_{ant}(\text{samples}) = \frac{1}{\texttt{antenna\_name}} \times \frac{b}{\texttt{range}} \tag{2.16}$$

$$win = 2\,T_{ant} \tag{2.17}$$

$$= \frac{2\,\texttt{samples\_per\_scan}}{\texttt{antenna\_name} \times \texttt{range}} \tag{2.18}$$

For the radar data shown in Figure 2.2, with antenna frequency 400 MHz, range 40 ns and 512 samples per scan, the window length is computed as 64 samples.

The spectrogram surfaces are analysed at every time step in order to quantify the time series characteristic features. The features extracted are the frequency and magnitude of the largest peak of the spectrum at each point on the time axis. This is achieved by examining the profile of the spectrogram along the time and frequency axes, as shown in Figure 2.9. This analysis, applied to each scan, associates two quantities with each point in the radargram, and the effect is the generation of two images: a "magnitude image" and a "frequency image". The value of each point in the frequency image represents the frequency of the spectrogram peak at that point, and the corresponding value in the magnitude image represents the value of this peak.

2.2.2 Spatial Features

Although in origin GPR radargrams consist of an ensemble of time-series, the manner in which they are displayed using intensity-mapped raster images lends itself naturally to visual interpretation whereby the trained operator would manually point out regions of interest from the two-dimensional images relying on certain visual cues in order to issue a judgement. He inspects the image and associates regions of similar

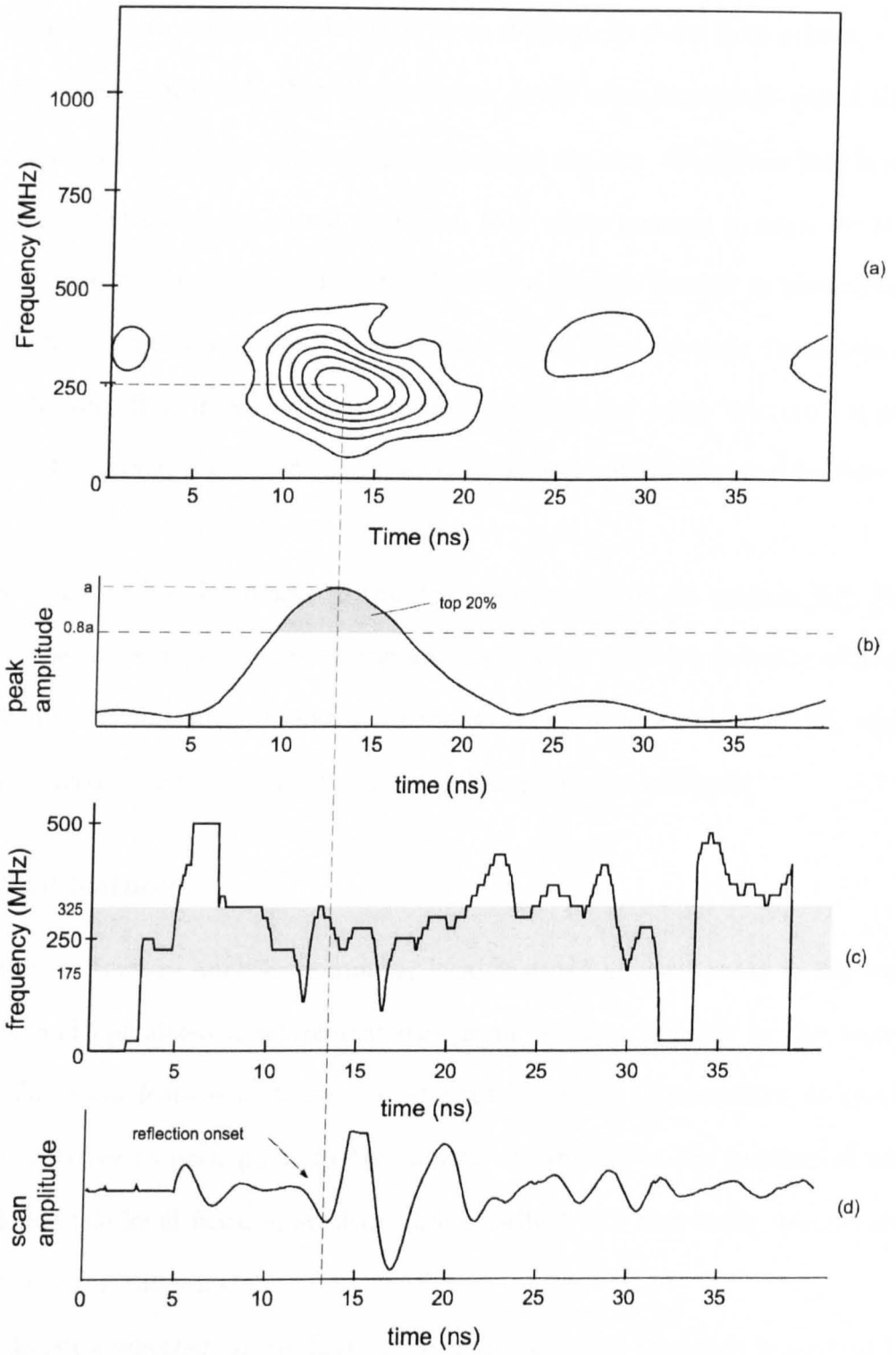

Figure 2.9: Frequency and amplitude analysis and selection of spectrogram
(a) Spectrogram of scan containing reflection
(b) Peak amplitudes at each time sample, with threshold
(c) Peak frequency at each time sample, with selection
(d) Time domain signal containing reflection

"appearance" with certain labels, in order to distinguish them from others.

It has been shown [57], that *visual texture* is the most important visual cue used to manually identify such types of homogeneous regions. Studies in psychophysics [58] have investigated the visual processes that allow humans to separate features in images using texture cues. This has lead to a greater interest in identifying and quantifying the perceived qualities of texture in an effort towards automatic image interpretation. It is important here to mention that the term "texture" is used to represent the *visual* texture of the radar images, and not the physical texture of the soil.

The considerable differences in the definitions available for texture [51], [59], in terms of the concepts, applications and approaches has lead to a diversity of methods for utilising and interpreting texture. Among the most successful [60], [?], and [51] texture analysis techniques are the statistical and regional methods.

Statistical features

Statistical texture analysis computes local features at each point in the image-segment, and calculates a set of statistics from the distributions of the intensity levels. The local feature is defined by the combinations of intensities at specified positions relative to each point in the image. According to the number of points which define the local feature, statistics are classified into first-order, second-order, and higher-order statistics.

The decision whether to use first-order or higher-order statistics is governed by few factors such as the type of texture, the number of classes to distinguish between, the minimum required accuracy, and the system-complexity. Consequently, it is important to make the right choice corresponding to the required task.

Statistical descriptors are computed from the local pixel statistics of the intensity histogram (probability of occurrence). In this case of B-scans, the problem is viewed as an image-processing one. In fact statistical analysis computes local features at each point in the image-segment, and calculates a set of statistics from the distributions of the intensity levels.

The technique works on the basis of a rectangular window that scans the radargram vertically and horizontally, then the histogram of each windowed-segment is characterised using statistical descriptors which are functions of the pixel intensity distribution $h(i)$ within the windowed region centered at an arbitrary point (x, y). These descriptors are

1. Variance (second moment):

$$\sigma_h^2 = \sum_{i=1}^{g} (i - \mu_h)^2 \, h(i) \tag{2.19}$$

2. Skewness (third moment):

$$\sum_{i=1}^{g} (i - \mu_h)^3 \, h(i) \tag{2.20}$$

3. Kurtosis (fourth moment):

$$\sum_{i=1}^{g} (i - \mu_h)^4 \, h(i) \tag{2.21}$$

4. Entropy:

$$-\sum_{i=1}^{g} h(i) \, \log h(i) \tag{2.22}$$

where g is the number of data points (pixels) in the scanning window, and μ_h is the mean of the pixel intensity distribution in the window.

The discrimination capability between targets and non-targets is tested by performing a hierarchical tree unsupervised clustering (as described before) for a data set specially built for this purpose, which contains windowed segments of data representing targets and non-targets. The selected features were extracted for each window in the data set then the unsupervised clustering was applied. The resulting hierarchical tree can be seen in Figure 2.10.

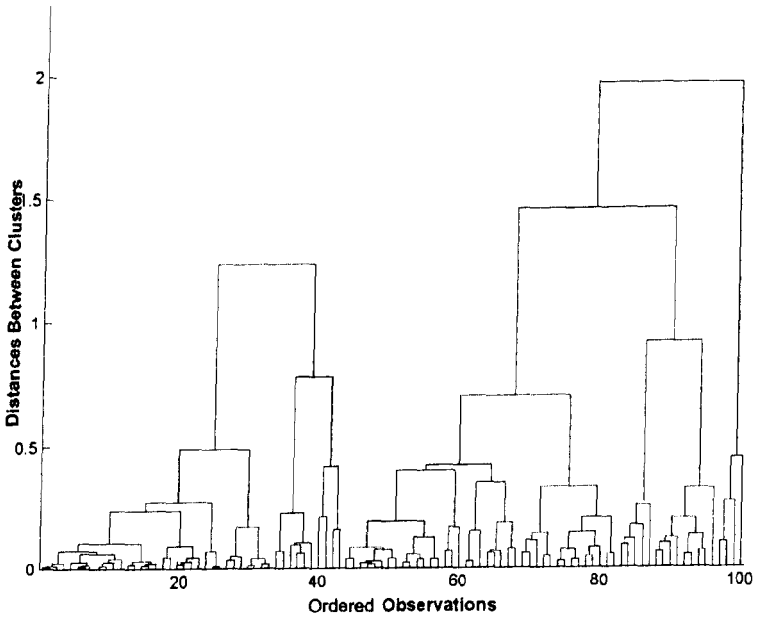

Figure 2.10: Unsupervised hierarchical tree test showing discrimination capability of the chosen descriptors for B-scans

A window overlapping was used in order to further reduce any unnecessary regions that do not contain target data. It involves setting vertical and horizontal overlap percentages for the segment window so that it can be used in the subsequent neural network classification stage, where each region is classified more than once, and this

will make the selected regions include only the targets of interest as the overlapping percentages increase. As a result to this, the time cost would increase as the number of loops, calculations and memory size increase. Consequently, a right choice of the overlapping percentage must be made in a manner that balances between non-useful data reduction and the spent time. To make this process easier, one can derive a mathematical relationship that combines time, and degree of overlap so that the user can chose whether he wants to spend some extra time on targets shaping or not. For an image data of size $n \times m$, the number of horizontal windows N_h of size $x \times y$ across the image is given by

$$N_h = \left\lceil \frac{n}{x} \right\rceil \tag{2.23}$$

while the number of vertical windows N_v down the image is given by

$$N_v = \left\lceil \frac{m}{y} \right\rceil \tag{2.24}$$

hence the total number of windows is given by

$$N = N_h \times N_v \tag{2.25}$$

Then time function in seconds can be written as

$$t = \frac{(N-1)}{k \times p} + 1 \tag{2.26}$$

where p is the fractional degree of overlap, while k is a constant and it is estimated to be 200.

Regional features

Until now, all the methods which have been described in the previous sections are concerned with detecting a single reflection or a band of reflections that correspond to the reflections from buried cylinders while rejecting the others. In this section, a new approach is presented that aims at selecting the hyperbolic shapes that result from buried cylinders. The main idea behind this approach is to consider the radargrams as whole images containing different-shaped regions, then the hyperbolic-shaped regions are to be distinguished from other ones in these images. This process is referred to as image segmentation. Automatic segmentation techniques can be put into one of four categories

1. Thresholding techniques
2. Boundary-based techniques
3. Region-based techniques, and
4. Hybrid techniques

In this study, the used technique is a hybrid one that combines the region-based and thresholding categories. It relies on the assumption that adjacent pixels in the same region have similar visual features such as gray level, colour value, or texture based on which, the image is searched for boundaries and discontinuities.

Detecting discontinuities

There are many approaches that are used to detect meaningful discontinuities. One of the most popular among those is edge detection [51], as edges represent the

most frequently appearing boundaries within images in comparison to point and line-boundaries.

Another popular technique is thresholding, as it provides an easy and convenient way to perform the required segmentation on the basis of the different intensities or colours between the regions of an image.

In our case, a simple thresholding was required where the output should be a binary image with the resulted segments. Black pixels correspond to background and white pixels correspond to foreground (or vice versa). The segmentation is determined by a single parameter known as the *intensity threshold.* The value of this threshold is set in a manner so that the lowest 15% of the pixel intensity values within the whole image are considered redundant. In a single pass, each pixel in the image is compared with this threshold; if the pixel's intensity is higher than the threshold, the pixel is set to one in the output, and if it is less than the threshold, it is set to zero.

The next step is to assign a unique label to each detected region via assigning a single yet distinctive value for all the pixels in each region, as follows

$$R_k = k \qquad\qquad k = 1, 2, 3, \cdots, N \tag{2.27}$$

where R_k is the k^{th} region in an image that contains N regions. Figure 2.11 shows the result of thresholding a typical radargram. To this point, an image which consists of N regions is obtained and is ready for the following features extraction process for each one of these regions.

Chosen features

The process of deciding which features are most adequate in distinguishing hyperbolic-shaped regions from other ones, requires that different regional descriptors

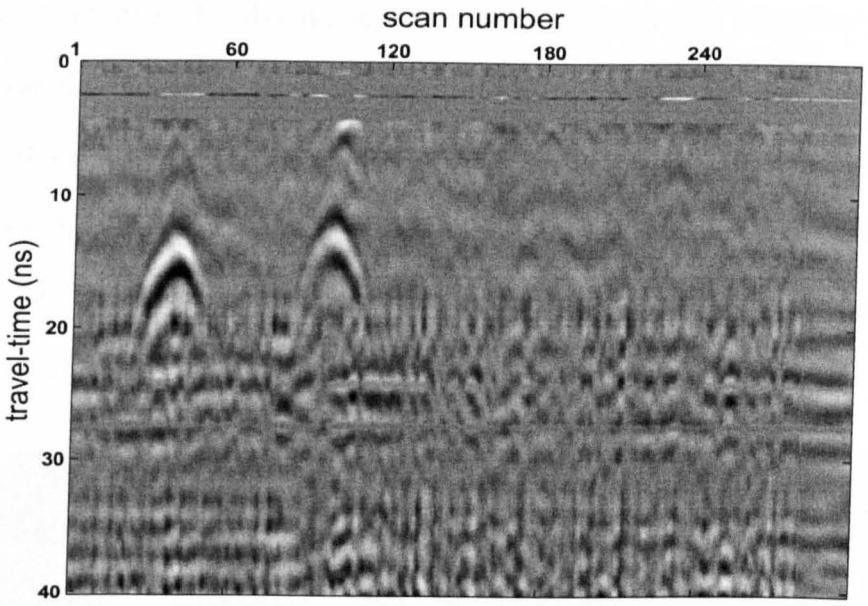

(a) Original radargram

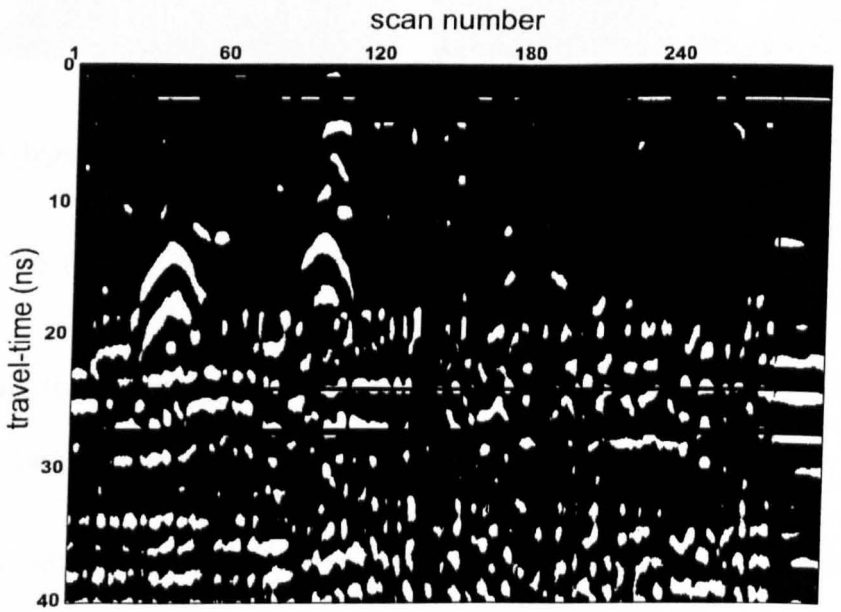

(b) The radargram after applying simple thresholding

Figure 2.11: Result of applying thresholding

are investigated separately and collectively, then the ones which are best capable of discriminating between the above-mentioned two classes, are to be chosen.

A data set that contains samples represent each of the two classes was collected. Because of the nature of the selected features, each sample contained only one of either classes; hyperbolic or a non-hyperbolic segments (as in the samples shown in Figure 2.12). To overcome the problem of different sizes of data, the collected segments were resized to fit with other segments which may differ in size.

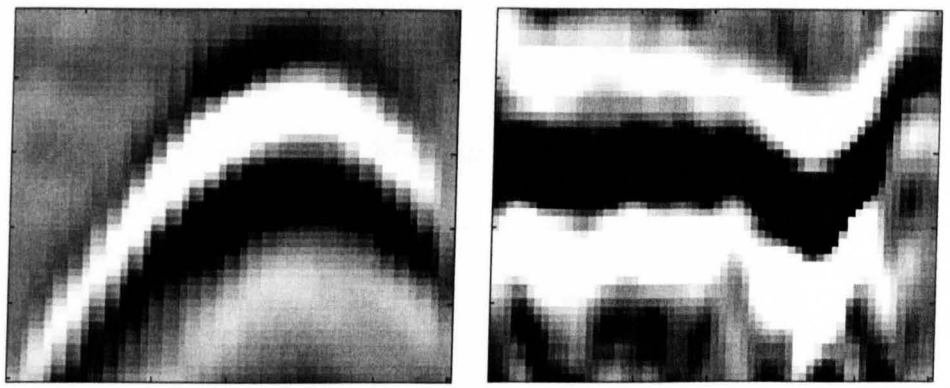

(a) Hyperbolic signature of a pipe (b) Non-hyperbolic signature

Figure 2.12: Resized data representing hyperbolic and non-hyperbolic signatures

As a result for features investigation, the following features are found to best distinguish between hyperbolic and non-hyperbolic-shaped regions:

1. Area: represents the actual number of pixels in the region, and is given by

$$A_R = \sum_{i}^{n} \sum_{j}^{m} R(i,j) \tag{2.28}$$

2. Equivalent Diameter: represents the diameter of a circle with the same area as the region, and is given by

$$ED_R = 2\sqrt{\frac{A_R}{\pi}} \tag{2.29}$$

3. Extent: represents the area of the region divided by the area of the smallest rectangle containing that region, and is given by

$$\text{Extent}_R = \frac{A_R}{A_{rectangle}} \tag{2.30}$$

where $A_{rectangle}$ is given by

$$A_{rectangle} = (i_{max} - i_{min})(j_{max} - j_{min}) \tag{2.31}$$

4. Major Axis Length: represents the length of the major axis of the ellipse that has the same second moment as the region.

5. Minor Axis Length: represents the length of the minor axis of the ellipse that has the same second moment as the region.

6. Convex Area: represents the area of the smallest convex polygon containing the region.

7. Solidity: the area of the region divided by the area of the smallest convex polygon containing that region.

This method has a good property that it considers all the regions to be classified in GPR radargram of same weight, i.e once the global thresholding is applied, all thresholded regions are set to ones. The choice of a certain region will then depend on the features of that region. Consequently, the probability of missing weak targets would be reduced to a high extent.

Tables 2.1 and 2.2 summarise the features which have been used for each one of the methods described in the previous sections.

Table 2.1: Time-series (A-scans) feature selection subsets

Statistical Features	**Spectral Features**		
	Periodogram	WVD	STFT
Variance Mean absolute deviation Fourth moment	Logarithm of the windowed periodogram	Magnitude of the largest peak at each time instant Frequency at which spectrum magnitude is largest	Magnitude of the largest peak at each time instant Frequency at which spectrum magnitude is largest

Table 2.2: Spatial (B-scans) feature selection subsets

Statistical Features	Regional Features
	Area
Variance	Equivalent Diameter
Skewness	Extent
Kurtosis	Major axis length
Entropy	Minor axis length
	Convex Area
	Solidity

2.3 Classification

In order for the automatic segmentation process to be complete, the selected features need to be employed into a classification mechanism. One of the most successful approaches in this field is artificial neural networks. They have proven to be rapid, accurate, and most importantly consistent in classifying and simplifying complex data.

2.3.1 Neural Networks

Neural networks, with their ability to derive meaning from complicated or imprecise data, can be used to extract patterns and detect trends that are too complex to be noticed by either humans or other computer techniques. A trained neural network can be thought of as an "expert" in the category of information it has been given to analyse. This expert can then be used to provide projections given new situations of interest, a property called "generalisation".

All artificial neural networks take numeric input and produce numeric output. To capture the essence of biological neural systems, an artificial neuron receives a

weighted number of inputs (either from original data, or from the output of other neurons), and responds by producing an activation signal. The activation signal is passed through a transfer function (also known as an activation function) to produce the output of the neuron. This is based on the original model for the neuron proposed by McCulloch and Pitts [61].

To illustrate this, consider a neuron with n inputs $in_1, in_2, \cdots, in_n$ and corresponding weights $w_1, w_2, \cdots, w_n$. The activation signal is given by

$$\text{net} = w_1 in_1 + w_2 in_2 + \cdots + w_n in_n \tag{2.32}$$

$$= \sum_{i=1}^{n} w_i in_i \tag{2.33}$$

This activation is subjected to a (usually) nonlinear activation function, and the result is the output of the neuron. This transfer function is selected so as to accept input of an unlimited range, and produce output on a restricted range. One common such saturating nonlinearity is the *logistic* S-shaped (*sigmoidal*) function shown in Figure 2.13.

$$\text{out} = f_{\text{sig}}(\text{net}) = \frac{1}{1 + e^{-\text{net}}} \tag{2.34}$$

In addition to being bounded, it also has the desirable properties of being both smooth and easily differentiable. The hyperbolic tangent function is very similar to this but with an output range of -1 to 1. Indeed f_{sig} and f_{tan} are related thus

$$f_{\text{tan}}(\text{net}) = 2f_{\text{sig}}(2\text{net}) - 1 \tag{2.35}$$

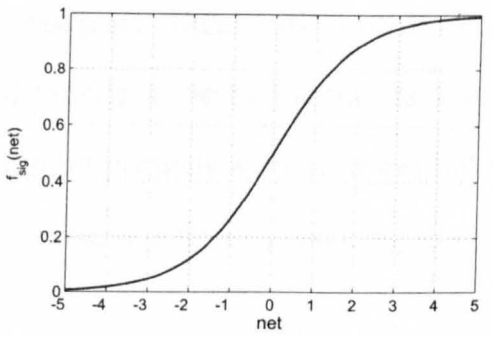

Figure 2.13: Sigmoidal transfer function `logsig`

There are two main types of learning strategies used with neural networks, with different types of network using different types of training. These are *supervised* and *unsupervised* learning. In supervised or associative learning the network is trained by providing it with matching output patterns, whereas in unsupervised learning or self-organisation the system discovers statistically salient features of the input population with no *a priori* set of classification categories. Figure 2.14 shows a typical feedforward network (similar to the one used in this study), where neurons are arranged in a distinct layered topology.

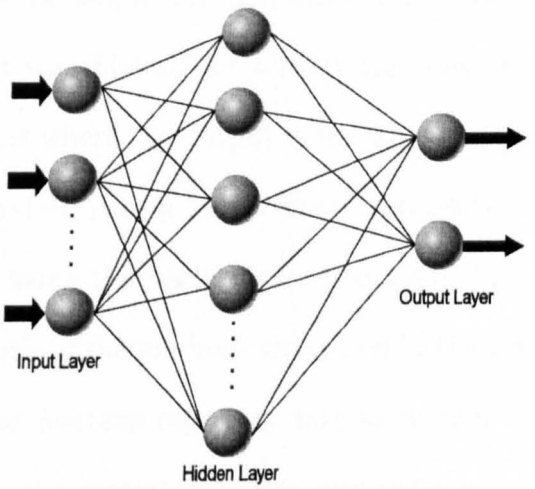

Figure 2.14: Feedforward multi-layer perceptron neural network with one hidden layer

This stage provides subsequent stages with a continuous measure of confidence as to whether a particular radargram section is the result of reflection from a target or not. By rejecting radargram portions with measures below a certain threshold, a data reduction may be achieved, significantly reducing the computational burden for further stages.

Supervised neural networks

In a supervised neural network, the network user assembles a set of training data consisting of vector training pairs. Each training pair is composed of an input (pattern) vector and a target (class) vector. The target vector represents the set of values *desired* of the network when the input vector is applied. The training set must provide a full and accurate representative sample of the problem domain.

The neural network is then trained using one of the supervised learning algorithms (*backpropagation* in this case), which uses the data to adjust the network's weights and thresholds so as to minimise the error in its predictions on the training set. If the network is properly trained, it has then learned to model the (unknown) function which relates the input variables to the output variables, and can subsequently be used to make predictions where the output is not known.

The presented supervised-neural-networks are three-layer feedforward neural networks that are trained using the backpropagation algorithm. They tend to use the features extracted by each of the methods described in the previous sections to make a decision whether these features represent targets or non-targets. This applies to the time-series methods, the spatial statistics, and regional features methods.

Three different data sets were used to train the networks:

1. Signal-based data set, which contains A-scans representing targets and non-targets.

2. B-scans based data set, which contains windowed radargram-segments representing targets and non-targets.

3. Region-based data set, which contains hyperbolic-shaped and non-hyperbolic-shaped regions.

The data contained in these sets is randomly-selected from a variety of radargrams. This ensures the resulting segmentation takes into account a wide spectrum of radargrams to maintain a degree of consistency in classification. All data sets were divided into training, validating, and testing sets; 20% of each data set was assigned for training, 40% was assigned for validation, and 40% for testing. The number of input neurons for each network is equal to the number of features extracted in each method. For all the feature sets, the network parameters were set to the values in Table 2.3.

The trained and calibrated neural classifier is then applied to the features derived from the data sets using each of the techniques discussed, outlining regions of interest corresponding to specific localised targets, in this case buried utility pipes.

Table 2.3: Configuration parameters for neural network classifiers

Parameter	**Values**			
	A-scan Statistics	**WVD**	**B-scan Statistics**	**Regional Features**
Number of input neurons	3	2	4	7
Number of hidden neurons	7	5	15	27
Number of output neurons	2	2	2	2
Input data normalisation	$[-1, 1]$	$[-1, 1]$	$[-1, 1]$	$[-1, 1]$
Input layer transfer function	sigmoid	sigmoid	sigmoid	sigmoid
Hidden layer transfer function	sigmoid	sigmoid	sigmoid	sigmoid
Output layer transfer function	linear	linear	linear	linear
Learning rate η_{lr}	0.02	0.02	0.02	0.02
Learning rate increase η_{up}	1.05	1.05	1.05	1.05
Learning rate decrease η_{down}	0.7	0.7	0.7	0.7
Maximum error ratio η_{er}	1.04	1.04	1.04	1.04
Momentum constant α_{mom}	0.9	0.9	0.9	0.9
Samples retained for training	20 %	20 %	20 %	20 %
Samples retained for validation	40 %	40 %	40 %	40 %
Samples retained for testing	40 %	40 %	40 %	40 %
Recall output threshold value	± 0.7	± 0.8	± 0.7	± 0.6

2.4 Results

As it is impractical to show classification results for all radargrams within a site, a single representative radargram is chosen to show these results. This radargram represents `file 47` taken from a controlled test site [49] is shown in Figure 2.2, and it contains two hyperbolic signatures representing two buried pipes. Figure 2.15 shows the classification result achieved by the A-scan statistical-features based method. The results of spectral features techniques are shown in Figures 2.16 and 2.17. It is to be said here that the good results achieved by these techniques were at the expense of a significantly increased computational cost. It is noted that the masked-STFT features give better result than the WVD features with respect to accuracy and data reduction, as seen when comparing Figures 2.17 and 2.18.

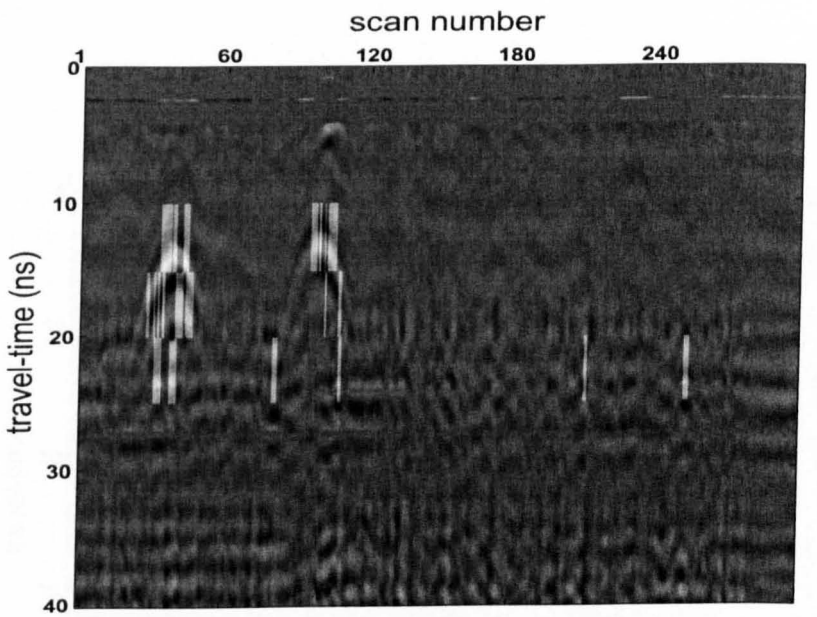

Figure 2.15: Classification result using A-scans statistical features

For the B-scans statistics method, a voting procedure is used, because the overlapping procedure discussed in Section 2.2.2 would result in each windowed segment in

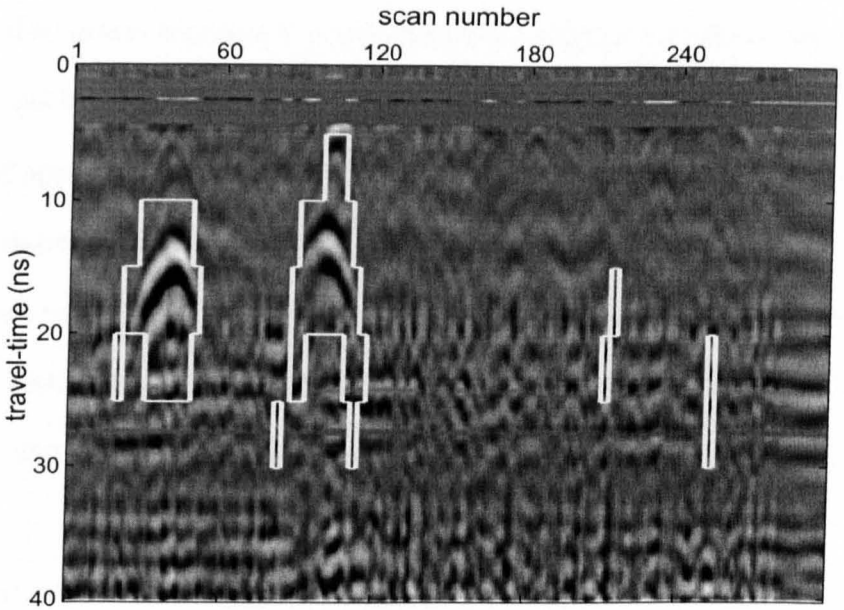

Figure 2.16: Classification result using windowed logarithm of 64-point segments

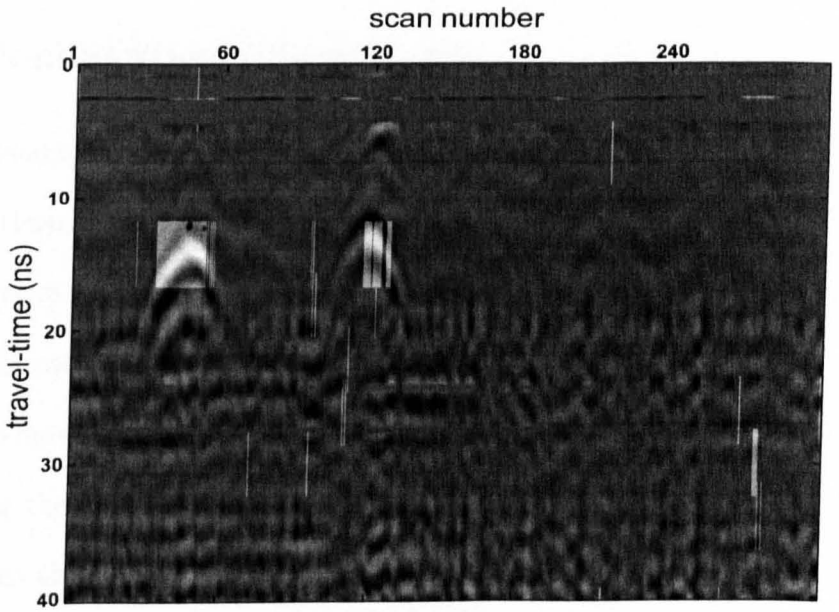

Figure 2.17: Classification result using WVD features

the radargram being scanned more than once. This voting involves setting a threshold on decision if a certain segment is considered as a target or not, and it depends on how many times each segment has been classified as target-containing. Figure 2.19 shows the result of applying this voting, where the darker areas represent higher votes.

The overlapping-voting procedure would add certainty to the process of selecting targets, where only areas classified for three times are chosen while others are rejected. The B-scan statistics technique was particularly successful in differentiating between targets and non-targets in terms of speed, accuracy, and consistency, as shown in Figure 2.20.

Unlike the previous techniques, the region features technique identifies the targets as regions according to their shapes, and this is where the robustness of this technique lies, as only the desired shapes are chosen without the surrounding unwanted regions being selected (as in the other techniques). This can be seen in Figure 2.21.

2.4.1 Double-Stage Classification

A double-stage classification can be applied to GPR radargrams via cascading two of the classification techniques presented in the previous sections, namely the B-scan statistics and the regional features techniques in order to combine the points of strength of each technique.

This is achieved via subjecting the radargram to the classification process twice, first by using the B-scans statistics method, and then by using the regional-features method. Then the resulting masks from both methods are compared so that only the regions that are detected by both methods are kept, whereas others are considered redundant, as this can be seen in Figure 2.22. Here another file (`file 31`) was

Table 2.4: Time consumption for detection methods

Method	Consumed Time (sec)
A-scans statistics	9.44
Windowed periodogram	85.37
WVD Features	153.21
Masked STFT	93.40
B-scans statistics	5.36
Regional Features	3.52
Double stage classifier	9.29

used, because as the classifier was successful in identifying only the three hyperbolae in `file 47` without any regions falsely detected, so the benefit of the double-stage classification will not be seen in `file 47`. Although this cascaded classifier would result in a higher time consumption compared to when using only one method, but this additional time is still acceptable due to the low time costs of the above two techniques. The robustness of this technique would be in further reducing falsely detected regions, while confirming detected targets. Figure 2.23 shows `file 31` before and after the double-stage classification.

The applied classifiers consumed different amounts of time depending on the feature-extraction method used. Table 2.4 shows the time consumed by each method when classifying `file 47`, where all times are obtained by a Matlab 6.5 running on a PC with a dual-Pentium® III 1000 MHz processor and 768 MB RAM. It can be seen that the windowed-periodogram, the WVD features, and the masked-STFT methods have consumed much more time than the rest four methods, which makes them not suitable for near-real time applications.

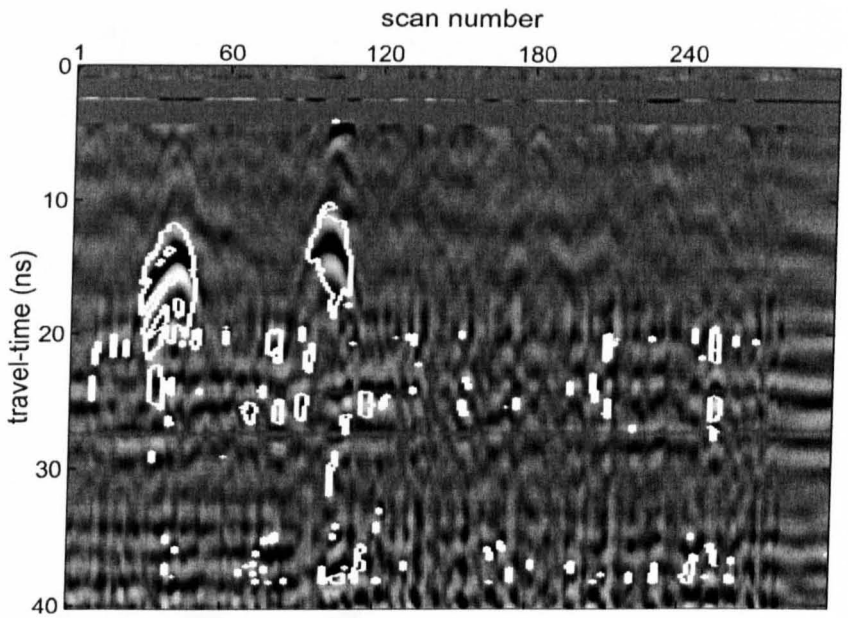

Figure 2.18: Classification result using masked STFT

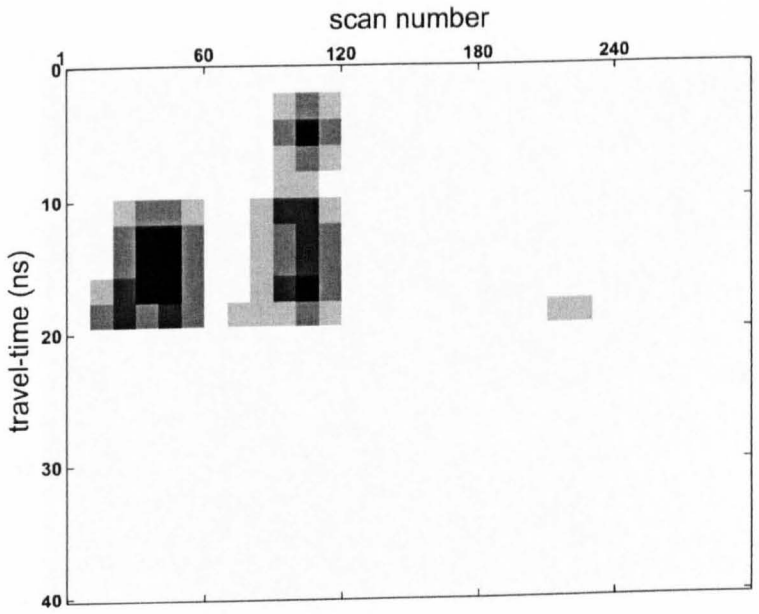

(a) Resulted mask with overlapped windows

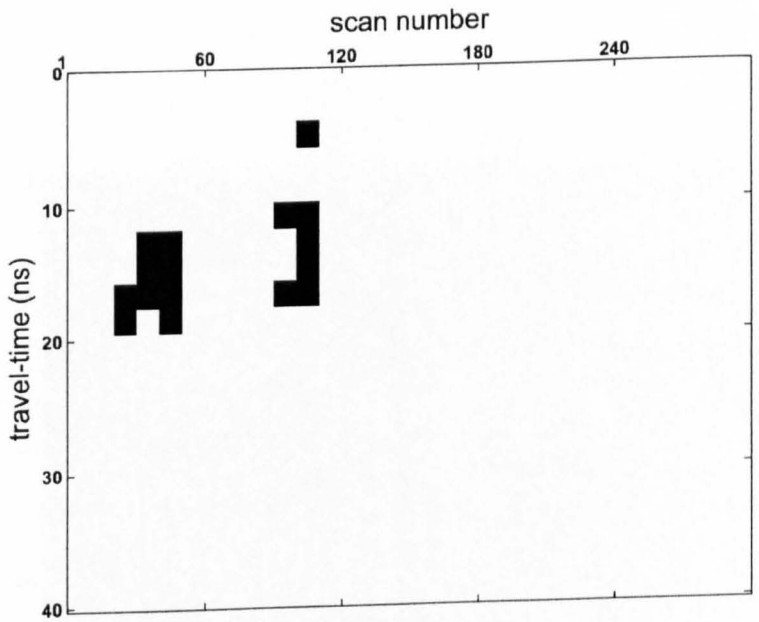

(b) Voting result where only windows with votes > 2 are taken

Figure 2.19: Result of applying voting to the overlapped windows

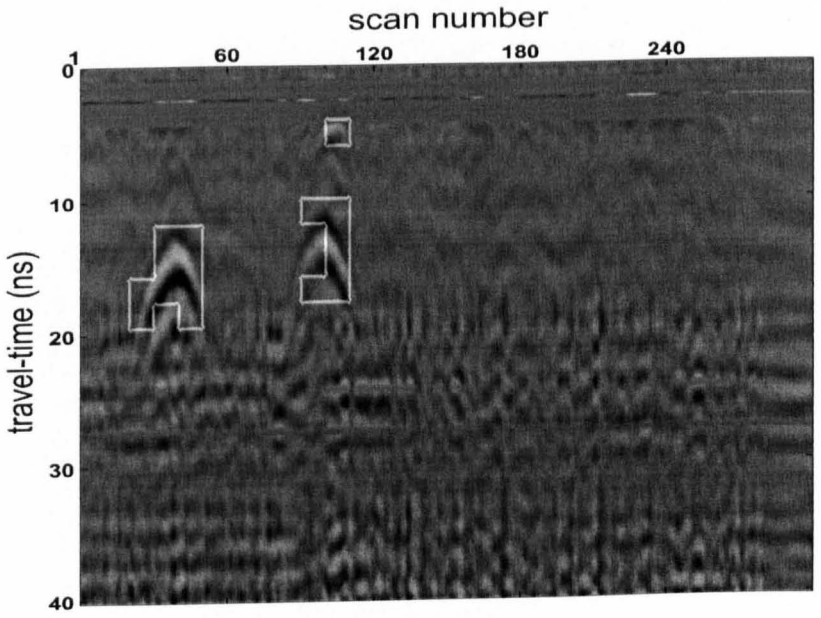

Figure 2.20: Classification result using B-scans statistical features

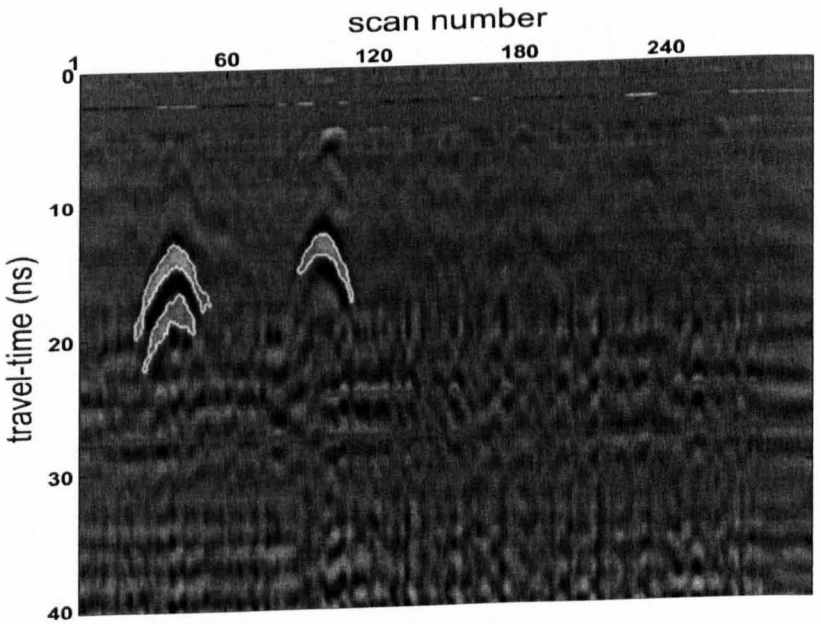

Figure 2.21: Classification result using regional features

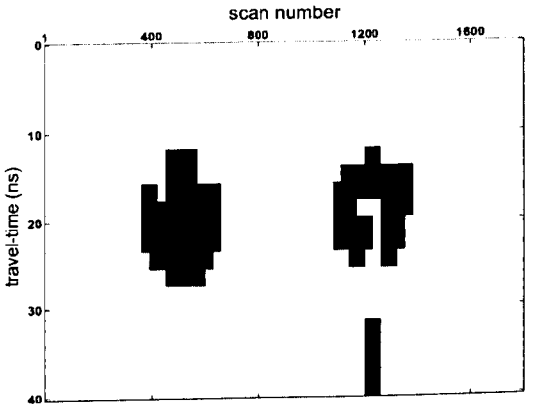

(a) Mask from B-scan statistics method

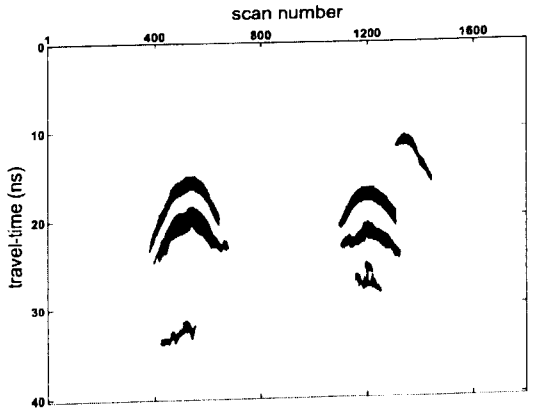

(b) Mask from regional-features method

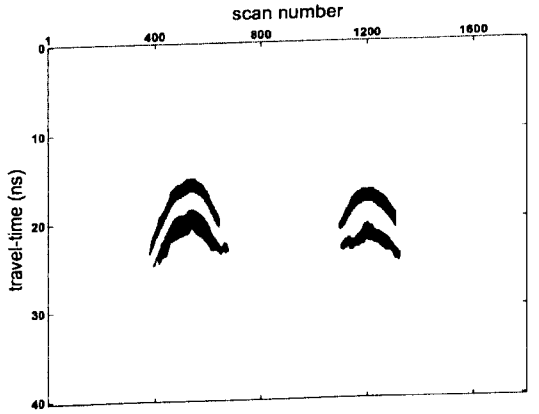

(c) Filtered mask

Figure 2.22: Resulting mask from combining the B-scan statistics and regional-features methods

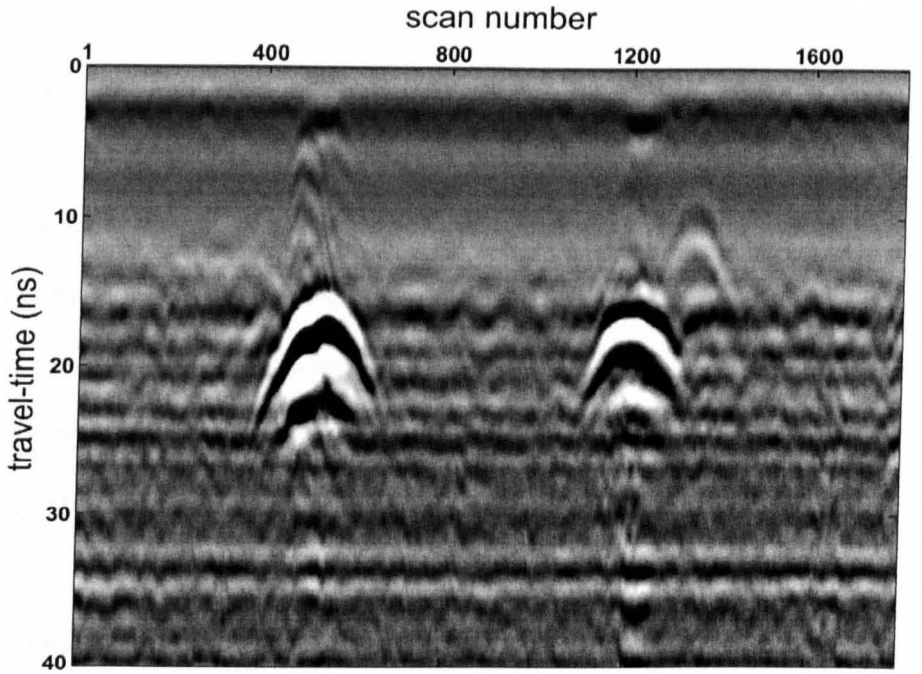

(a) Typical ground-penetrating radar image exhibiting two hyperbolic regions

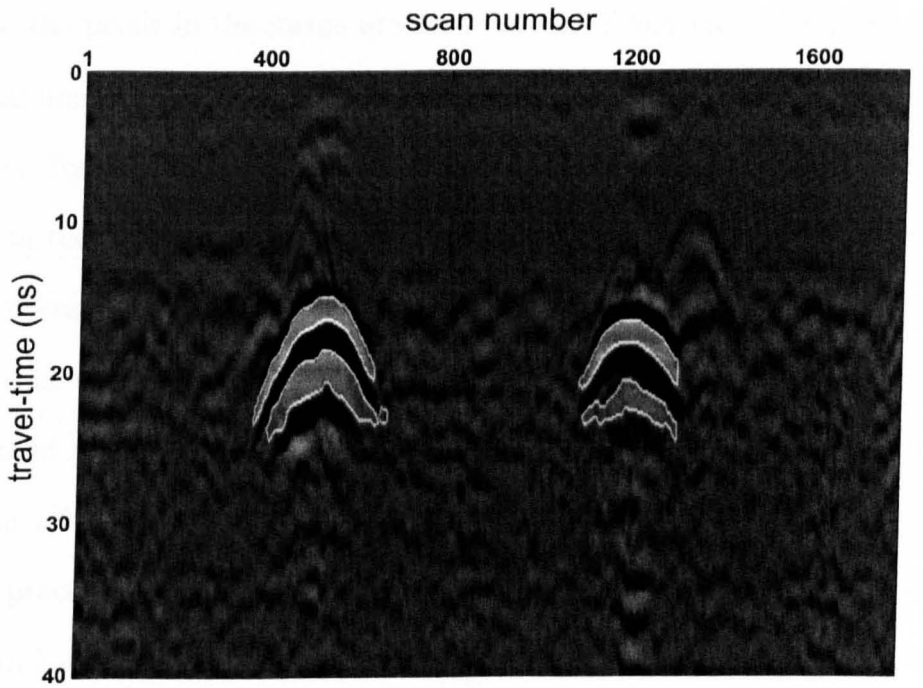

(b) Classification result

Figure 2.23: Classification result using the double-stage classifier

2.5 Image Reduction

The region selection techniques described in this chapter aim at segmenting the input image into regions of interest suspected to be resulted from genuine targets, and other regions that do not contain useful information. In most practical cases, these selected regions constitute only small percentage of the overall images, whereas the majority of each image is redundant. As a result, a large proportion of the GPR data collected during a survey is discarded, while only small zones of interest are visually identified by the operator.

The task of image reduction follows naturally the region selection stage by isolating the regions highlighted as targets from others. This is performed in several steps, as described below. The basis for the image reduction is the binary mask which result from the classification process and used to outline the regions, such as the one shown in Figure 2.24. All the pixels in each detected area in the mask are set to ones, while the rest of the pixels in the image are set to zeros. When multiplying the mask by the original image, then only the detected regions will remain, whereas all others are set to zeros. By using the labels of the detected areas, then each area can be further processed in the subsequent stages. Figure 2.25 shows the multiplication result and how the processing area is highly reduced and limited to only three hyperbolic regions.

When time-series features techniques are involved, then the process of image reduction would not be as easy as in the spatial features techniques. Al-Nuaimy [52] presents an effective procedure for reducing images when time-series features are used. The procedure involves using the number of non-zero pixels in each column of the mask to locate and exclude isolated specks and clusters of spurious points not originating from genuine targets, by retaining only those scans whose pixel profile is

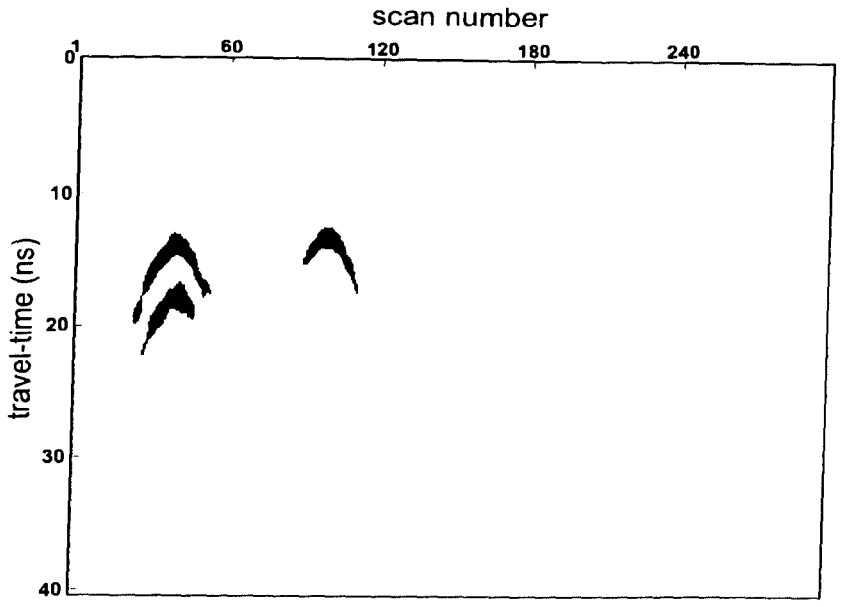

Figure 2.24: Binary mask resulted from regional-features classification method

non-zero for a certain number of scans or certain distance along the surface.

2.5.1 Edge detection

In order to for further detection and characterisation of the desired shapes in an image to take place, then the boundaries of these shapes must be detected. This boundary-detection problem is carried-out via edge detection. The goal behind edge detection procedures is to detect changes in intensity associated with the envelope edges of reflection wavefronts. Several edge detection techniques are available in the image processing literature (e.g. [51]) for this purpose. In the field of GPR most researchers however tend to use less sophisticated techniques for hyperbolic shapes detection, and hence their techniques lack efficiency and suffer from the drawbacks caused by noise and the spurious effects that are often encountered in subsurface surveys. Nagashima [62], for instance simply assigns values of $+1$ and -1 to all the peaks

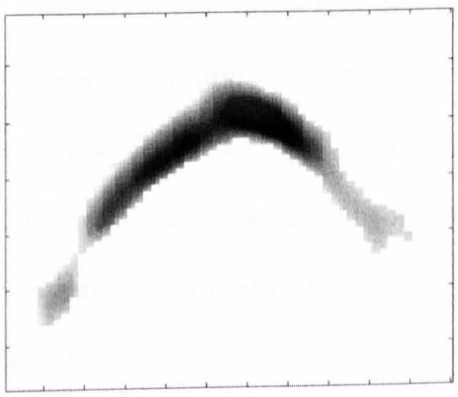

(a) Region 1

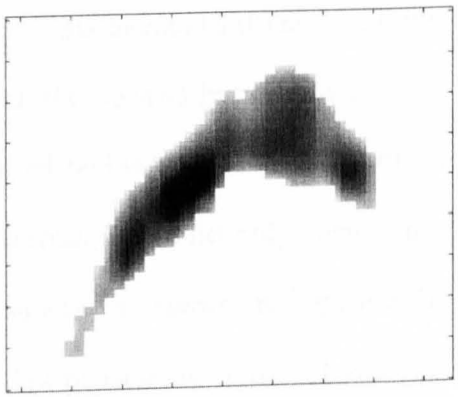

(b) Region 2

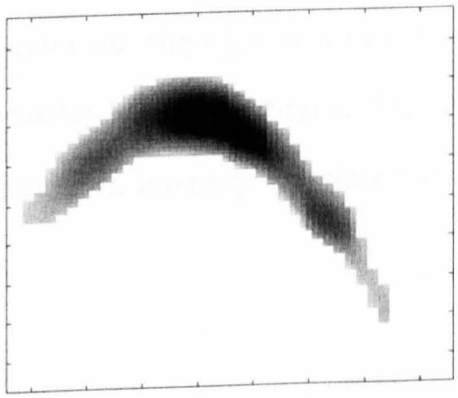

(c) Region 3

Figure 2.25: Original image is reduced to only three regions for further processing

and troughs in the image, while Sato [63] takes this one step further and "extrapolates" in the vicinity of each local maximum in order to locate continuous edge peaks corresponding to wavefront crests. Al-Nuaimy [52] tries to fill this gap by suggesting more sophisticated processing tools to refine and automate the edge detection process, however additional processing is required to detect hyperbolic anomalies, which would lead to additional time cost.

These edge detection processes are necessary to identify hyperbolic signatures within a highlighted area that contains a target or more besides some other regions, as illustrated in Figure 2.20. This means that the highlighted areas are still requiring further processing to extract the desired hyperbolae.

In this study, the presented regional features technique would shortcut these steps by a large extent, as this technique would only result in separated regions and not windowed areas of mixed regions, as shown in Figure 2.21. As a result, the already detected edges need only edge processing that includes region completion and skeletonisation.

In the case where other detection methods are used, then various processing tools are required to refine and automate the edge detection process, such as image contrast enhancement, differentiation, skeletonisation and edge processing with the goal of detecting the abrupt changes in intensity associated with the envelope edges of reflection wavefronts.

Region completion

The reason behind developing this region completion process is that in some incidents, only part of a hyperbolic region is detected and hence this region may not be ready for further processing (such as hyperbola fitting) aiming at extracting target

information. Consequently, such partial regions need to be completed in order for further processing to take place.

The procedure for this process starts with scanning a detected hyperbolic area for symmetry and if that symmetry does not exist, then a horizontal search for the shortest side of the hyperbola is run, this would decide the point where asymmetry starts. Then, a part from the longer side which starts at that same horizontal point is copied. In the last stage, the copied region is mirrored and pasted to the incomplete half. Figure 2.26 shows this region-completion process.

Skeletonisation

A skeletonisation algorithm was developed specifically for the purpose of extracting one-pixel thick segments out of the detected hyperbolic blocks. This is done on a single region basis and takes place after this region passes the *region completion* stage. The procedure is as follows:

- The completed region (with all its pixels values equal to one) is multiplied by the original radargram to retrieve original pixels values for that region.
- A vertical search from left to right is run through the columns forming the region to obtain pixels values of each column.
- The pixels values in each column are replaced by a single value representing the mean of these values.

This skeletonisation algorithm has proven to be very successful when applied to gradient images, as shown in Figure 2.27(c).

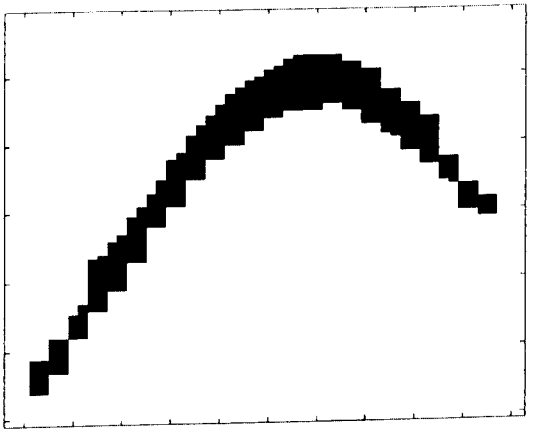

(a) Incomplete hyperbolic region

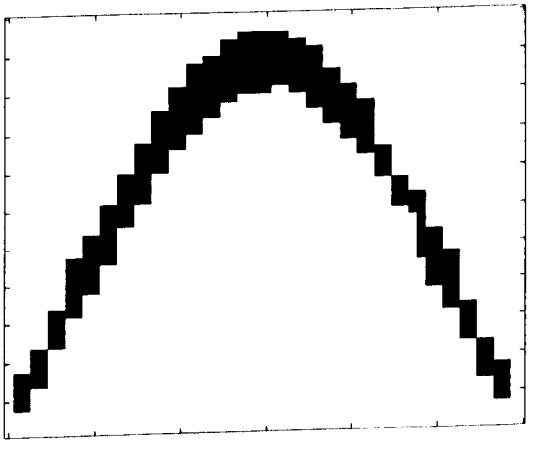

(b) Completed region

Figure 2.26: Region completion process

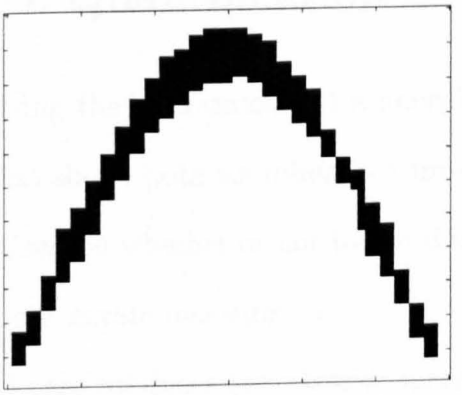

(a) Detected region

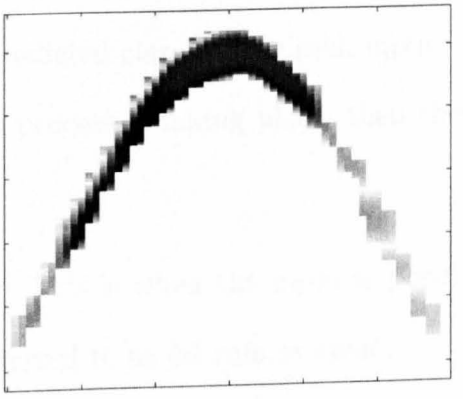

(b) Retrieving original pixels values

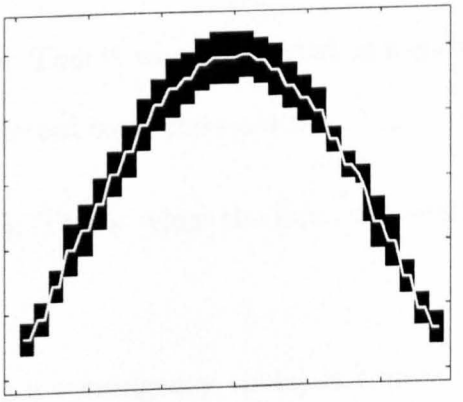

(c) Skeletonisation result

Figure 2.27: Skeletonisation process

2.6 Performance Quantification

The process of quantifying the performance of a neural network classifier needs to be done in a manner that shows both its robust features and weakness points (if any). In this manner, the decision whether or not to use this classifier in a particular application can be based on accurate measures.

The classifier presented here produces two classes; targets and non-targets. The classification process which is taking place is a mapping of a fixed finite set of input parameters into an output set of two classes. This classifier produces a discrete class label indicating only the predicted class for the each input.

When the classification process is taking place, then there are four possible outcomes:

1. **True Positive** (T_p): This is when the input is positive and it is classified as positive. It is also referred to as *hit rate* or *recall*.

2. **False Negative** (F_n): This is when the input is positive and it is classified as negative. It is also referred to as *false dismissal*.

3. **False Positive** (F_p): This is when the input is negative and it is classified as positive. It is also referred to as *false alarm*.

4. **True Negative** (T_n): This is when the input is negative and it is classified as negative.

A *confusion matrix* (or a contingency table) is commonly used as a metric for performance. It is a 2×2 matrix representing the dispositions of the set of input (testing set) when this set is applied to the classifier (such a matrix is shown in Figure 2.28).

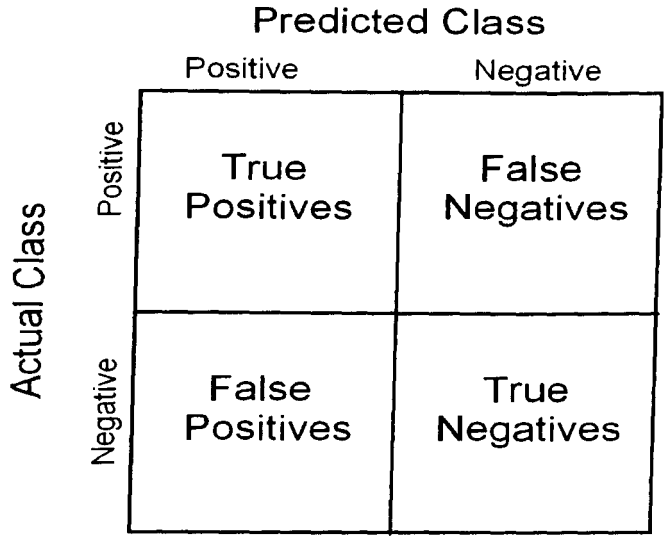

Figure 2.28: A confusion matrix suited for GPR classification

Below are some useful relations that can be used as measures for performance:

1. The true positive rate (also called hit rate or recall) of a classifier is given by:

$$T_p \text{ Rate} = \frac{T_p}{T_p + F_n} \times 100\% \tag{2.36}$$

2. The false positive rate (also known as false alarm rate) of a classifier is given by:

$$F_p \text{ Rate} = \frac{F_p}{F_p + T_n} \times 100\% \tag{2.37}$$

3. The false negative rate (also known as false dismissal rate) of a classifier is given by:

$$F_n \text{ Rate} = \frac{F_n}{T_p + F_n} \times 100\% \tag{2.38}$$

4. Accuracy is given by:

$$\text{Accuracy Rate} = \frac{T_p + T_n}{T_p + T_n + F_p + F_n} \times 100\% \tag{2.39}$$

5. Error rate is given by:

$$\text{Error Rate} = 100 - \text{Accuracy} \tag{2.40}$$

6. Precision is given by:

$$\text{Precision} = \frac{T_p}{T_p + F_p} \times 100\% \tag{2.41}$$

7. Score is given by:

$$\text{Score} = \text{Precision} \times T_p \text{ Rate} \tag{2.42}$$

Furthermore, it can be understood that

$$T_p \text{ Rate} + F_n \text{ Rate} = 100\% \tag{2.43}$$

$$F_p \text{ Rate} + T_n \text{ Rate} = 100\% \tag{2.44}$$

With the diversity range of segmentation techniques, it is essential to provide an adequate quantitative measure to present an effective comparison. A bach testing

for `Area 3` of the controlled test site [49] was performed. Only four techniques were chosen for this test: *A-scans statistics*, *B-scans statistics*, *regional features*, and the *double-stage classifier*. As near-real time performance is an essential objective in this study, the reason behind this choice was mainly the low computational time that the chosen methods require when compared to others (as shown in Table 2.4). The trained and calibrated neural classifier is applied to the features derived from the radargrams using these four techniques, outlining regions of interest corresponding to specific localised targets, in this case buried utility pipes. The aim of the testing process is to assess the performance of the on real data and extract the associated measures. The performance assessment was based on comparison with human operator interpretation and available ground truth data. There were 56 targets identified within the 32 radargrams. The results were compared based on some of the quantification measures described above in addition to time-cost, as illustrated shown in Table 2.5.

It can be seen that all of the four techniques have successfully identified all of the 56 targets, with a noticeably low false alarm rate for all of them. The main difference that can be noticed between these techniques is in the time cost. It can be seen that while it took the A-scan statistics classifier about three and a half hours to complete the classification, this time was reduced to about 15 minutes for the B-scan classifier, and to about 7 minutes for the new regional-features classifier. The relatively low precision rates are due to the fact that the total of *true positives* is compared to only the total of *false positives* and not all the positives and negatives. It can be seen as well how the precision rate has increased when the double stage classifier was used indication the efficiency of this classifier in reducing the *false positive* rate.

Furthermore, the most important feature of the regional-features classifier is its ability to detect hyperbolic regions without the need for edge detection techniques as

Table 2.5: Quantitative comparison between the performances of different segmentation techniques

Method	**True Positive Rate (%)**	**False Positive Rate (%)**	**Accuracy (%)**	**Precision (%)**	**Total Time (mins)**
Regional Features	100	0.7915	99.21	41.01	6.57
A-scans statistics	100	0.0604	99.94	26.62	196.2
B-scans statistics	100	0.5070	99.50	37.32	14.49
Double stage classifier	100	0.090	99.91	66.91	21.46

the rest of techniques do. This feature makes it much easier to further process the detected hyperbolae and extract interpretation information from them.

The *double-stage classifier* is a hybrid combination of the *regional-features* technique and the *B-scans statistics* technique. Although this technique has a higher time consumption compared to each one alone (about 22 minutes), but this additional time would be acceptable when high accuracy is sought. Moreover, it was successful in further reducing falsely detected regions.

2.7 Conclusions

This chapter has addressed the task of automatic segmentation of GPR radargrams, as a necessary step in the automatic processing and interpretation of such data for situations where near real-time interpretation of large volumes of data is crucial. A number of segmentation techniques were investigated and compared based on their efficiency and classification accuracy. These included techniques based on time-series discrimination and B-scan pattern recognition.

Spatial features have proven to be better suited to high speed segmentation of image data, particularly where medium variability is an issue. The use of simple statistical descriptors was particularly successful in differentiating between targets and non-targets in terms of speed, accuracy, and consistency. While this is true for data exhibiting two main visual categories, it would not suite segmenting demands when that data has greater variability and where targets 'zones' may have more subtle properties. In this case, higher order statistics would better suite this purpose, but again at the expense of an increased computational cost. The region features technique in particular represents a big improvement to the automatic segmentation

of GPR data specially where hyperbolic-shaped signatures are sought. Its ability to rapidly detect hyperbolic regions has reduced the extra time required by other techniques for detecting hyperbolic edges. This added speed, combined with the extra flexibility, robustness, accuracy and noise-immunity gives this technique considerable advantages over existing techniques for cylindrical target detection.

It was shown in this chapter that it is not necessary to use complicated combinations of features for detection purposes, where simple time-series and spatial features have shown high efficiency in distinguishing between target and non-target signatures.

The progressive data reduction approach has had a considerable effect on the overall computation time, allowing the automated system to operate in near real-time and making it adequate for on-site survey. A Comparison between the selected techniques in terms of detection capability and time consumption is presented in this chapter as well.

Chapter 3

Modelling Targets and Parameters Estimation

The task of describing the hyperbolic reflections resulting from buried cylindrical objects is addressed here, and a novel general equation that models such reflections is presented. The model takes into consideration the effect of the radius, depth, azimuth orientation, and vertical inclination of buried cylinders in addition to the dielectric constant of the host medium.

Furthermore, a developed hyperbola-specific fitting technique is discussed, which has the ability of calculating some target parameters when combined with the presented model.

3.1 Introduction

An important stage towards automating the interpretation of GPR data involves processing the detected and segmented data in a manner that results in as much information as possible about the segmented data, and hence the target. To a large

extent, reliance on human intervention and broad assumptions are the most outstanding shortcomings that have not been satisfactory resolved.

Recent research (e.g. [12] and [27]) has addressed some of these problems and has been successful to some extent at addressing and automating the interpretation process, and introducing a degree of robustness and consistency in the estimation of the dielectric properties of the host medium, but still falls short of removing or even minimising the uncertainty associated with the interpretation results. This uncertainty is mainly due to the fact that visually indistinguishable radar signatures can often result from subsurface configurations that are very different. This known problem is invariably overcome by making broad assumptions about the nature and geometry of the targets, the radar system and the medium. These assumptions are often made out of convenience rather than being informed by *a priori* knowledge, and hence their validity is at best questionable.

The class of targets under consideration in this chapter consists of cylindrical reflective objects such as pipes, tanks, and cables. Conventional processing and interpretation of the signatures of such objects relies on five underlying assumptions:

- that the dielectric constant in the volume above the object is homogenous and uniform [25],
- that the antenna radiation is two dimensional, i.e. out-of-plane effects are ignored [12],
- that the buried cylinder is normal to the plane containing this 2D radiation pattern [10],
- that the buried cylinder is parallel to the ground surface [10], and

- that the buried cylinder has negligible radius [14].

While the first two assumptions can be defended in most cases, the latter three are very rarely valid; indeed it is the accurate location and orientation of these cylinders that is the desired result of the interpretation. This has been one of the main obstacles preventing mainstream automation of GPR data processing in situations where accuracy is paramount, and it is this obstacle that is addressed in this chapter in a novel manner.

The hyperbolic signatures of cylinders detected by GPR are influenced by a number of parameters, some of which are environmental such as the dielectric properties of the medium, and some are system-related such as the antenna radiation pattern and polarisation, while other parameters are target-dependent such as the depth, radius, and orientation of the target relative to the scan path. Unreliable or incorrect information about these parameters, be it due to invalid assumptions or due to misinformation, would lead to inaccurate interpretations with possibly serious consequences when excavation or construction work is involved.

This chapter demonstrates how these inaccuracies are to a large extent avoidable, by presenting an outline of a procedure whereby these issues can be taken into account in the underlying geometrical model, attempting to iteratively estimate the parameters related to buried cylinders either directly or indirectly, thereby improving the accuracy of the interpretation of the radar returns. The effect of ignoring these parameters is also addressed and quantified.

3.2 Standard Signature Model

The poor directivity of ground-penetrating radar antennas has the effect of spatially smearing the resulting image, leading to the formation of downward-opening hyperbolic shapes in the radargram. GPR operators have long been familiar with these hyperbolic signatures associated with localised and extended reflecting targets, but it is only recently that the relationship between the shapes of these hyperbolae and the underlying geometric configuration has been investigated. Rather than being treated as a nuisance or a necessary evil associated with this geophysical technique, it is becoming apparent that studying the characteristics of these hyperbolae can provide valuable information about the exact nature of the targets in question. It is generally accepted [12] that the detected two-way travel time t is related to the horizontal position x, and the velocity of propagation of the electromagnetic waves v as follows

$$\left(\frac{t}{t_0}\right)^2 - \left(\frac{x - x_0}{\frac{v}{2}t_0}\right)^2 = 1 \tag{3.1}$$

where (x_0, t_0) are the coordinates of the apex of the hyperbola in the image (space-time) plane. The assumed configuration is one of an infinitely long cylinder buried in a homogenous medium, in a plane perpendicular to the linear direction of movement of a co-located bistatic antenna pair.

This is similar to the equation of a generalised vertically-opening hyperbola pair centred at point (x_0, y_0), and represented by

$$\left(\frac{y - y_0}{a}\right)^2 - \left(\frac{x - x_0}{b}\right)^2 = 1 \tag{3.2}$$

When Equations 3.1 and 3.2 are compared, then values of a, and b are given by

$$a = t_0 \tag{3.3}$$

$$b = \frac{v}{2} t_0 \tag{3.4}$$

Stolte and Nick [26] investigated the relationship between cylinder radius and hyperbola eccentricity for the purpose of migration, and later Olhoeft [27] attempted to derive radius information from the curvature of the hyperbola apex.

In this chapter, the problem of making broad assumptions is overcome, when it is shown that Equation 3.1 can be modified to incorporate the radius, depth, horizontal orientation, and vertical orientation of buried cylinders as well as the relative permittivity of the medium.

3.2.1 Effect of Cylinder Radius

The hyperbola model presented by [12] for example, relates the two-way travel time t to the horizontal position x and the velocity of propagation v as it was shown in Equation 3.1 above. This model relies on the assumption that the hyperbolic signatures result from point reflectors, and hence the radius is assumed to be zero. This is clearly a special case with a limited benefit, as in most of the cases the targets of interest are cylindrical objects with finite radii such as pipes and tanks, and using this model to characterise the signatures of such targets leads to erroneous information, as will be shown.

This problem would be solved if a more generalised equation is presented, that takes into account the possibility of a finite radius R. Figure 3.1 shows a generated

hyperbola due to change in position of the GPR and the possibility of that hyperbola being the result of a cylindrical object of radius R. It can be seen that

$$(z+R)^2 = (z_0+R)^2 + (x-x_0)^2 \tag{3.5}$$

where z_0 is the depth to the top of the cylinder, z is the apparent depth of the reflection from the cylinder at a position x displaced from the position of the cylinder x_0, and R is the radius of cylinder.

Substituting z with $\frac{vt}{2}$ and z_0 with $\frac{vt_0}{2}$ in Equation 3.5 and manipulating it gives

$$\left(\frac{t+\frac{2R}{v}}{t_0+\frac{2R}{v}}\right)^2 - \left(\frac{x-x_0}{\frac{v}{2}t_0+R}\right)^2 = 1 \tag{3.6}$$

This is similar to the equation of a generalised vertically-opening hyperbola pair of Equation 3.2 and with an eccentricity[1] of $\sqrt{1+\frac{b^2}{a^2}}$, as illustrated in Figure 3.2 and mathematically as in Equation 3.1. Equation 3.6 is thus an equation of a hyperbola centred around $(x_0, -\frac{2R}{v})$. It can also be seen that if the radius was zero (i.e. a point reflector) then Equation 3.6 becomes the same as Equation 3.1.

Figure 3.3 shows the effect of changing the radius on the shape of the resulting hyperbolae. It can be seen that when R is estimated to be zero, then this would lead the assumption that the spread of the hyperbola is caused by a higher value of the velocity of propagation v. Consequently, incorrect calculations of both the depth of the object and the dielectric constant of the medium will result.

By comparing this with Equation 3.6, then values of a, and b are given by

[1] The eccentricity of a hyperbola is the ratio between the focal length and the distance from the apex to the origin.

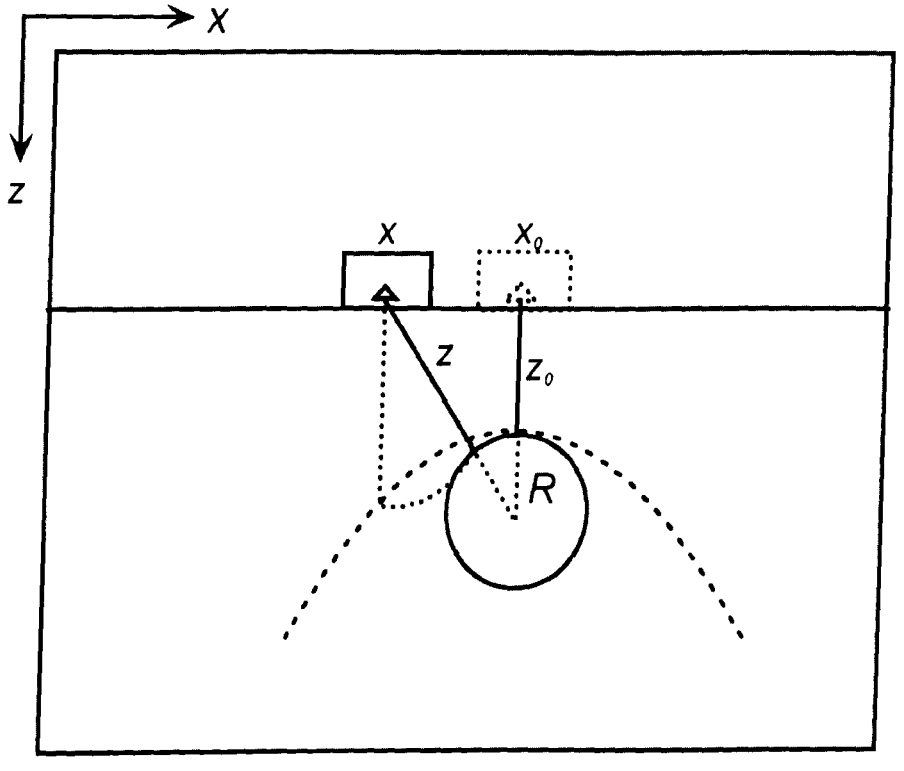

Figure 3.1: Effect of changing the value of R on the resulting hyperbola

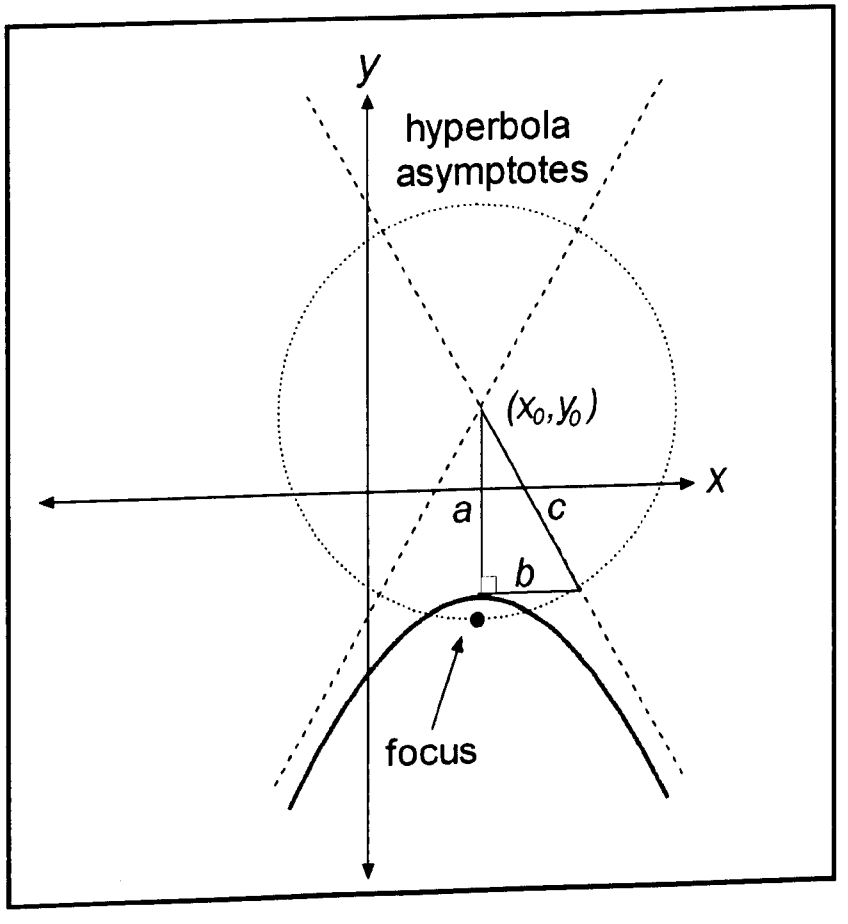

Figure 3.2: A general hyperbola with its asymptotes and related parameters

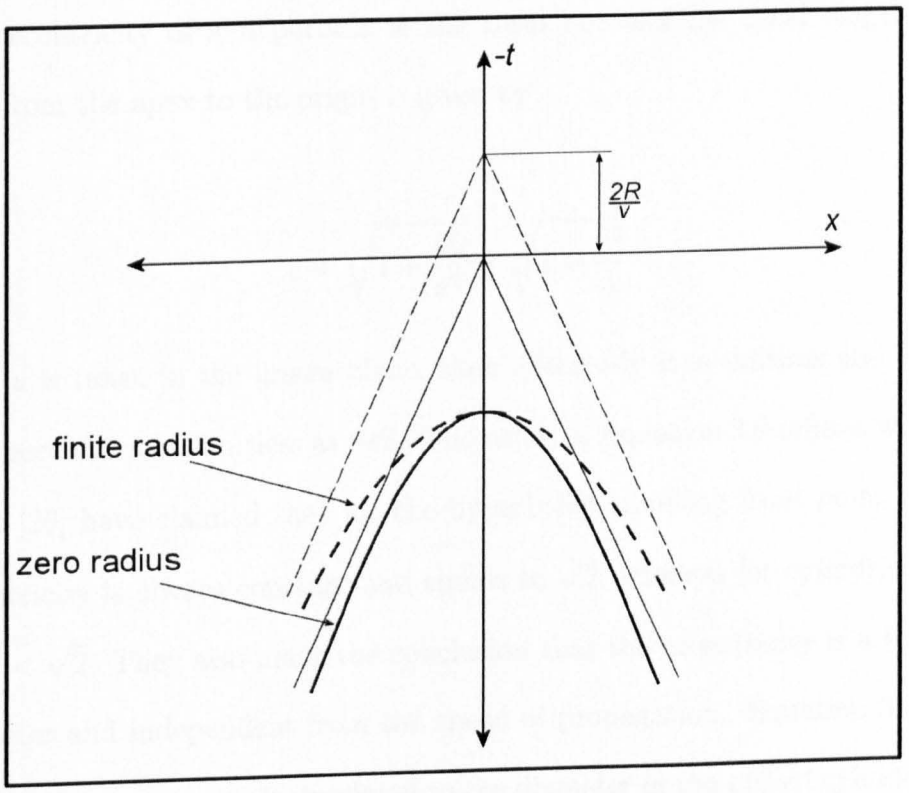

Figure 3.3: Effect of changing the radius of a buried cylinder on the resulting hyperbolae and corresponding asymptotes

$$a = t_0 + \frac{2R}{v} \tag{3.7}$$

$$b = \frac{v}{2}t_0 + R \tag{3.8}$$

The eccentricity of a hyperbola is the ratio between the focal length and the distance from the apex to the origin is given by

$$e = \sqrt{1 + \frac{b^2}{a^2}} = \sqrt{1 + \frac{v^2}{4}} \tag{3.9}$$

Since v is taken in the image plane, then effectively it is unitless and hence the resulting eccentricity is unitless as well. The result of Equation 3.9 refutes what Stolte and Nick [26] have claimed that for the hyperbolae resulting from point reflectors, the eccentricity is always constant and equals to $\sqrt{2}$, whereas for cylindrical-shaped objects $e < \sqrt{2}$. They also make the conclusion that the eccentricity is a function of the diameter and independent from the speed of propagation. Equation 3.9 demonstrates that the eccentricity is unrelated to the diameter of the buried cylinder; rather it solely depends of the speed of propagation v and hence the dielectric constant of the medium.

The importance of knowing the value of the radius emanates from the fact it gives a more accurate realisation of the nature and location of the target. As can be seen from Equation 3.6 that when R is zero then the resulting hyperbola is centered around the point $(x_0, 0)$, whereas if R has a finite value then this point will be shifted in time by a value of $-\frac{2R}{v}$, as shown in Figure 3.3. It can be seen also that the asymptotes

of the hyperbola with a finite radius have been shifted by $-\frac{2R}{v}$ without a change in their inclination as the angle between the asymptotes is related to the velocity of propagation in the medium.

Figure 3.4 shows the effect of changing v on the resulting hyperbola. Unlike the case of changing R it can be seen that as the speed changes, the point around which the hyperbola is centered remains the same, while the inclination of the asymptotes changes.

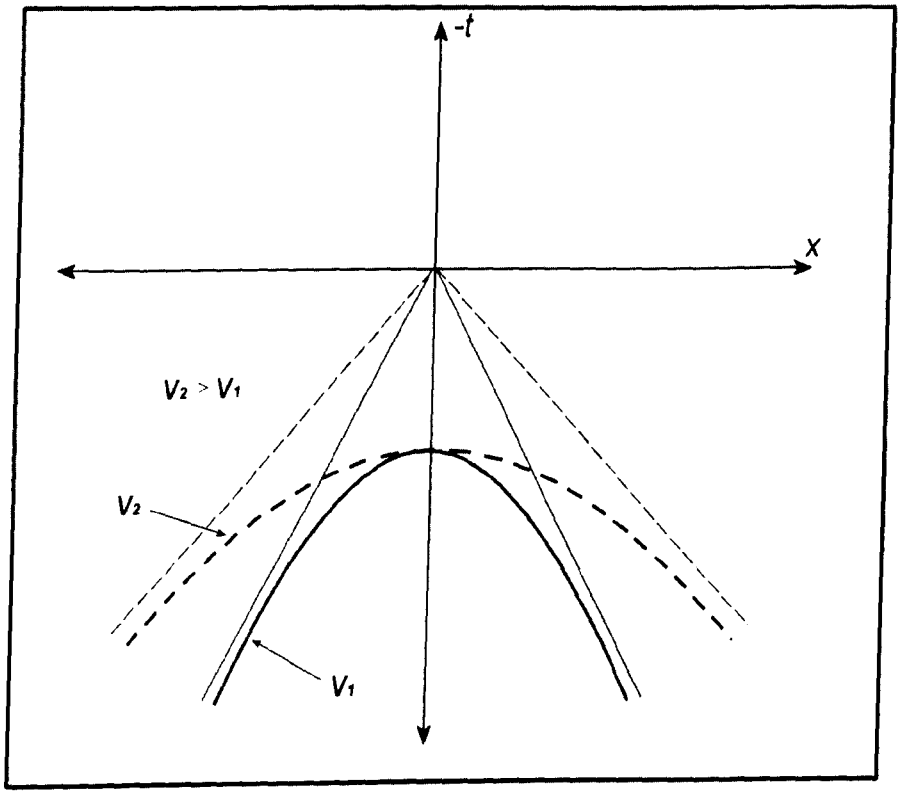

Figure 3.4: Effect of changing the speed of propagation on the resulting hyperbolae and corresponding asymptotes

Up to this date, the models that have been presented for hyperbolic signatures resulted from cylindrical objects are based on the assumption of zero radius. Consequently, any change in the shape of a hyperbola would be assumed to have arisen from a change in the dielectric constant of the medium which would, in turn, affect

the speed with which the radar signals penetrate through that medium.

Conventional polynomial fitters such as that presented in [28] which are normally used to fit hyperbolae resulting from buried cylinders, have two major shortcomings; they do not result in values for the parameters a and b, nor do take into account the effect of the radius R. Rather, they provide an inaccurate estimate of v when faced with a finite value of R.

Figure 3.5 shows the difference between a conventional polynomial fitter model and the novel conic-fitter-model combinations presented here. This difference is shown via the change in the inclination of the hyperbolae asymptotes. In the case of a conventional fitter, it would tend to artificially increase the speed of propagation v' (and hence the inclination of the corresponding asymptotes would increase as well) when there is a finite value for R, while the conic fitter would move the point where the two asymptotes intersect upwards by a value of $\frac{2R}{v}$. From Figure 3.5

$$\tan\omega = \frac{b'}{a'} = \frac{nb}{na - \frac{2R}{v}} \tag{3.10}$$

where n is a constant representing the ratio between the horizontal offset part where the asymptotes of the two models intersect and the depth of the target.

This exaggerated speed v' can be found from

$$v' = \frac{2b'}{a'} \tag{3.11}$$

and the percentage error in this estimate for the speed value is given by

$$e_v = \frac{v' - v}{v} \times 100\% = \frac{R}{nb - R} \times 100\% \tag{3.12}$$

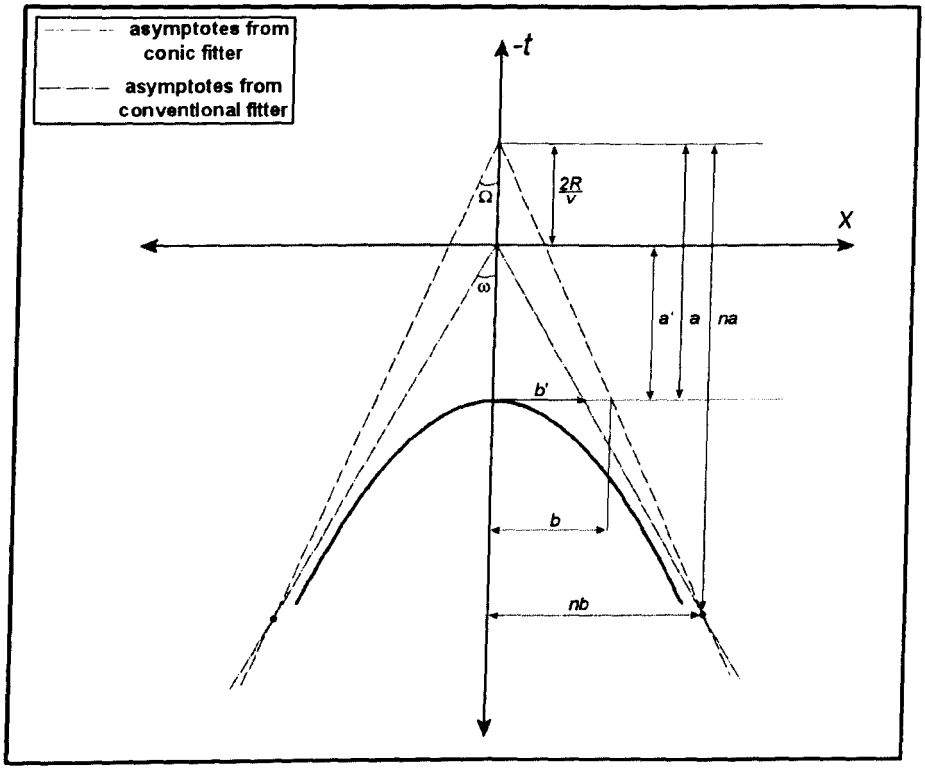

Figure 3.5: The difference between a conventional fitter and the conic-fitter when responding to a finite radius signature

As depth is proportional to speed, this is also the percentage error in depth estimate.

The value of n can be obtained from Figure 3.5 and is given by

$$n = \frac{\frac{R}{b}}{(\tan\Omega \tan\omega - 1)} \tag{3.13}$$

Figure 3.6 represents a plot of percentage depth error versus the radius-to-depth-to-centre ratio $\frac{R}{b}$ and was generated numerically by computing the 'best-fit' hyperbolae using a non-conic fitter and without taking R into account in the hyperbola model. It shows how error percentage increases sharply as the diameter of a buried cylinder goes higher, and even for modest $\frac{R}{b}$ ratios, the error can be very significant. The cylinders will thus be assumed to be at a depth *greater* than they are in reality, and this could cause disastrous consequences during excavation.

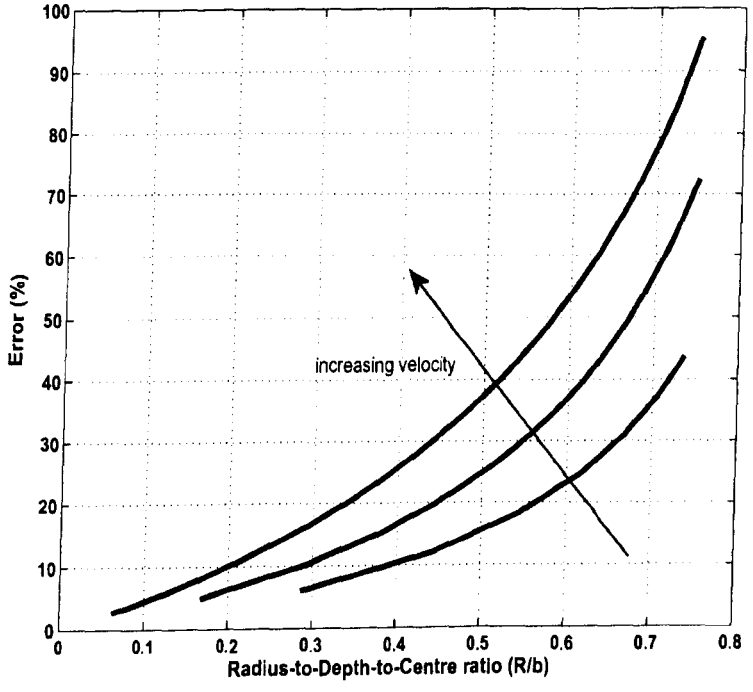

Figure 3.6: Percentage error in depth with respect to R/b ratio which result from conventional fitters

This error can be significant, even for relatively small radius-to-depth ratios, and can lead to disastrous consequences if digging or excavation is involved. It is possible to avoid this error simply by using the model in Equation 3.6 in conjunction with the presented least-square-hyperbola-fitter which capable of computing the parameters a and b, as opposed to just computing v as with conventional fitters [12]. However if the cylinder is not normal to the vertical plane directly beneath the radar scan line, this model will no longer hold and further errors will result.

3.2.2 Effect of Cylinder Orientation

The first direct reflection received by the GPR antenna from a smooth reflective cylinder of constant curvature will be that along a ray-path normal to the cylinder surface. The orientation of the cylinder relative to the radar scan direction will therefore influence the shape of the detected signature, and what follows is the first (published) attempt to quantify this relationship, in order to further refine the signature model given in Equation 3.6.

It is shown in Appendix C that the normal distance between the antenna and a cylinder oriented at an angle γ is reduced by a factor of $\sin\gamma$ compared to the normal case above. The signature will still be hyperbolic, but Equation 3.6 must now be modified as follows

$$\left(\frac{t+\frac{2R}{v}}{t_0+\frac{2R}{v}}\right)^2 - \left(\frac{(x-x_0)\sin\gamma}{\frac{v}{2}t_0+R}\right)^2 = 1 \tag{3.14}$$

The value of a will still the same, while the value of b will hence be modified by a factor $\frac{1}{\sin\gamma}$, which will in turn influence the eccentricity of the hyperbola and the inclination of its asymptotes. The values of a, and b are given by

$$a = t_0 + \frac{2R}{v} \tag{3.15}$$

$$b = \frac{\frac{v}{2}t_0 + R}{\sin\gamma} \tag{3.16}$$

It can be seen here that if only one value of R, v, or γ is known, the other two values can be accurately calculated. For example, if the dielectric constant of the host medium is known, and hence the value of v is known, then the value of R can then be calculated from

$$R = \frac{v}{2}(a - t_0) \tag{3.17}$$

or

$$R = b\sin\gamma - \frac{v}{2}t_0 \tag{3.18}$$

Then γ can be calculated from

$$\gamma = \arcsin\left(\frac{\frac{v}{2}t_0 + R}{b}\right) \tag{3.19}$$

As in the case of the finite radius above, ignoring this γ will result in an over-estimate of the interpreted value of the velocity, in turn resulting in an over-estimate of the depth to the top of the target. From Equation 3.19 above, then v is given by

$$v_\gamma = 2\frac{b\sin\gamma - R}{t_0} \tag{3.20}$$

Here, we use the term v_γ just to distinguish the value of v with the presence of γ from that when γ is not taken into account, which is

$$v = 2\frac{b - R}{t_0} \tag{3.21}$$

In order to show the effect of γ alone, then R is assumed to be zero in Equations 3.20 and 3.21. The percentage error in depth (or velocity) can then be calculated to be

$$\text{err} = \frac{v - v_\gamma}{v_\gamma} \tag{3.22}$$

hence

$$\text{err}_\gamma = \frac{1 - \sin\gamma}{\sin\gamma} \tag{3.23}$$

Figure 3.7 illustrates how this error rises dramatically with small values of γ. Again, this error can be avoided by incorporating $\sin\gamma$ into the hyperbolic signature model as in Equation 3.14.

Azimuthal and vertical orientations

It is convenient to think of the orientation of buried cylinders in terms of inclination angle and azimuthal orientation, rather than just the angle between the cylinder axis and the radar scan line. By decomposing γ into two such angles, further information about the geometry and configuration of the buried target can be derived.

The azimuth orientation is defined here as the acute angle between projection of the buried cylinder onto the ground (radar) plane and the direction of scanning of

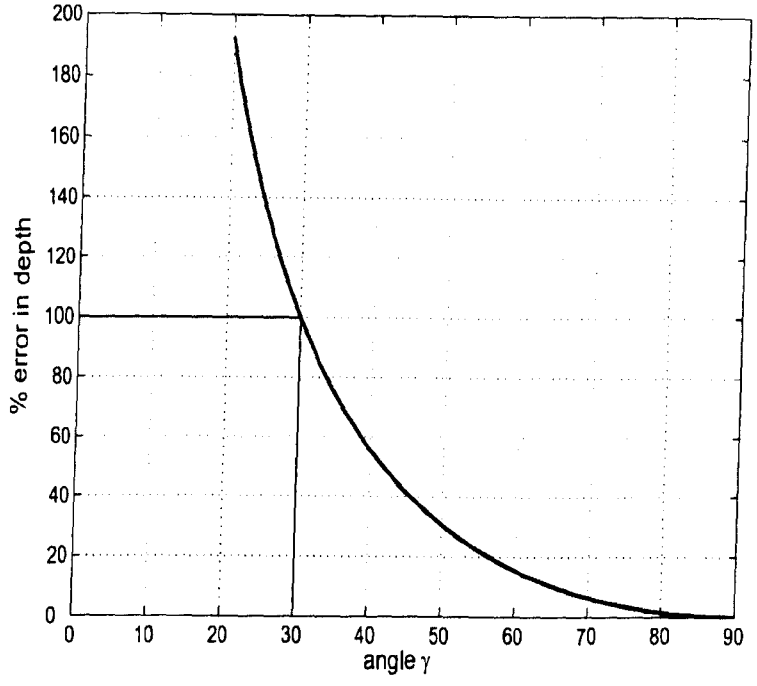

Figure 3.7: Effect of ignoring the angle γ on the interpreted depth

the GPR, and will be referred to here as α, whereas the inclination angle β is the acute angle between the cylinder and its projection onto the ground plane. Figure 3.8 shows two signatures taken over the same part of a pipe but with a changing α. It can be seen obviously how the shape of the hyperbola has changed in (b) from the one in (a). If the value of α is not known, then it will be assumed to be 90° and hence the flatness in the shape of the hyperbola would explained as being resulting from a higher velocity.

Looking at the data acquisition configuration from two different perspectives in Figures 3.9 and 3.10, one can appreciate that each of these angles has a separate and identifiable effect on the ray-path, and hence on the shape of the hyperbolic signature.

Referring to Figure 3.11, the relationship between the three angles can be derived. Assuming the radar scan direction to be along the $x-$axis, and assuming $z = 1$, the

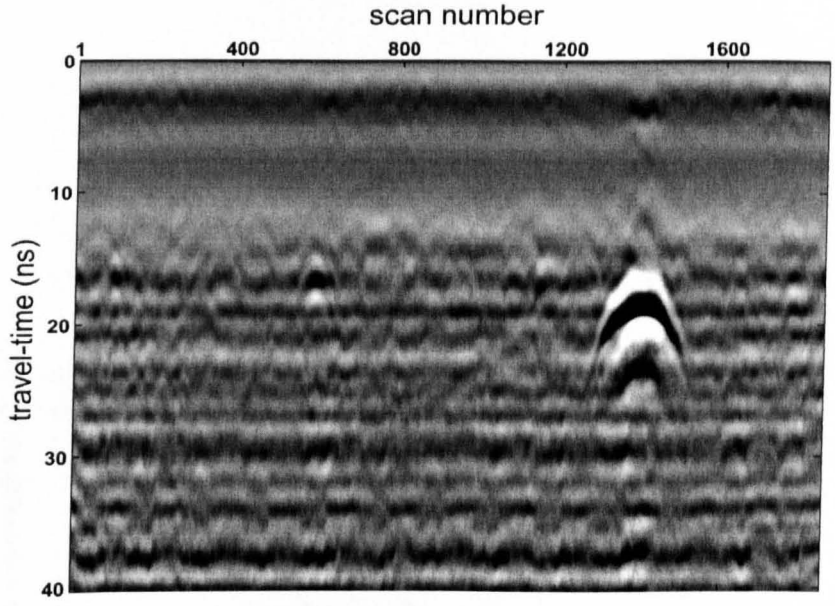

(a) Signature of a pipe with 90° horizontal orientation

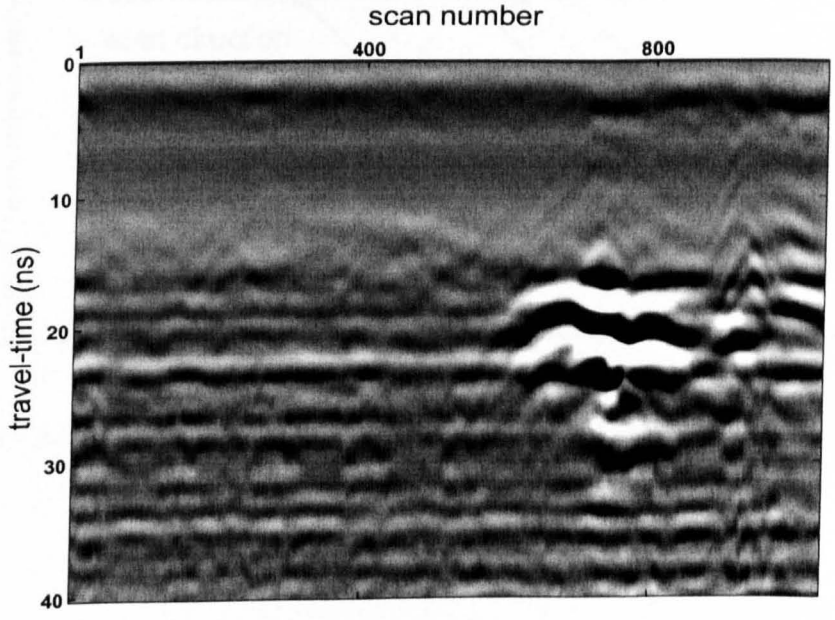

(b) Signature of the same pipe with $\approx 40°$ horizontal orientation

Figure 3.8: Effect of changing the azimuthal orientation of pipe on the corresponding signature

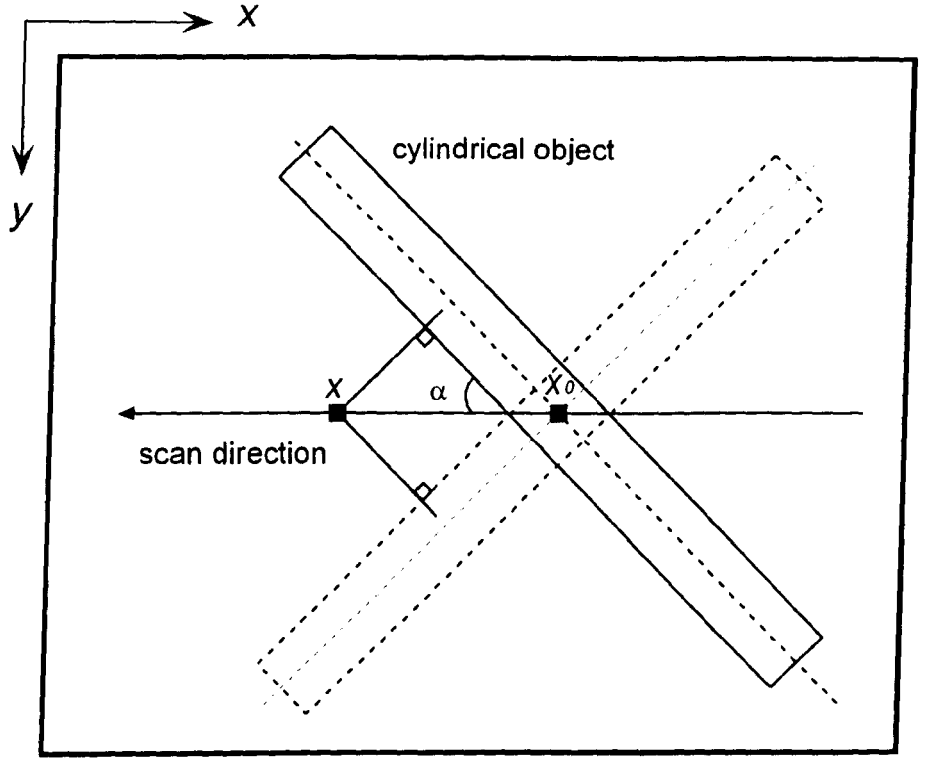

Figure 3.9: Effect of an arbitrary azimuthal orientation α on the ray-path

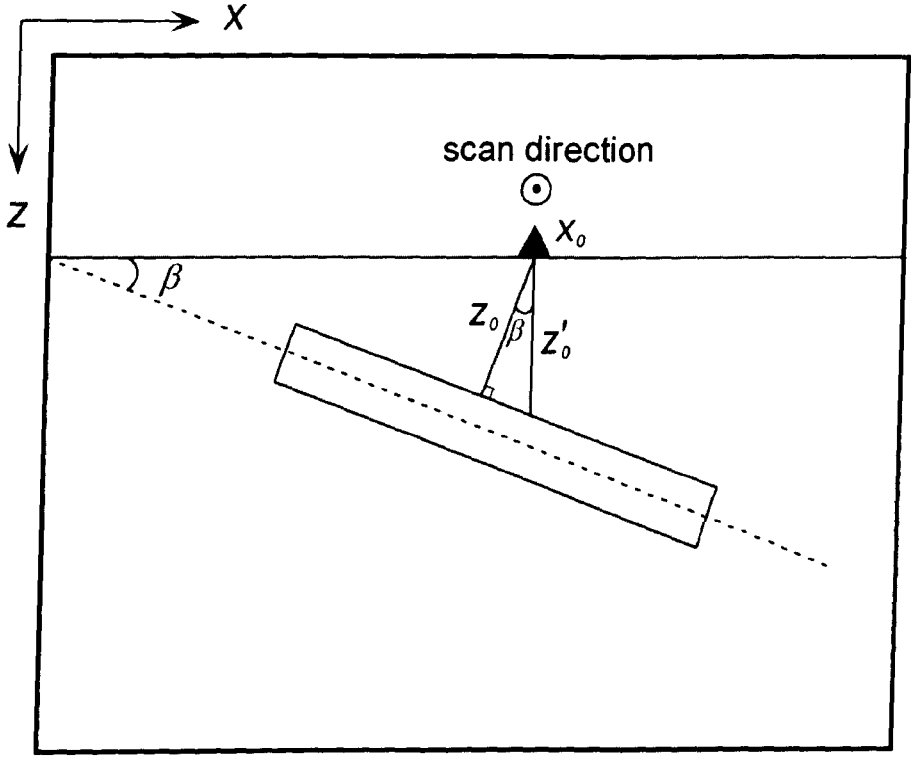

Figure 3.10: Effect of an arbitrary inclination angle β on the ray-path

length of the side h which is common to two triangles can be expressed as

$$h^2 = y^2 + 1 = \rho^2 + x^2 - 2\rho x \cos\gamma \tag{3.24}$$

where $x = \frac{\cos\alpha}{\tan\beta}$, $y = \frac{\sin\alpha}{\tan\beta}$, and $\rho = \frac{1}{\sin\beta}$.

Substituting in Equation 3.24 gives

$$\frac{\sin^2\alpha\cos^2\beta}{\sin^2\beta} + 1 - \frac{1}{\sin^2\beta} - \frac{\cos^\alpha\cos^2\beta}{\sin^2\beta} - 2\frac{1}{\sin\beta}x\cos\gamma = 0 \tag{3.25}$$

Manipulating the above leads to

$$\frac{\sin^2\alpha\cos^2\beta + \sin^2\beta - 1 - \cos^2\alpha\cos^2\beta + 2\cos\alpha\cos\beta\cos\gamma}{\sin^2\beta} = 0 \tag{3.26}$$

$$\sin^2\alpha\cos^2\beta + \sin^2\beta - 1 - \cos^2\alpha\cos^2\beta + 2\cos\alpha\cos\beta\cos\gamma = 0 \tag{3.27}$$

$$\sin^2\alpha\cos^2\beta - \cos^2\beta - \cos^2\alpha\cos^2\beta + 2\cos\alpha\cos\beta\cos\gamma = 0 \tag{3.28}$$

$$-\cos^2\beta(1 - \sin^2\alpha + \cos^2\alpha) + 2\cos\alpha\cos\beta\cos\gamma = 0 \tag{3.29}$$

$$-2\cos^2\beta\cos^2\alpha + 2\cos\alpha\cos\beta\cos\gamma = 0 \tag{3.30}$$

This will result in the following final compact relation

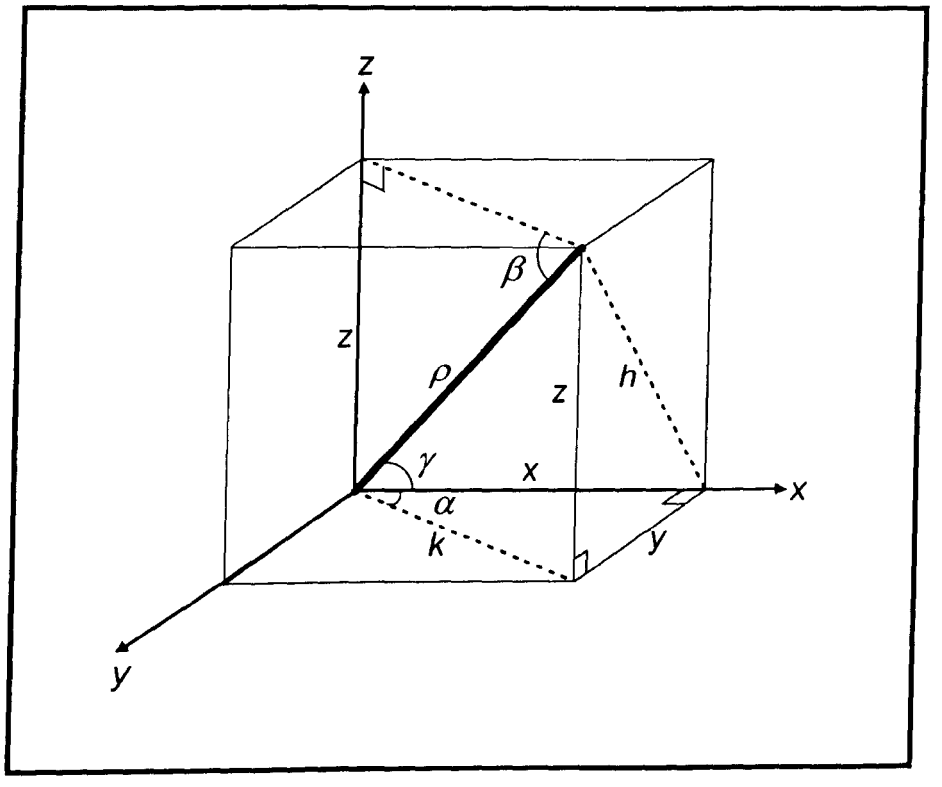

Figure 3.11: Geometric relationship between the angles α, β and γ

$$\cos\gamma = \cos\alpha\cos\beta \tag{3.31}$$

Figure 3.12 illustrates how γ varies with α and β, with the square box and the circle representing the limits of detectability. Thus Equation 3.14 can be modified to include both components α and β.

$$\left(\frac{t+\frac{2R}{v}}{t_0+\frac{2R}{v}}\right)^2 - \left(\frac{(x-x_0)\sqrt{1-\cos^2\alpha\cos^2\beta}}{\frac{v}{2}t_0+R}\right)^2 = 1 \tag{3.32}$$

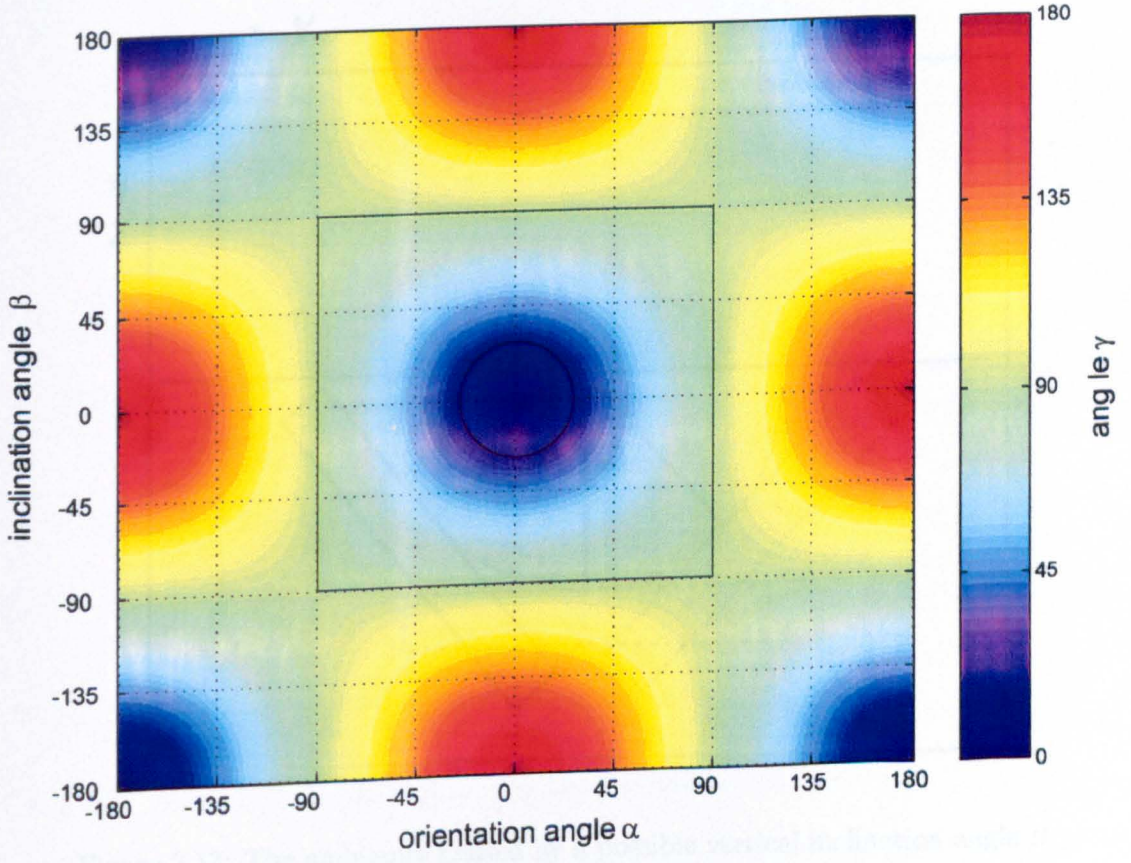

Figure 3.12: Graphical illustration of the numeric angles α, β and γ; the region of detectability is between the circle and the square

This demonstrates that the signature of a buried cylinder is unique to a single geometrical configuration consisting of a finite radius R, and angle γ, buried in a

medium of constant dielectric constant $\varepsilon_r = \left(\frac{c}{v}\right)^2$ where c is the speed of light in vacuum.

Figures 3.9 and 3.13 demonstrate that despite the above there is still some ambiguity in determining the exact geometry, as an orientation of α cannot be distinguished from $-\alpha$, neither can an inclination of β be distinguished from $-\beta$. This highlights the limits of what information can be derived from a single radargram, although it is envisaged that even this limitation could be overcome if the antenna radiation pattern was asymmetrical. Using multiple-radargrams and further data from across the site, this uncertainty can be removed, as will be discussed in Chapter 4.

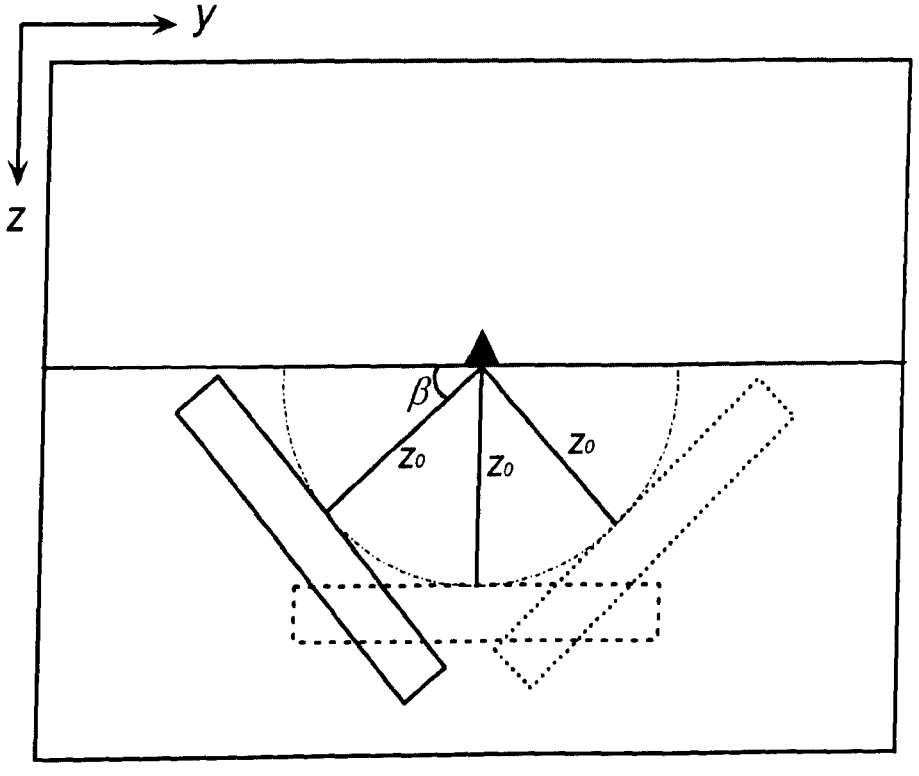

Figure 3.13: The ambiguity caused by a possible vertical inclination angle β

It was shown in Figure 3.7 how incorrectly assuming a configuration where the pipe is normal to the scan direction (i.e. $\gamma = 90^o$) leads to significant errors in

the estimation of the propagation velocity (and hence the target depth). Figure 3.14 illustrates how α and β each contribute to this error. Note how the error is asymptotic as both angles approach zero. It is also notable from Figures 3.7 and 3.14 that at an orientation or inclination of 30°, the resulting error in the depth will be 100%, i.e. the target will be 'seen' to be at twice the actual depth.

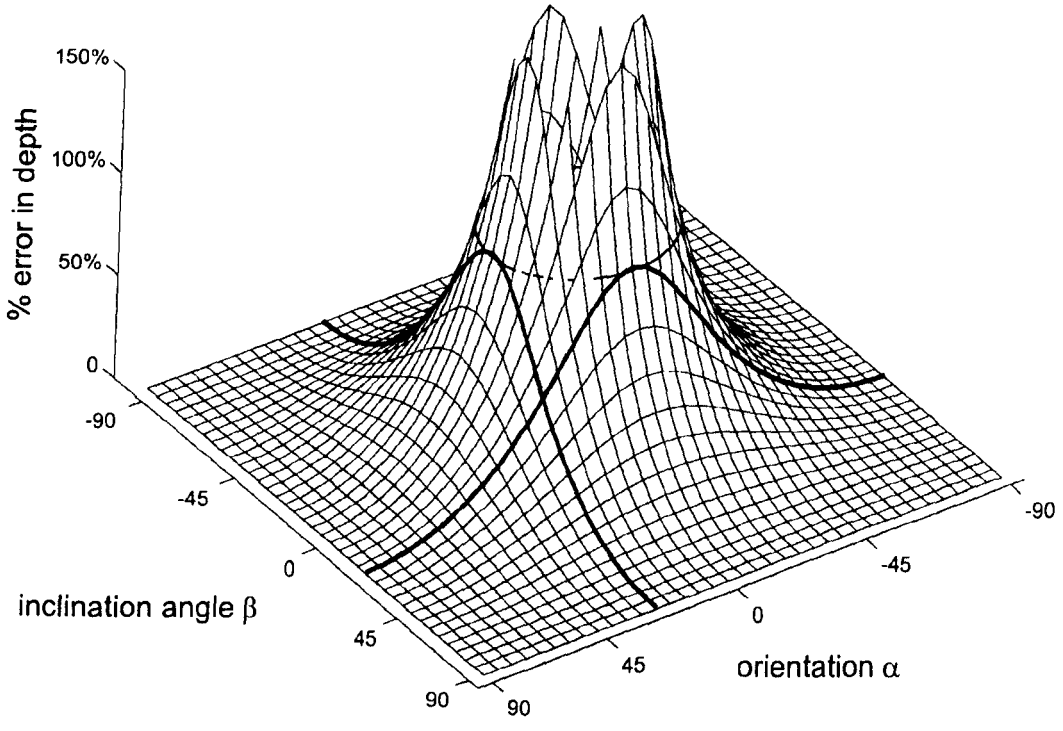

Figure 3.14: Effect of ignoring the angles α and/or β on the interpreted depth

3.2.3 Hyperbola fitting

Despite the variety of fitting procedures available, yet they are either Hough transform-based approaches which are computationally expensive, or least-square fitting methods to a general conic and rejecting non-hyperbolic fits. These latter methods are fast and of good performance when the given data belong to a hyperbolic-shaped arc, and they use iterative refinement procedures when the data are more

noisy [64], however this is achieved at the expense of computational cost. Moreover, the latter methods do not adequately characterise the hyperbolae in terms of a and b, and hence fall short of providing the necessary information for target identification.

The new fitting technique presented in this work was developed from Fitzgibbon's ellipse-specific direct least-square fitting technique [64]. It uses constrained least-square method for specifically fitting hyperbolae. The most important feature of the technique is its ability to calculate certain parameters of the fitted hyperbolae. These parameters are used to calculate target information and hence minimising the inaccuracy of weak estimations.

This fitter has the following advantages:

1. Hyperbola-specificity
2. Makes it possible to calculate depth, propagation speed, radius, vertical inclination, and azimuth orientation
3. High robustness in cases of non-ideal data, and
4. High computational efficiency

A general conic can be represented by an implicit second order polynomial

$$F(\mathbf{m};\mathbf{x}) = \mathbf{m}\cdot\mathbf{x} = a_c x^2 + b_c xy + c_c y^2 + d_c x + e_c y + f_c = 0 \qquad (3.33)$$

where $\mathbf{m} = [a_c\ b_c\ c_c\ d_c\ e_c\ f_c]^T$ and $\mathbf{x} = [x^2\ xy\ y^2\ x\ y\ 1]^T$. $F(\mathbf{m};\mathbf{x}_i)$ is called the *algebraic distance* of a point (x, y) to the conic $F(\mathbf{m};\mathbf{x}) = 0$. The fitting of such a general conic can be achieved via minimizing the sum of squared algebraic distances

$$D_A(\mathbf{m}) = \sum_{i=1}^{N} F(\mathbf{x}_i)^2 \tag{3.34}$$

of the curve to the N data points x_i [65]. The parameter vector $\mathbf{m}$ is required to be constrained in a manner that avoids solution of $\mathbf{m} = 0_6$, and recognises that any multiple solutions of $\mathbf{m}$ represents the same conic [64].

It was shown by Bookstein [66] that if a quadratic constraint is set on the parameters, then Equation 3.34 can be solved by the rank-deficient generalised eigenvalue system

$$\mathbf{D}^T\mathbf{D}\mathbf{m} = \mathbf{S}\mathbf{m} = \lambda\mathbf{C}\mathbf{m} \tag{3.35}$$

where $\mathbf{D} = [x_1 x_2 ... x_n]^T$ is called *design matrix*, $\mathbf{S} = \mathbf{D}^T\mathbf{D}$ is called *scatter matrix* and $\mathbf{C}$ is the matrix that expresses the constraint.

In order to fit a hyperbola specifically to produce a highly efficient solution of the linear least- squares problem of Equation 3.34, the parameter vector $\mathbf{m}$ is to be constrained so that the conic it represents is forced to be a hyperbola. This constraint happens to be the *discriminant* ${b_c}^2 - 4a_c c_c$.

It is very difficult to solve this constraint inequality problem in general as there is no guaranteed solution. In stead the parameters can be scaled arbitrarily via imposing the equality constraint ${b_c}^2 - 4a_c c_c = 1$.

This constraint may be expressed in the matrix of the form $\mathbf{m}^T C\mathbf{m} = 1$ as

$$\mathbf{m}^T \begin{pmatrix} 0 & 0 & -2 & 0 & 0 & 0 \\ 0 & 1 & 0 & 0 & 0 & 0 \\ -2 & 0 & 0 & 0 & 0 & 0 \\ 0 & 0 & 0 & 0 & 0 & 0 \\ 0 & 0 & 0 & 0 & 0 & 0 \\ 0 & 0 & 0 & 0 & 0 & 0 \end{pmatrix} \mathbf{m} = 1 \tag{3.36}$$

minimizing

$$E = \|\mathbf{Dm}\|^2 \tag{3.37}$$

subject to the constraint

$$\mathbf{m}^T\mathbf{Cm} = 1 \tag{3.38}$$

This system was solved by calculating the generalized eigenvectors of Equation 3.35 and thus the parameters of the hyperbolae are obtained.

Using this hyperbola-specific conic section least squares fitter, the values of a and b can be extracted, as the angle between the two asymptotes is $2\arctan\frac{b}{a}$. This angle, in conjunction with either the focal length or the distance from the centre to the apex, together uniquely characterise a hyperbola. From the two parameters a and b, the remaining parameters x_0, t_0, v and R can thus be computed, subject to the above assumptions, provided that either $\alpha = 90°$ and $\beta = 0°$, or both their values are known. When α and β are unknown, then the fitter would calclculate a and b based on the assumption that $\gamma = 90°$. The consequences of making such an assumption will be discussed in detail in Chapter 4.

3.3 Image scaling

In order for meaningful quantities to be extracted from the radargrams for real-life interpretation and mapping, then the units must be converted to physical dimensions. Knowledge of the radar parameters and data acquisition settings stored in the raw data file header (see Appendix D) facilitates this process of conversion. Using the header parameters scans_per_metre, samples_per_scan and range, the routes necessary for such unit conversions can be seen to be:

$$\text{scans} \longrightarrow \text{metres} \quad : \quad \text{scan} \times \frac{\text{metre}}{\text{scan}} \tag{3.39}$$

$$\text{samples} \longrightarrow \text{second} \quad : \quad \text{samples} \times \frac{\text{second}}{\text{sample}} \tag{3.40}$$

$$\text{samples} \times \frac{\text{scan}}{\text{sample}} \times \frac{\text{second}}{\text{scan}} \tag{3.41}$$

$$\frac{\text{scan}}{\text{sample}} \longrightarrow \frac{\text{metre}}{\text{second}} \quad : \quad \frac{\text{scan}}{\text{sample}} \times \frac{\text{metre}}{\text{scan}} \times \frac{\text{sample}}{\text{second}} \tag{3.42}$$

$$\frac{\text{scan}}{\text{sample}} \times \frac{\text{metre}}{\text{scan}} \times \frac{\text{sample}}{\text{scan}} \times \frac{\text{sample}}{\text{second}} \tag{3.43}$$

and so by defining unit conversion constants

$$\xi_x = \frac{1}{\texttt{scans\_per\_metre}} \tag{3.44}$$

$$\xi_t = \frac{\texttt{range}}{\texttt{samples\_per\_scan}} \tag{3.45}$$

and

$$\xi_v = \frac{\texttt{samples\_per\_scan}}{\texttt{scans\_per\_metre} \times \texttt{range}} \tag{3.46}$$

where v_s is the velocity of propagation of GPR electromagnetic waves. The quantities x_0, t_0 and v_s can be converted to physical SI dimensions using

$$\hat{x} = \xi_x \, x_0 \tag{3.47}$$

$$\hat{t} = \xi_t \, t_0 \tag{3.48}$$

$$\hat{v}_s = \xi_v \, v \tag{3.49}$$

The velocity of propagation is primarily governed by the relative permittivity of the propagation medium. Assuming the magnetic permeability to be equal to that of free space, the dielectric constant, or relative permittivity of the soil ϵ_s can then be calculated directly from the velocity $\hat{v}_s$

$$\epsilon_r = \left(\frac{c}{\hat{v}_s} \right)^2 \tag{3.50}$$

where c is the speed of electromagnetic propagation in free space.

The medium through which the radiation propagates is not expected to contain materials with relative permittivities outside the range 2 to 40 (see Appendix E). Nevertheless, as there exists the possibility of performing radar surveys above targets immersed in water, the upper limit is set at 81, the permittivity of salt water. Using Equations 3.46 and 3.50, the lower and upper limits for v_s can be shown to be

$$\frac{c}{\xi_v \sqrt{\epsilon_{r_{min}}}} \leq v \leq \frac{c}{\xi_v \sqrt{\epsilon_{r_{max}}}} \tag{3.51}$$

where $\epsilon_{r_{min}} = 2$ and $\epsilon_{r_{max}} = 81$.

The vertical axis is then re-scaled to represent depth information instead of travel-time by multiplying the turnaround time by $\hat{v}_s/2$.

3.4 Radius Calculation

In order to make it possible to extract information from the hyperbolic signatures detected in GPR radargrams, both the hyperbola model in Equation 3.6 and the least-square-fitting technique are combined. The resulting technique represents the stage that follows the detection and segmentation stage.

As the regional-features technique (described in Chapter 2) is used for detecting and segmenting hyperbolic signatures prior to hyperbola-fitting and targets information extraction, since it has proven to be the best technique for hyperbolic signatures detection.

Here, file 31 obtained from Area 3 in the controlled test site [49], is used as a sample file. This file is shown in Figure 3.15 and it contains two hyperbolic signatures resulted from two pipes buried at 70 centimeters depths.

The range of 40 ns in this example now becomes 2.4 m. This re-scaling converts the radargram into a spatial image which can be subjected to GPR time domain processing.

Figure 3.16 shows the segmentation result and the identified hyperbolic signatures after applying the double-stage classification method. It is to be mentioned here that if there are vertically adjacent hyperbolae then if the difference in depth between each two hyperbola is less than 1.5λ then the second hyperbola is not considered another cylinder, but it is still used to improve the accuracy of the top cylinder. Each one of the two hyperbolic regions was subjected to region-completion and skeletonisation processes to extract the related sets of points (as shown in Figure 3.17), then the fitting-technique was applied to each one of these sets. Fitting results can be seen in Table 3.1 and Figure 3.18. It can be seen that the relative permittivity is calculated

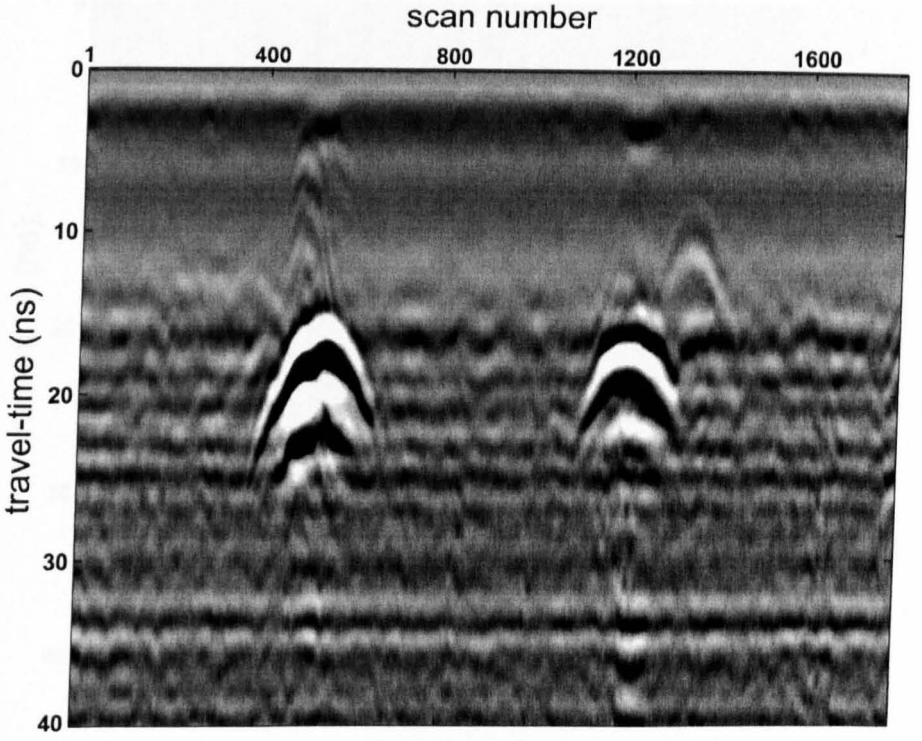

Figure 3.15: Typical ground-penetrating radar image exhibiting two hyperbolic regions

to be 11.9 which is typical for damp clayey soil at the test site [2], and [49]. As for the radius and depth, it can be seen that they are calculated within low error percentages, while the radius calculated from a conventional fitter is almost 50% different from the original value. The "True value" in the table are obtained from the ground truth provided with the site maps [49].

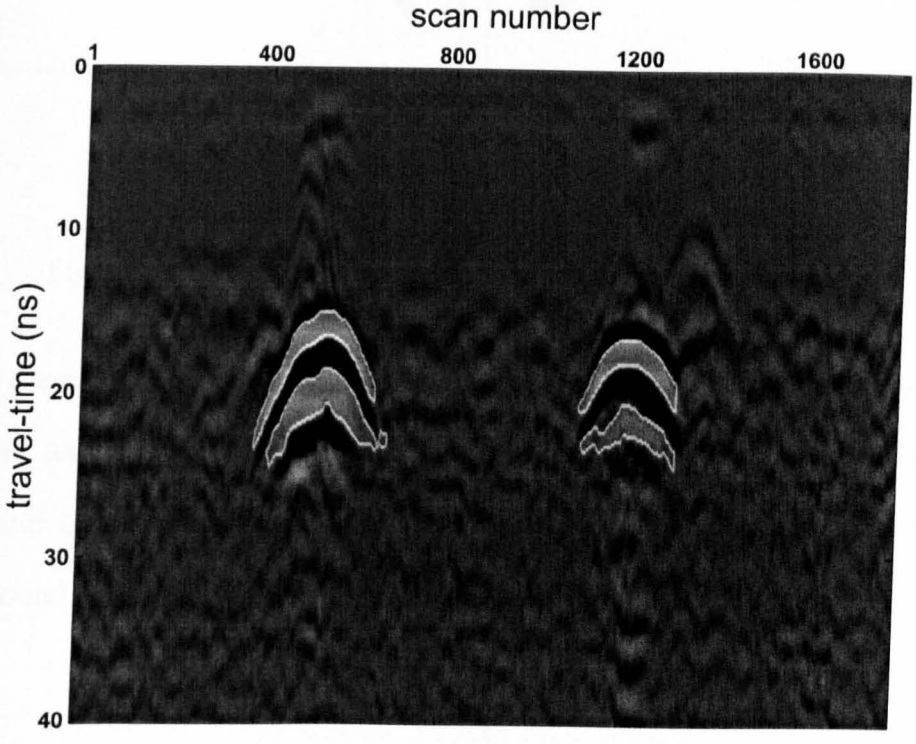

Figure 3.16: Classification result using the double-stage classifier

Table 3.1: Pipe parameters resulted from fitting

Parameters	**depth1 (cm)**	**depth2 (cm)**	R_1 **(cm)**	R_2 **(cm)**	**depth (cm)** $(R = 0)$	ϵ_{r1}	ϵ_{r2}
True Values	70	70	5	5	70	unknown	unknown
Calculated Value	72.3	65.55	5.56	5.64	101.98	11.9	11.9
Error (%)	3.29	6.36	11.2	12.8	45.69	–	–

In both examples, the fitter returns values for a, b, and t_0. From these values, both

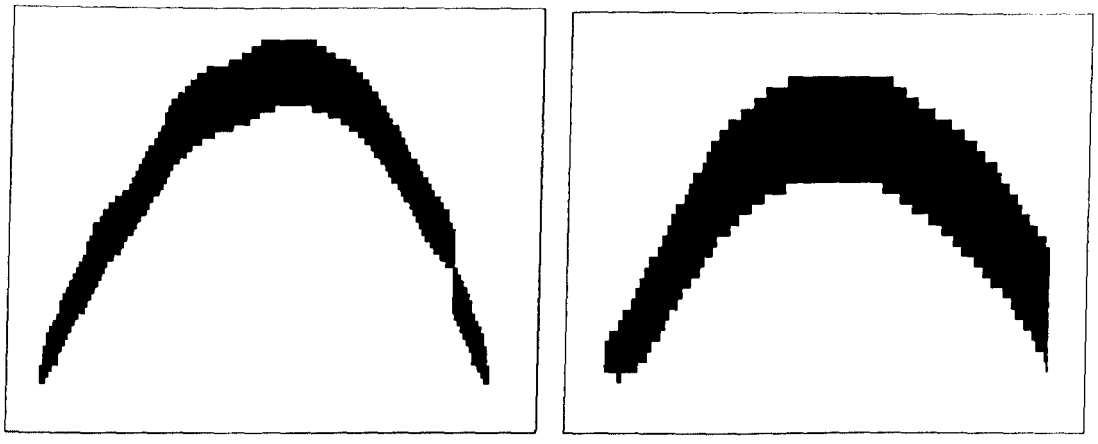

(a) Region 1 (b) Region 2

Figure 3.17: Detected hyperbolae after region-completion process

R, and v are calculated as in Equations 3.7 and 3.8. By using the GPR-scan header parameters, namely `range`, `scans_per_meter`, and `samples_per_scan`, then the values of R, v, and t_0 are converted to physical dimensions as shown in Section 3.3. The depth is found from

$$d = \frac{\hat{v}_s \hat{t}}{2} \tag{3.52}$$

It can be seen from the obtained results that the differences in error between the new model and the conventional model (where R is assumed zero) is a clear indication in favor of this new technique. When applying the new technique to synthetic data, however, the error is negligible as one would expect.

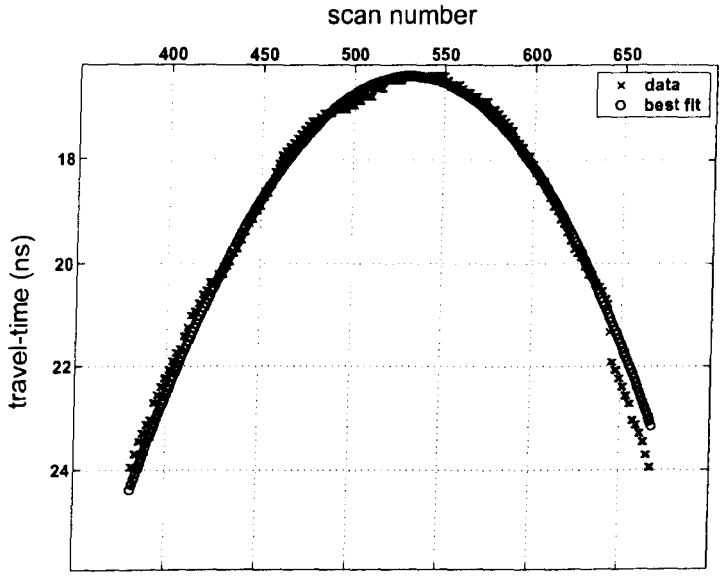

(a) Fitting result for points of region 1

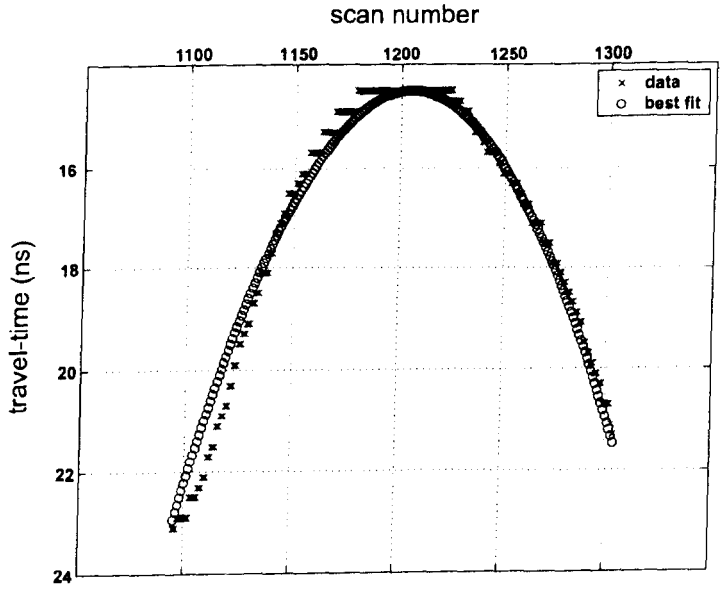

(b) Fitting result for points of region 2

Figure 3.18: Fitting results for the extracted hyperbola-points

3.5 Conclusions

This chapter has attempted to refine the 'art' of interpreting radargrams originating from buried cylindrical reflectors, by presenting a mathematical model that incorporates not only the depth, velocity and radius information, but also the inclination and azimuthal orientation of the cylinder in question. The dangers of ignoring these parameters in the resulting interpretation have been quantified and illustrated with respect to each of these parameters.

By combining information extracted from various cues from within the data in a manner that minimises the reliance on ready-made assumptions, rules of thumb and conjecture, it is possible to improve the reliability and accuracy of the final interpretation result. These procedures are to be used to develop guidelines and recommendations for GPR data acquisition and interpretation.

The overall quantification of speed for the processing stages including detection, segmentation, edge-processing, and characterisation, has shown a high performance speed which serves the aim of an adequate and reliable near-real time system.

Chapter 4

Site Data Processing

This chapter presents a novel iterative parameter-correction method which combines the individual target information derived from the hyperbolic signatures to detect the orientation and and inclination of extended cylinders and correct their geometrical parameters derived from the individual radargrams.

4.1 Data Fusion for 3D Pipe Detection

In Chapters 2 and 3 the stages of target-detection, segmentation, and characterisation where discussed. Figure 4.1 shows these stages which are curried out automatically and in near real-time. In an ideal case, when *a priori* knowledge about both vertical and azimuthal orientations of the buried targets exists, then these stages are quite adequate for accurate target detection and characterisation.

Despite the amount of information that can be derived from a single radargram, this information is nevertheless limited in most cases, and without additional knowledge about the site or the buried objects it will not be possible to uniquely locate a detected pipe or cylinder as it may be subject to either a vertical or azimuth orien-

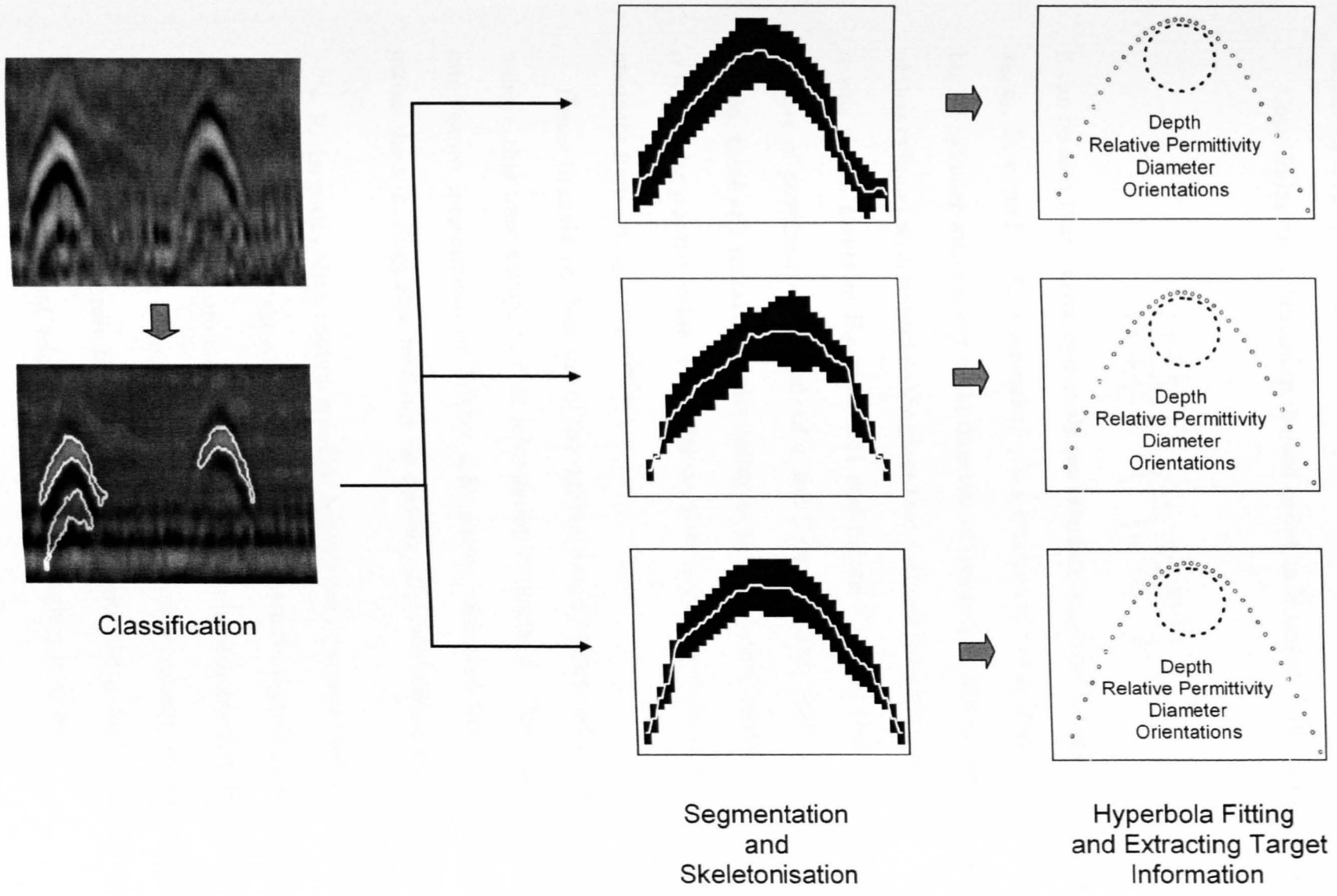

Figure 4.1: Detecting targets and extracting their related information

tation (or both), and this makes the procedure illustrated in Figure 4.1 incomplete.

Considering the relationship derived earlier in Equation 3.14, and repeated here,

$$\left(\frac{t+\frac{2R}{v}}{t_0+\frac{2R}{v}}\right)^2-\left(\frac{(x-x_0)\sin\gamma}{\frac{v}{2}t_0+R}\right)^2=1 \tag{4.1}$$

it can be seen that a given hyperbola can originate only from a single set of parameters x_0, t_0, R, v, and γ. As a reminder, γ is a function of the azimuthal orientation of a buried cylinder with respect to the direction of scanning α, and the vertical inclination of that cylinder with respect to the plane that contains the ground surface β. However it was shown earlier in Equation 3.31 and Figure 3.12 that there exists an infinite number of possible combinations of α and β for any given value of γ. Even if α was known, there still remain the uncertainty as to the relative orientation of the pipe as α is a scalar positive value. Furthermore, there is no way to determine both γ and v uniquely from a single hyperbola.

Hence to make the best use of the signature model presented in Chapter 3 and to remove this uncertainty, further information is required. This can either be site-intelligence information, or further information extracted from other radargrams across the site. Suggested methods for deriving this information are as follows:

- Radargrams often contain spurious hyperbolae from point reflectors, which will generally exhibit the correct velocity (and hence the correct permittivity). This can be detected automatically when multiple hyperbolae that are spatially not far apart exhibit a range of velocities; the lowest velocity should generally be accepted as accurate based on the fact (mentioned in Section 3.2.2) that the lower the apparent velocity, the closer the angle γ is to 90°.

- Occasionally site information is available to suggest that pipes or cylinders are buried parallel to the radar scan plane, or at a given inclination angle; manholes and other means are often available to verify this information. This can exclude β from the model, leaving us with a direct relationship (from Equation 3.31 between γ and α.

- Provided the radar scan lines are sufficiently close together, pipes can generally be tracked between adjacent radargrams. This will provide a fairly accurate estimate for α; in conjunction with the above, this information may be sufficient to uniquely identify the parameters of the target.

- 3D line detection algorithms such as the Adaptive Non-accumulative Hough Transform (ANHT) presented in [15] may be used to estimate α and β simultaneously from the available information about the hyperbola apices.

- If a reliable estimate of the dielectric constant of the upper layer of the medium is known, then γ can be calculated and hence the rest of target parameters can be identified.

All available information should be exploited in the interpretation of any given reflection, as a single hyperbola will rarely expose the reality of the situation, while there are often valuable cues within the data that are overlooked.

The procedure normally followed for interpreting is based on processing individual radargrams to extract information from detected hyperbolae, such as depth and relative permittivity, while the radius and the orientations of a target are considered negligible. It was shown in Chapter 3 the inaccuracy of such considerations. However, even when these parameters are considered the uncertainty problem with regard to

these parameters will still be standing.

When the value of the relative permittivity of the host medium is unknown, it is estimated in order to calculate other parameters. One way for doing this is by assuming the minimum calculated velocity of propagation within all radargrams to be that resulted from a point reflector, and consequently the relative permittivity will be calculated and considered to be the same for the whole site. A more accurate way may involve dividing the site into subareas and calculate the permittivity for each area in the same manner. This method may work if the relative permittivity for the investigated site is constant or subjected to slight changes, while when drastic changes are involved the results would be totally different from reality when targets are not detected (completely or partially) as it will be shown in the subsequent sections.

In this study, the automatic detection and interpretation system presented in Chapters 2 and 3, is completed by combining it with the Adaptive Non-accumulative Hough Transform in an iterative manner to provide accurate values for the azimuthal orientation θ and the vertical inclination ϕ, so they can be used in turn to correct any inaccurate estimations of the radius R and the velocity v resulting from processing individual radargrams. The information obtained from processing individual radargrams needs to be combined in order to completely locate the buried cylinders in terms of their dimensions and orientations. The basis for this combination is to find aligned detected hyperbola apices within the whole site radargrams, and this means searching for lines in 3D space.

4.1.1 Detecting Lines in 3D Space

A straight line in 3D space passing through an arbitrary point and having the direction vector $\overrightarrow{l}$ may be expressed by

$$r = (x, y, z) = r_1 + k\overrightarrow{l} \tag{4.2}$$

where r is the position vector relative to the origin O, r_1 is a given point on the line and k is a scalar dependent on the position of the point on the line. Since $r_1 = (x_1, y_1, z_1)$ and $l = (a, b, c)$, then Equation 4.2 can be rewritten as

$$r = (x, y, z) = (x_1, y_1, z_1) + k(a, b, c) \tag{4.3}$$

For any value of k there is a unique point $P(x, y, z)$ on the line and a direction vector that can fully describe that line in 3-D space. A *special point* may be identified to describe a line. For a given line in 3-D space, there is only one plane Π through the origin perpendicular to it, and the intersection of that line and the plane can be treated as the special point. Assume there is a line $l = (x, y, z) = (x_1, y_1, z_1) + k(a, b, c)$ in 3D space, and a plane Π that passes through the origin O and perpendicular to l. Let $\mathbf{n}$ be a vector normal to Π, B a fixed point on Π, and $P(x_k, y_k, z_k)$ any point on the plane. Let $OB = r_1$, $OP = r$, then $BP.\mathbf{n} = 0$. Since $BP = r - r_1$, then

$$(r - r_1) \cdot \mathbf{n} = 0 \tag{4.4}$$

Since the plane Π passes through the origin, then the point $(0, 0, 0)$ can be assumed to be the fixed point B. Therefore, $OB = r_1 = (0, 0, 0)$, now Equation 4.4 can be written as

$$r \cdot \mathbf{n} = 0 \tag{4.5}$$

Since $\overrightarrow{l}$ is perpendicular to Π, then the direction-vector of $\overrightarrow{l}$ is the normal-vector to Π. Assuming P to be the intersection of $\overrightarrow{l}$ and Π, we have

$$\Big[(x_1, y_1, z_1) + k(a, b, c)\Big] \cdot (a, b, c) = 0 \tag{4.6}$$

Solving this equation leads to

$$k = \frac{-(ax_1, by_1, cz_1)}{a^2 + b^2 + c^2} \tag{4.7}$$

then P can be obtained from

$$P = (x_1, y_1, z_1) + k(a, b, c) \tag{4.8}$$

For simplicity, the direction-vector $\overrightarrow{l}$ can be assumed to be a unit vector, giving us

$$a = \sin\phi\cos\theta \tag{4.9}$$

$$b = \sin\phi\sin\theta \tag{4.10}$$

$$c = \cos\phi \tag{4.11}$$

where θ and ϕ are the orientations of $\overrightarrow{l}$ in spherical coordinates. Substituting for a, b, and c in Equation 4.8 then

$$P = (x_1, y_1, z_1) + k(\sin\phi\cos\theta, \sin\phi\sin, \cos\phi) \tag{4.12}$$

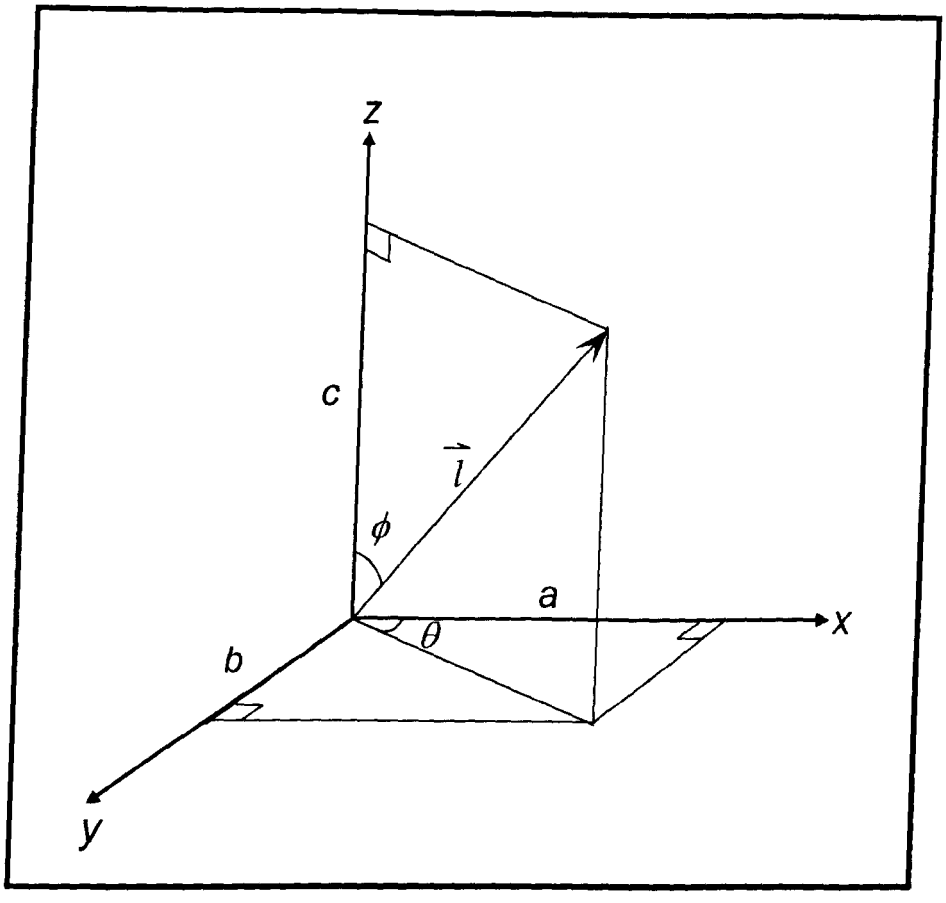

Figure 4.2: Vector representation in spherical coordinates

A straight line in 3D space can be described by the five parameters: x_k, y_k, z_k, ϕ, and θ. When applying the Hough Transform, then each point (x, y, z) in 3D space generates a hyper-surface $(x_k, y_k, z_k, \phi, \theta)$ in the 5D parameter space.

4.1.2 Adaptive Non-Accumulative Hough Transform

The standard implementation of the Hough Transform involves accumulating the votes of a parameter space in a finely quantised accumulator array. The fineness of quantisation is a measure of the accuracy in determining individual parameters. However a fine quantisation means a large accumulator array, specially when the standard 2D HT is employed to detect patterns in 3D. As mentioned in the previous section, a unique 3D line is defined by five parameters: x_k, y_k, z_k, ϕ, and θ. This means that the accumulator array used to detect 3D linear objects has five dimensions, hence, it requires a huge amount of computer memory. Furthermore a searching of peaks in such a big accumulator array is impractical and time-consuming. Each 3D point when mapped into parameter space produces a parameter hyper-surface, and the parameter hyper-surfaces produced by aligned points in 3D intersect at a common point in parameter space. The coordinates of this parameter point characterises the straight line connecting the 3D points [67]. The HT mechanism is based on generating these hyper-surfaces and identifying the parameter point where they intersect.

When noisy data is involved, then not all of the hyper-surfaces produced by collinear points intersect at the same point but in the vicinity of the true intersection. Consequently, a cluster is formed with a barycentre with coordinates very close to the true parameter point. The number of clusters in parameter space indicates the number of possible instances of linear objects in 3D space. Detecting hyper-surface intersection can therefore be approximated by detecting the barycentres in a number of clusters. By using the ANHT, a competitive learning neural network is used to perform the detection of barycentres, instead of using a finely-quantised accumulator. The densest cluster will be treated as a group of the input vectors for the neural

network, and the number of neurons is set to one, hence this neuron will win all the time and its weight vector tends towards the barycentre of the input vectors. The number of the epochs is a user-defined parameter; the larger this number is, the more accurate will be the result and the more computational time is required.

Furthermore, the ANHT involves an intelligent iterative "coarse to fine" calculation strategy for finding only the points that are in the vicinity of the barycentres of clusters. The properties of the ANHT method can be summarised by the following:

- It uses a competitive learning neural network for finding the intersection points in the parameter space, which avoids the time-consuming finely quantized accumulator
- It intelligently redefines the parameter range for the next computation so that an interesting area can be further investigated and the use of a small parameter size becomes possible, which considerably reduces the computer storage requirement
- A filtering process for the parameter space is applied to reduce the effect of outliers
- It automatically estimates the number of significant clusters in parameter space

The ANHT is used in an iterative manner to search for aligned apices and to calculate their corresponding lengths and orientations. Figure 4.3 shows a block diagram of the complete automatic detection-interpretation procedure for subsurface cylindrical targets and indicating the ANHT.

This procedure can be summarised in the following steps:

1. Mapping the detected apices into 3D space

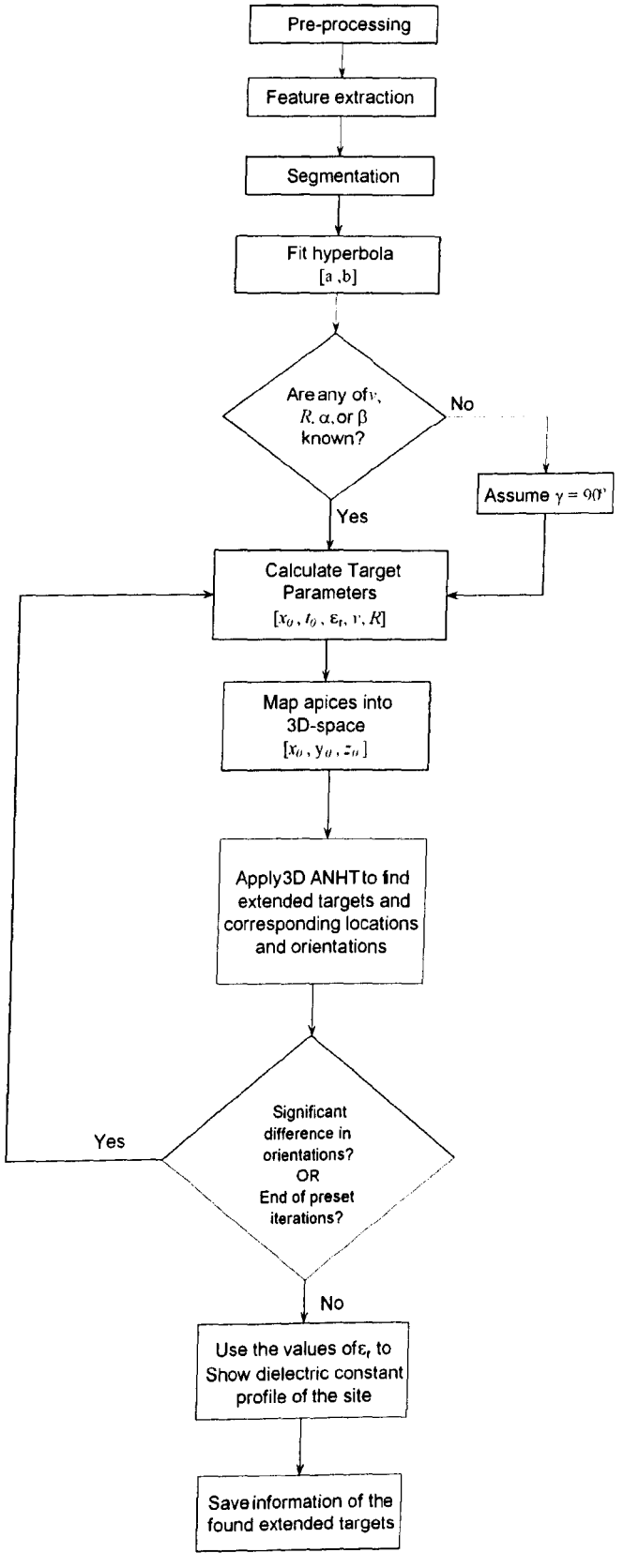

Figure 4.3: Block diagram of the complete automatic detection and interpretation system

2. Searching for aligned points in 3D space by applying the 3D ANHT

3. The orientations θ and ϕ of a detected line are used to correct for the values of α and β.

4. Correcting for the values of R and v, which were calculated from individual radargrams when hyperbola-fitting was applied. These values are then saved along with the corresponding apices-coordinates. From these saved coordinates, it is to be decided to which detected-cylinder a certain apex belongs. When lines are detected by the ANHT, their corresponding orientations are used to correct for the values R, v, and ϵ_r for each detected cylinder via

$$R = \frac{b(a - t_0)\sin\gamma}{a} \tag{4.13}$$

$$v = \frac{2b\sin\gamma}{a} \tag{4.14}$$

$$\epsilon_r = \left(\frac{c}{\hat{v}_s}\right)^2 \tag{4.15}$$

where

$$\hat{v}_s = \frac{v \times \texttt{samples\_per\_scan}}{\texttt{scans\_per\_meter} \times \texttt{range}} \tag{4.16}$$

5. Using the new values of R, v, and ϵ_r to re-map the detected apices according to the calculated orientations.

The procedure described above is repeated as long as a significant change in the values of θ or ϕ is taking place, otherwise it is stopped. Another stopping condition could be a preset number of iterations when reached, the procedure is stopped.

After the system settles, the final values of the relative permittivity at each detected apex are used to generate the permittivity profile of the whole investigated site via fitting a surface of the form $\epsilon_r = f(x, y)$ to the dielectric constant values obtained at the detected target points. This fitting is based on Delaunay triangulation [68], which represents a set of triangles connecting the points to satisfy an "empty circle" property: the circumcircle of each triangle does not contain any of the points. It is used to construct an approximation to a function $\epsilon_r(x, y)$ whose values are only known for a finite set of points (x, y).

4.1.3 Synthetic Site Data

In order to test the proposed system and quantify its performance, a synthetic site was built which models a real site of 20×30 meters. It contains four pipes and a tank in addition to fifteen randomly-distributed point-reflectors. The corresponding target information is detailed in Table 4.1. The site was surveyed using an orthogonal grid of survey-lines spaced one-meter apart and the hyperbolic responses (whether from point-reflectors or cylinders) were modelled on the basis of 512 samples_per_scan, 100 scans_per_meter, and 40 ns range.

The dielectric profile across the site was allowed to vary as if part of the site had been recently excavated and backfilled, and an artificial 'pool' of wet soil created as if to model a source of water. The resulting relative permittivity distribution is shown in Figure 4.4. Figures 4.5 and 4.6 illustrate the presented site in two and

Table 4.1: Synthetic test site target details

Target type	**Length (m)**	R **(cm)**	θ **(degrees)**	ϕ **(degrees)**	**depth to top (cm)**
`Pipe 1`	10	10	0	0	50
`Tank 2`	5	125	90	0	80
`Pipe 3`	14.87	50	45	10	30
`Pipe 4`	10.63	20	45	0	60
`Pipe 5`	13	20	90	0	70

three-dimensional views with the dielectric profile superimposed in contour form.

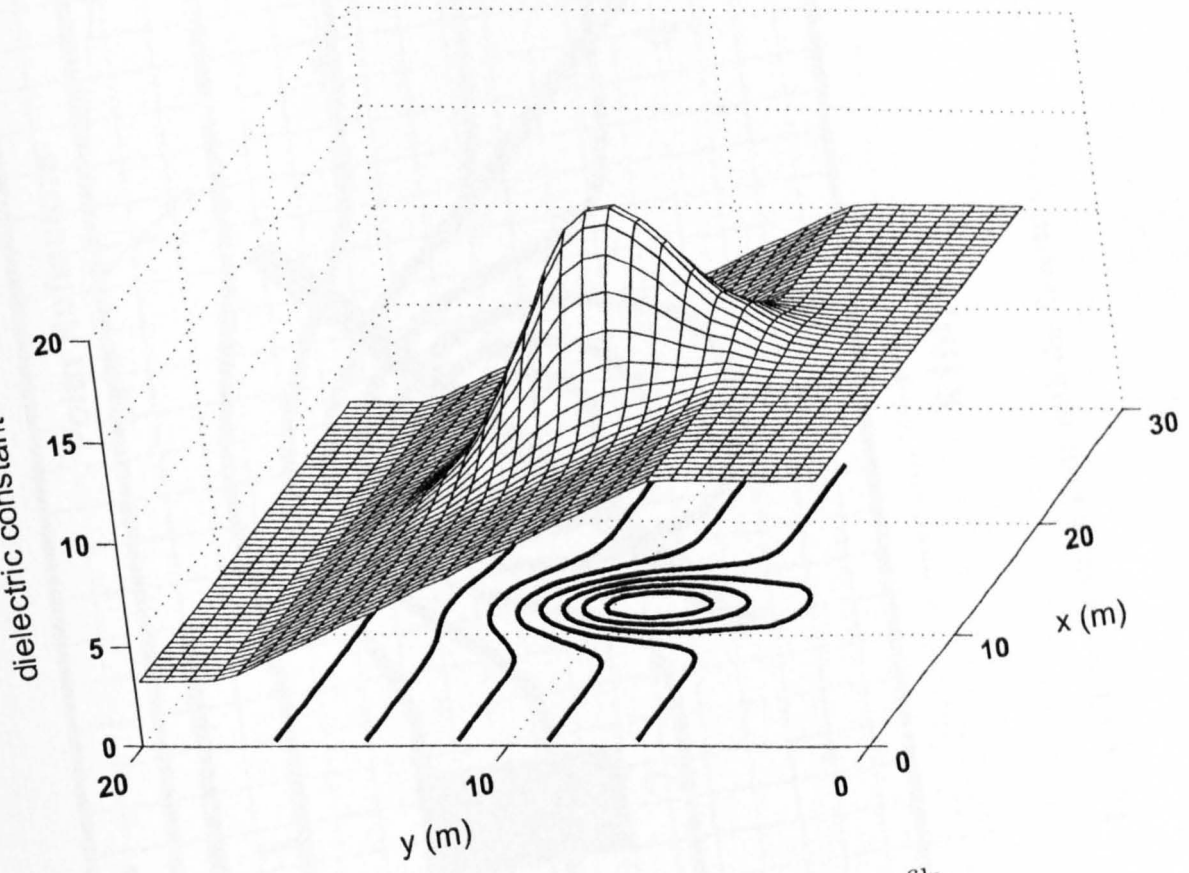

Figure 4.4: The imposed dielectric constant profile

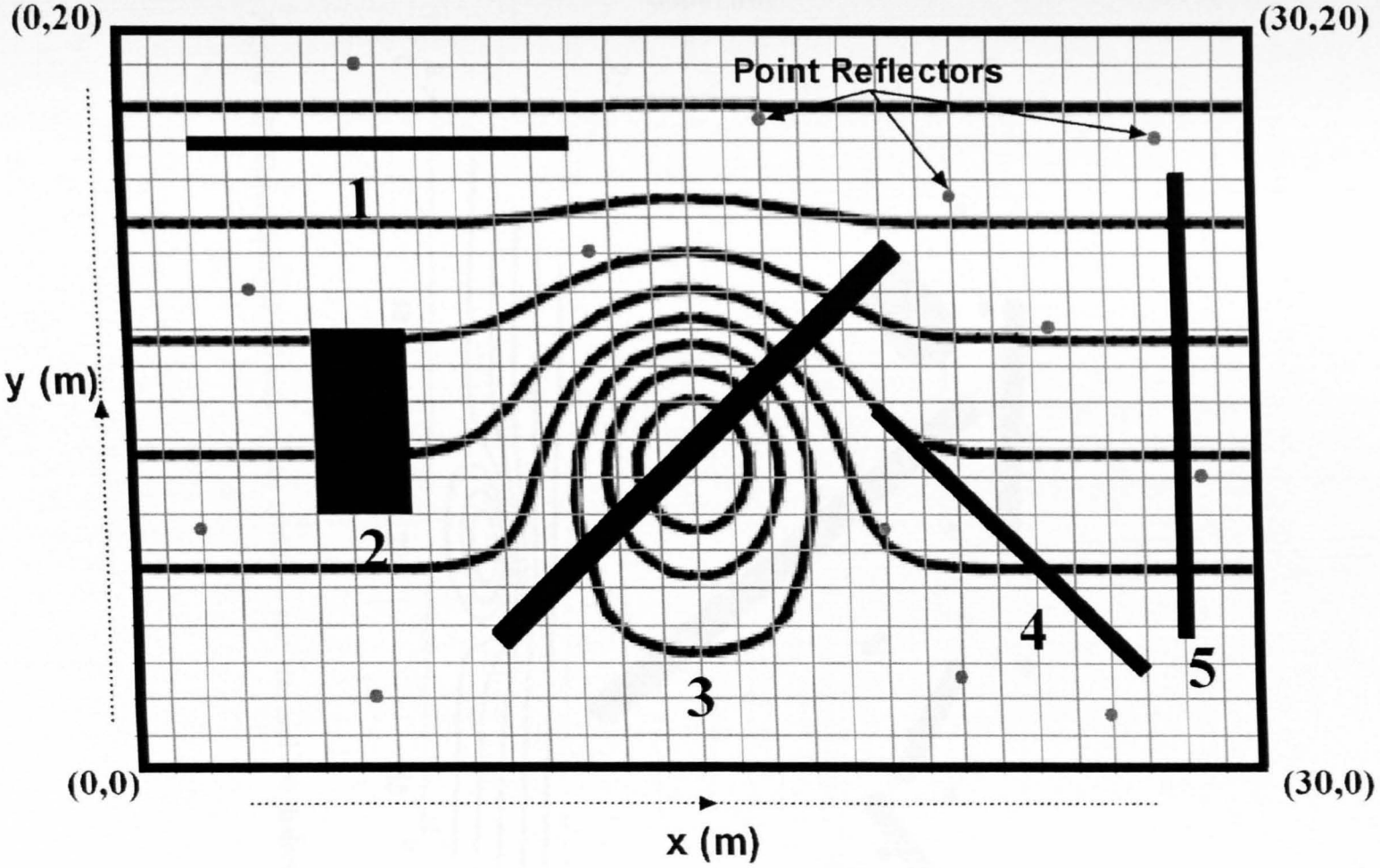

Figure 4.5: Synthetic test site with the dielectric-constant profile indicated

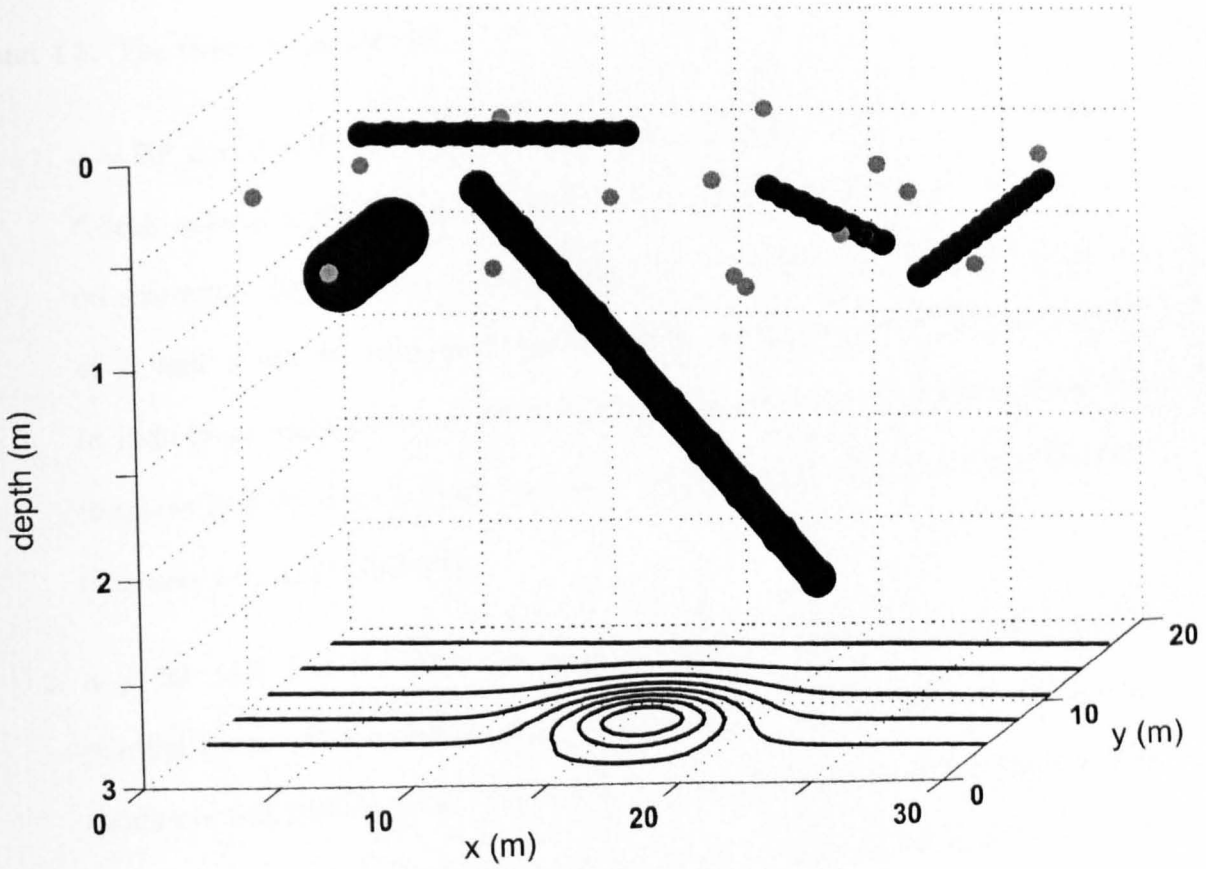

Figure 4.6: Three dimensional view of the synthetic test site and the dielectric profile

4.2 Application Results

In this section, the results of applying the suggested procedure to the synthetic-site are presented. Furthermore, `Pipes 1`, `3`, and `4` were taken as examples for three possible scenarios, as samples of the pipe-parameters obtained from individual radargram processing and using the proposed 3D-iterative method, are shown in Tables 4.2 and 4.3. The three scenarios are:

1. $\alpha = 90°$ and $\beta = 0°$: In this example, `Pipe 1` is considered and it represents the "ideal" case of a pipe buried parallel to the surface and normal to the direction od scanning. As stated in Section 3.2.3 if $\alpha = 90°$ and $\beta = 0°$ then the values of R and v can be calculated directly from fitting the detected hyperbolae in individual radargrams without the need for further processing. When the iterative system was applied, the correct values were obtained from the first iteration with negligible error.

2. $\alpha \neq 90°$ and $\beta = 0°$: This case is represented by `Pipe 4`, where the pipe is parallel to the surface, but at a 45° to the direction of scanning. The stopping condition was fulfilled in the first iteration, when accurate values for the pipe parameters were found with error rates dramatically reduced for the values of ϵ_r, R, and θ in comparison to the values obtained from individual radargrams. Based on the calculated values of ϵ_r, and R from individual radargrams, the pipe's depth was calculated to be 26% deeper than its true depth which may result in disastrous consequences in some of the cases, for example when oil, or utility pipes are involved.

3. $\alpha \neq 90°$ and $\beta \neq 0°$: In this case, `Pipe 3` is represented as it is neither parallel

to the surface nor normal to the direction of scanning. It can be seen from Figures 4.5 and 4.6 that `Pipe 3` lies in the heart of the area were the largest variation in the values of ϵ_r takes place and represents a good example of the information-uncertainty problem with regard to both target and host medium. In this case, the pipe was located 40% deeper than its true depth.

When comparing `Pipe 3` and `Pipe 4` corresponding values Table 4.2 shows the errors in targets parameters and ϵ_r obtained from the hyperbola-fitting stage priori to applying the iterative procedure, while Table 4.3 shows these errors after only one iteration of the suggested procedure. It can be seen the dangerous consequences of relying on broad assumptions, specially with regard to the locations of the targets in terms of their depths and orientations. In the second and third cases, the negligence about α and β has led to wrong estimates about the depths of the pipes, where they were located deeper than they were in reality.

Table 4.2: Errors in target parameters obtained from hyperbola-fitting stage

	Error in Depth (cm)	**Error in ϵ_r**	**Error in R (cm)**	**Error in θ (degrees)**	**Error in ϕ (degrees)**
`Pipe 1`	0	0	0	0	0
`Pipe 4`	10	6.5	10	45	0
`Pipe 3`	10	9	20	45	10

The proposed procedure was successfully applied to the synthetic site and all the five targets were identified and characterised with high accuracy, as shown in Figure 4.7. The above three cases are indications of three different situations where the accuracy of the proposed system can be seen in detecting the targets and extracting full information regarding their radii, depths and orientations.

Furthermore the dielectric constant was calculated with high accuracy at each detected target-apex and the resulting permittivity profile of the whole site was plotted

Table 4.3: Errors in target parameters obtained from the automatic 3D-detection procedure

	Number of iterations	**Error in Depth (cm)**	**Error in ϵ_r**	**Error in R (cm)**	**Error in θ (degrees)**	**Error in ϕ (degrees)**
Pipe 1	1	0	0	0.0001	0.0	0.04
Pipe 4	1	0	0.02	0.001	0.02	0.04
Pipe 3	2	1	2	0.001	0.02	0.66

via fitting a surface to these values of ϵ_r, as was described in the previous section. This is shown in Figure 4.8, where it shows a great similarity to the original profile shown in Figure 4.4.

The obtained shape is the result of surface-fitting to 65 values of ϵ_r obtained from the detected apices, and this is the reason why the shape does not look as smooth as the original profile which is resulted from 60000 values for ϵ_r. moreover, it can be seen that the obtained profile only covers the area where targets exist, while the rest of the site is not covered, but it can be expected that the values of ϵ_r will be within the range of values for the obtained profile. Finding the dielectric profile of the site by itself is a great achievement, where a robust and accurate method is suggested for solving the standing problem of unknown dielectric constant of the host medium.

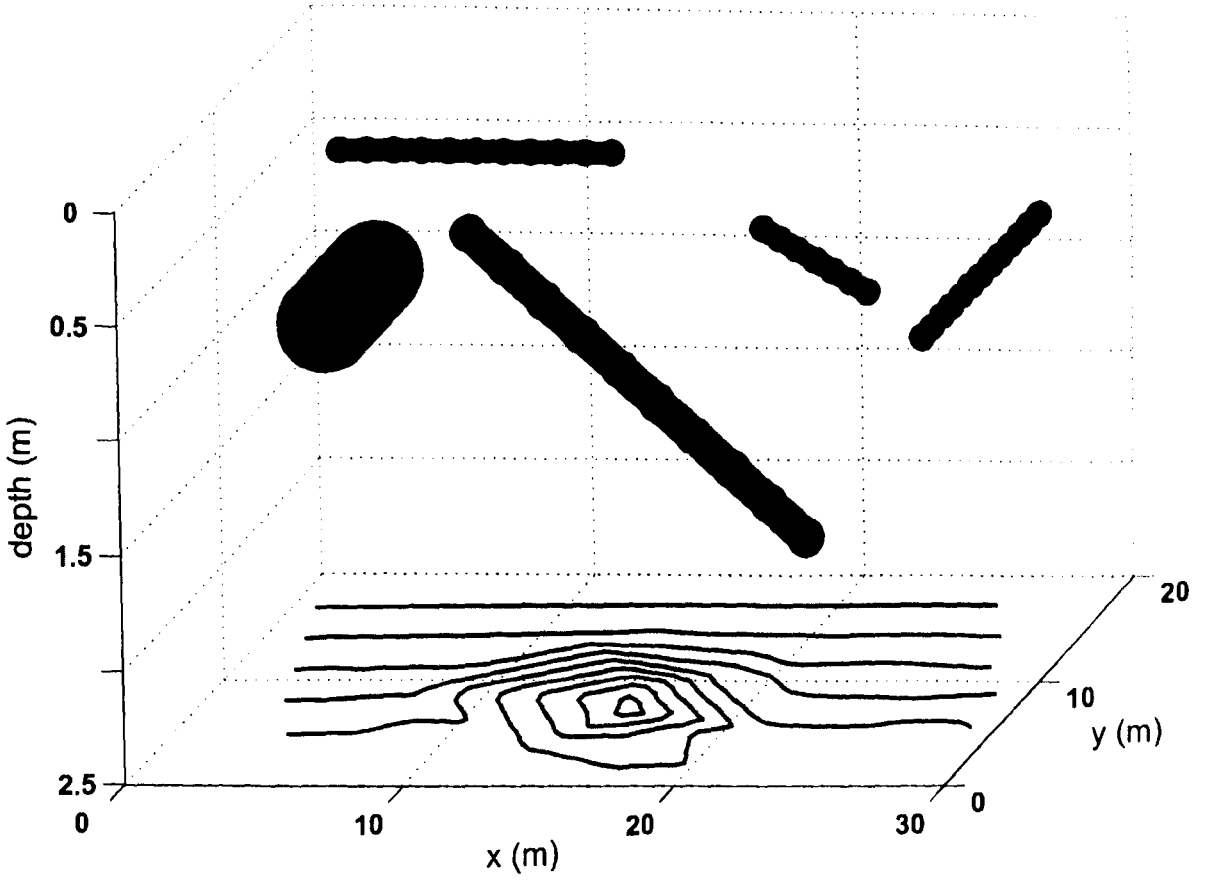

Figure 4.7: The detected targets and the calculated permittivity profile by the proposed system

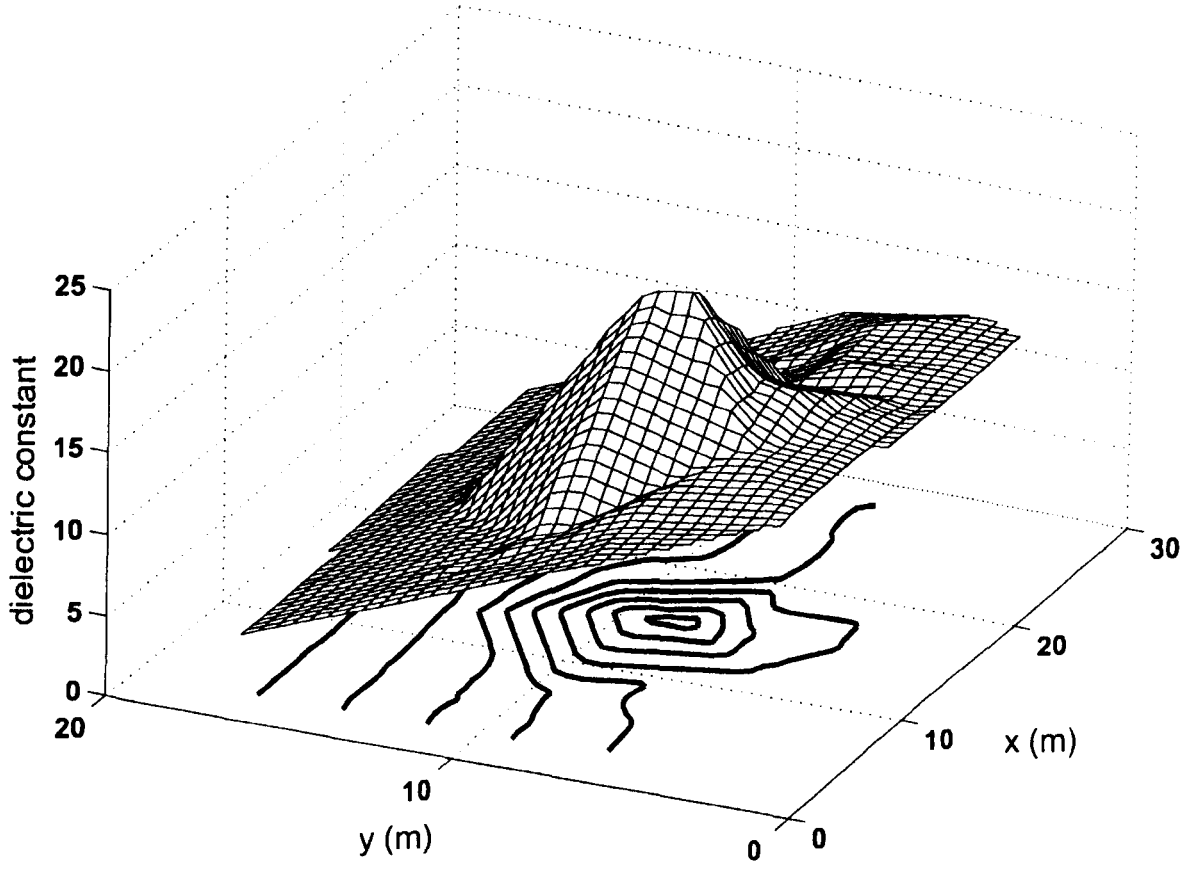

Figure 4.8: The dielectric constant profile obtained by the proposed system

4.3 Advantages of Site Data Fusion

It was mentioned in Section 4.1 that relying on individual radargrams to characterise detected targets may lead to incorrect results with regard to target location and dimensions, and even missing existing targets when a non-homogeneous profile of the relative permittivity exists. This can be seen when comparing Tables 4.2 and 4.3, besides that Figure 4.9 shows parameter convergence vs iterations plots for ϵ_r, θ, and ϕ for case 3, where these parameters rapidly converge towards the correct values after only one iteration of the new procedure. Moreover, Figure 4.10 shows a plot comparing between the points mapped using conventional procedure and those mapped using the multiple radargram procedure, while Figure 4.11 shows a comparison between the multiple radargram procedure mapping result and the true values. It can be seen from these figures the accuracy and robustness of the new procedure on one hand, and on the other hand they show how conventional procedure may miscalculate target parameters, in this case some targets and points were shown to be deeper than they are in reality, while points of `pipe 3` are shown as a curvature which means they may be considered redundant.

This shows clearly that the presented procedure represents a robust solution to the uncertainty problem about targets parameters and medium type, which results from making broad assumptions and relying on individual-scan processing.

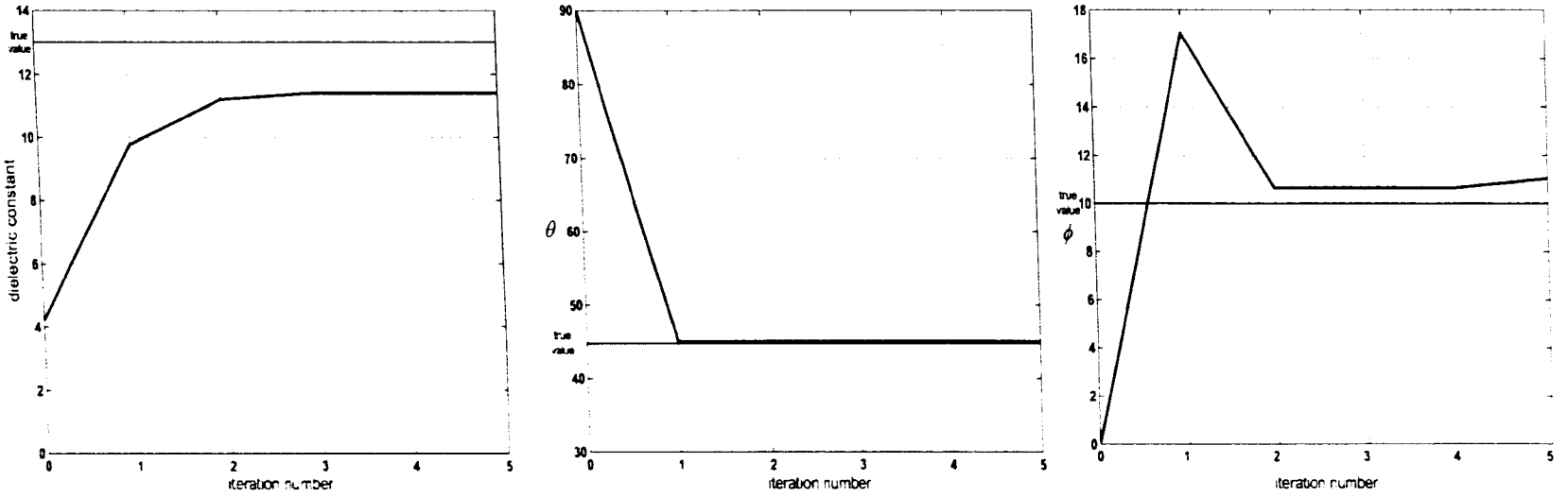

(a) Convergence of values of ϵ_r (b) Convergence of values of θ (c) Convergence of values of ϕ

Figure 4.9: Parameter-convergence-vs-iterations plots

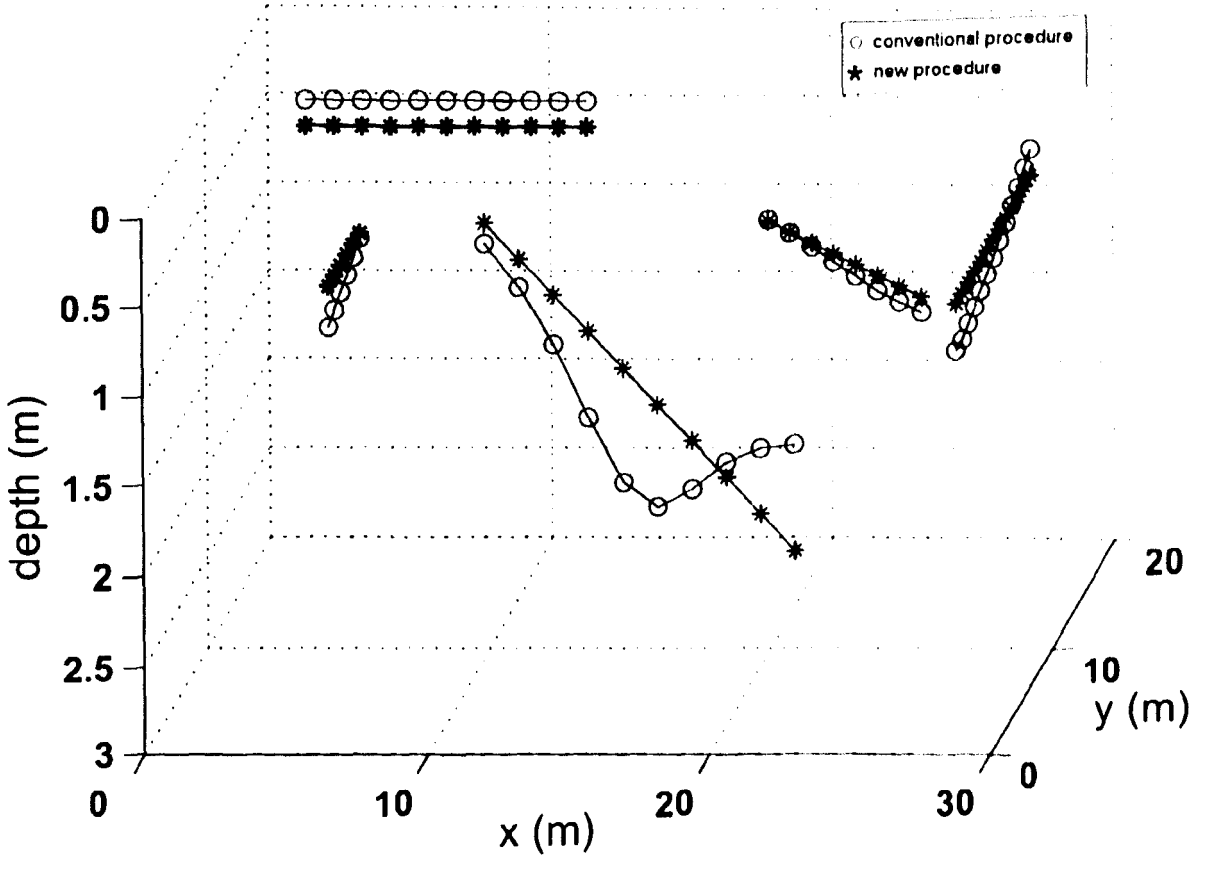

Figure 4.10: Mapping result of the multiple radargram procedure compared to conventional procedure

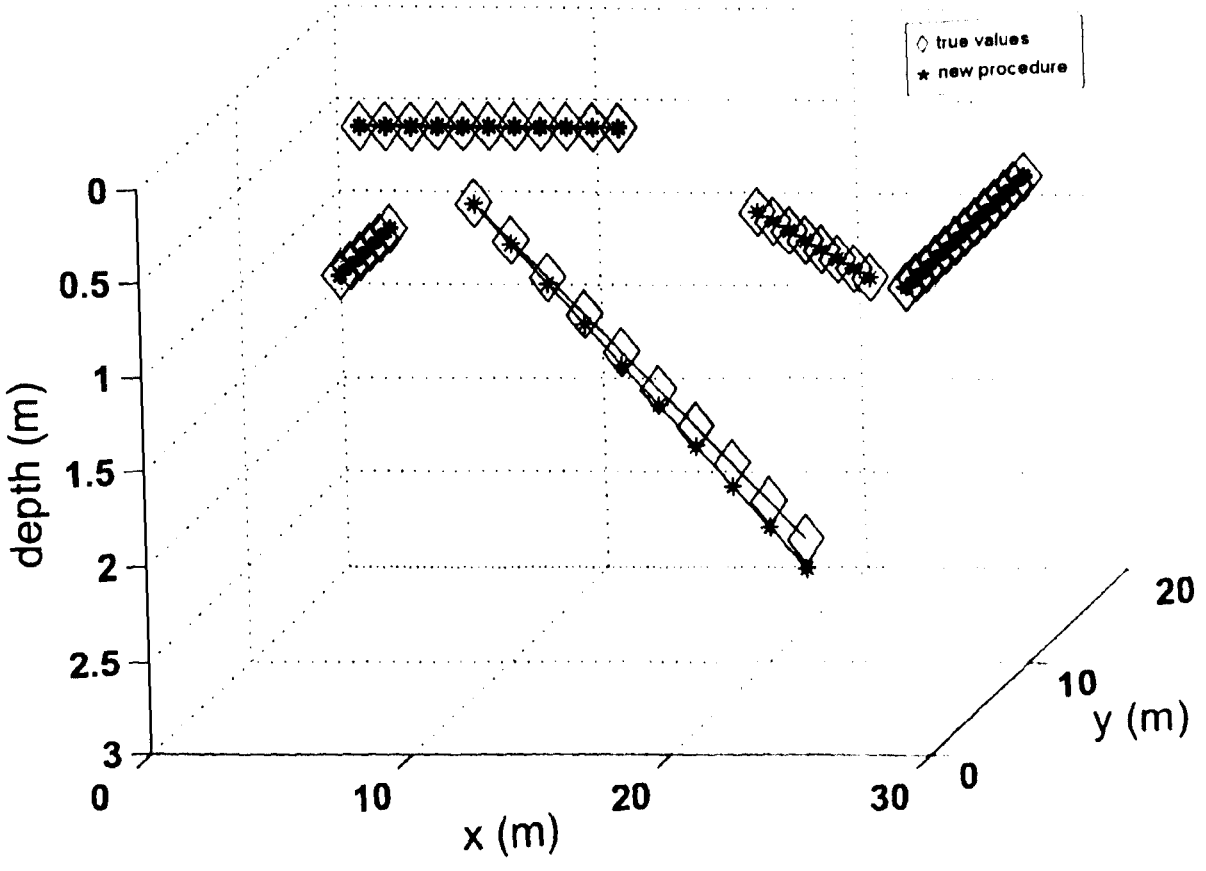

Figure 4.11: Mapping result of the multiple radargram procedure compared to true values

4.4 Computational demands

As mentioned in Section 1.5, one of the main objectives are set in this study is to achieve an on-site application in near-real-time. Hence the overall performance of the presented system needs to be quantified from the time-cost prospective. It is expected that the target-detection stage is a high-time costing stage of the automatic system, as it involves searching the collected data for targets via extracting features that makes the automatic-detection of these targets possible. The test images used for this purpose are collected from Area 3 in the test site [49] which is described in Appendix B. This area is 20×12 meter, and it is covered by 32 radargrams with an average number of scans of about 2000 scans per radargram. The sample radargram shown in Figure 3.15 represents file 31, and it is a 512×1800 pixel image. This file was subjected to detection (using the regional-features method), segmentation, and hyperbola-fitting and target-information calculation stages, and the total time cost was about 17 seconds. It is to be stated here that this cost varies from one radargram to another depending on the number of detected targets as well as the size of the image, so when these operations were applied to the whole 32 radargrams of Area 3, the total time cost was 21 minutes which is an excellent result.

When the multiple radargram procedure was applied to the synthetic site, the total time required for detecting the five targets in 3D space was 3:40 hours, which is the time that the ANHT[1] consumed to detect these targets. Despite this relatively high cost, the procedure is considered essential for accurate characterisation of cylindrical targets and for the outstanding achievement of finding the permittivity profile for the investigated site.

[1] the neural network used by the ANHT was set to 3000 epochs

Finally, it is to be mentioned here that the PC used for this operation is a dual-Pentium® III 1000 MHz processor and 768 MB RAM running Matlab 6.5. It is expected that the computational time would drop enormously when the Matlab code is compiled to C-language, which achieves the objective of on-site near real-time processing.

4.5 Conclusions

This chapter presents a novel procedure for processing target-points which are detected in individual radargrams from the previous stages. The procedure involves mapping the detected points into 3-dimensional space and applying Adaptive Non-accumulative Hough Transform (ANHT) in an iterative manner to detect aligned points in 3D and find their corresponding azimuth and vertical orientations. The calculated angles are then used to correct for the radius and permittivity values obtained from individual radargrams.

Furthermore, a synthetic test site is built with a number of point reflectors and cylindrical targets arranged at different depths and orientations, and a varying relative permittivity profile is set to cover the site. When applied to the site, the automatic procedure has shown high accuracy in detecting the aligned points and correcting for their corresponding parameters with a low percentage error.

When the detected aligned-points resulted from this procedure and those detected using conventional method were compared to true values, the difference in accuracy was quite clear in favour of the new procedure. Moreover, the permittivity profile for the site was found using this procedure with a high accuracy in comparison to the true profile.

The only limiting factor with the ANHT procedure is its relatively high time consumption, though it is considered crucial for the target interpretation process when information about the investigated site is not available, while this final stage will not be needed when orientations of the buried cylinders are known and there is no demand on the dielectric constant profile. In this case a considerable amount of time will be saved.

This system of combining information from individual and multiple radargrams to correct for calculated cylindrical-targets' data and find a dielectric-constant profile of the investigated site, is the first published automatic procedure for this purpose, and the achieved results proves it to be highly efficient and reliable for rapid detection and interpretation of subsurface cylindrical objects.

Chapter 5

Conclusions and Recommendations

This study addressed the tasks of automatic detection and interpretation of subsurface objects, particularly localised point reflectors and linearly extended cylinders. Novel processing techniques were developed that treated the radar data both as ensembles of time series and as images, combining signal and image processing to yield detailed interpretations of radar data in time-scales suitable for on-site near-real time operation.

A variety of features-extraction techniques were presented and used along with artificial neural networks as pattern recognition and classification tool with detailing complete feature classification routines based on supervised neural networks. A robust pattern recognition technique was presented, based on selected regional features to enable the detection of hyperbolic shapes in the data with extremely reduced computation time. Combining this with a novel hyperbola-specific least square fitter resulted in high accuracy estimates of buried targets information with a degree of tolerance to the effects of noise and clutter.

A variety of approaches were presented and implemented at each intermediate

stage for the above tasks, and the results compared as appropriate, in terms of feasibility, computational costs, quality of results, Classification rates, and false alarm rates. A brief discussion of the merits and drawbacks of several of these approaches follows.

5.1 Conclusions

It must be stressed that GPR can never produce definitive geometrical results given the diversity of the subterraneous environment and the nature of the electromagnetic configuration, but its convenience as a rapid non-invasive site investigation tool has lead to a degree of over-reliance on this particular geophysical technique. This in turn has cultivated a culture of quasi-scientific interpretation of these radargrams, with the inevitable errors often reflecting negatively and unfairly on the technique itself.

In the light of the objectives set for this work in Section 1.5, it can be stated here that all these objectives are met with high efficiency.

The first objective of highlighting of feature zones was covered in Chapter 2, where the aim of all the target detection techniques presented is to discriminate between two classes of GPR reflections; targets (such as pipes, tanks, cables, and voids), and non-targets (such as clutter and noise). Typically, this stage acts as a bottleneck in any automatic detection-interpretation system, as it is computationally expensive.

In all aspects, the regional features technique have proven to be the most effective among all supervised neural network region selection approaches described in Chapter 2 as it has the unique capability of selecting hyperbolic-shaped regions without further edge detection procedure needed. Moreover, this technique has the lowest

time cost among all other techniques, which has overcome the problem of computational cost that typically the detection stage suffers from. Although this technique points the relatively highest proportion of false alarms, yet the recorded figure is very low. The B-scan statistics technique has a much lower false alarm rate with a almost twice the time-cost of that of the regional features approach. The A-scans statistics technique has achieved the lowest false alarm rate on the expense of a relatively big increase in the computational cost. A double-stage classifier is suggested to combine the hyperbolic-shapes detection property of the regional-features technique and the ignorable false alarm rate of the B-scan statistics technique. The low time cost of both techniques has kept this technique within the desired near-real time performance, and the result was a more robust and accurate classifier.

The regional-features technique has reduced the edge-detection routines by a great extent, with only region-completion and skeletonisation procedures involved. The aim behind them was to produce a hyperbolae points ready for the following target-information extraction stage. With the greatly reduced radargrams data resulted from the previous target detection stage, the time cost of the edge detection stage is very low.

The objective of estimating the diameter and orientations of cylindrical targets was covered in Chapters 3 and 4. Presenting a comprehensive model for hyperbolic signatures resulted from buried cylinders, has filled the gap caused by the lack of information and led to making broad assumptions about the radius and orientations of such cylinders, in addition to the velocity of propagation. it was shown how wrong assumptions may lead to disastrous consequences especially in applications where targets need to by localised with high accuracy.

The least-square-hyperbola-specific fitter produced in this work has overcome the

shortcoming which the conventional polynomial fitters suffer from, where they depend on accurate estimates of velocity which in turn not always readily available. The ability of the novel fitter to produce numerical information about the fitted points, has made it possible to produce accurate calculations of target-related information, when combined with the derived hyperbolic-signature model. This fitter suffers from the limitation that it is only capable of calculating two parameters if the third is known; the radius, the combined orientations angle, or the velocity of propagation.

Chapter 4 also covered the fourth and fifth objectives, where The shortcoming of inaccurate estimation for the cylinder orientations was overcome via using multiple scans in a novel iterative routine which combines information extracted from various cues from within the data and applying 3-dimensional non-accumulative Hough transform to find extended cylinders in the investigated site and calculate both their azimuth and vertical orientations. These orientations are then used to correct for the values of target radius and depth which were calculated from individual radargrams. The only limitation of this technique lies in its relatively high time consumption which makes it the most time-costing stage of the presented system. Moreover, the information obtained from the iterative routine are used to map the detected targets in 3D.

Furthermore, the presented procedure was also used to produce a dielectric constant profile for the whole site based on fitting a plane to the values of the relative permittivity obtained from detected points. This strongly pushes towards a more accurate interpretation for the collected data and a better understanding for the nature of the investigated site.

As for the important objective of on-site near-real time processing, it was shown in Section 4.4 how the presented procedure was quit fast in processing site data and

producing final interpretation results. Hence, the presented system can be applied on-site to produce a final interpretation report in a relatively short time.

5.2 Recommendations

In order to enhance the quality of the raw GPR data by increasing the content of relevant site information, following are some recommendations regarding data acquisition:

- For maximum feature detectability a multichannel GPR would enable to gather signals from the antennae with different bandwidths or from antenna's arrays. By summing the signals in channels with different weights would be used to control the antenna patterns and change the direction of the main lobe. The main destination of the named systems is their using as a tool for processing of the mine searching algorithms. Results of experiments are cited in the report.

- Cross-polarised antennae can be used to make them more sensitive to cylindrical objects (like pipes), independent of alignment of such objects with regard to the antennae. The antennae need to be configured with one antenna electric field perpendicular to the other.

5.3 Further Work

A major achievement of this study is overcoming the relative bottleneck caused by the region selection stage, yet the presented regional-features technique could be improved to reduce its false alarm rate. This could be achieved via further investi-

gating region descriptors and combining one or more region segmentation techniques, with time-cost issue kept in mind.

This system could be expanded to cover other types of targets such as land-mines and other unexploded ordinance, where modelling and analysing procedures (similar to the ones presented by this study) could be applied to develop this field.

The dielectric constant profile-calculation procedure could be developed to cover the possibility of different medium layers. This could be used, along with the iterative 3D Hough transform algorithm, to correct for targets points which lost their alignments due to the change in relative permittivity.

Bibliography

[1] Geophysical Survey Systems Inc. Products software and applications. *Internet site http://www.geophysical.com/products.htm.*

[2] D. J. Daniels. *Surface Penetrating Radar.* The Institution of Electrical Engineers, London, 2nd edition, 2004.

[3] D. J. Daniels, D. J. Gunton, and H. F. Scott. Introduction to subsurface radar. *IEE Proceedings, Part F: Communications, Radar and Signal Processing*, 135-f:278 - 320, 1988.

[4] J. J. Daniels, R. Roberts, and M. Vendi. Ground penetrating radar for the detection of liquid contaminants. *Journal of Applied Geophysics*, 33:195–207, 1995.

[5] B. Sai and L. Ligthart. Improved GPR data preprocessing for detection of various land mines. *in Eighth International Conference on Ground Penetrating Radar, Proceedings of SPIE*, 4084:80–84, 2000.

[6] A. Merwe, I. Gupta, and L. Peters Jr. A clutter reduction technique for GPR data from mine like targets. *Proceedings of SPIE*, 3710:1094–1106, 1999.

[7] D. Carevic. Wavelet based method for detection of shallowly buried objects

from GPR data. *Information, Decision and Control Conference Proceedings*, Cat. No.99EX251:201–206, IEEE 1999.

[8] D. Carevic, I. Chant, and T. Caelli. Feature extraction and classification of minelike targets from GPR data using gaussian mixture models. *Information, Decision and Control Conference Proceedings*, Cat. No.99EX251:329–334, IEEE 1999.

[9] B. Ulug, J. Zhao, and S. Ahalt. Feature-based classification of SAR data using RBF networks. *Conference on Signal Processing, Sensor Fusion, and Target Recognition IV, Proceedings of SPIE*, 2484:583–594, 1995.

[10] P. Gamba and S. Lossani. Neural detection of pipe signatures in ground penetrating radar images. *IEEE Transactions on Geoscience and Remote Sensing*, 38(2):790–798, 2000.

[11] R. Lotlikar and R. Kothri. Bayes-optimality motivated linear and multilayered perceptron-based dimentionality reduction. *IEEE Transactions on Neural Networks*, 11(2):452–463, 2000.

[12] W. Al-Nuaimy, Y. Huang, M. Fang, V. Nguyen, and A. Eriksen. Automatic detection of buried utilities and solid objects with GPR using neural networks and pattern recognition. *Journal of Applied Geophysics*, 43:157–165, 2000.

[13] W. Al-Nuaimy, Y. Huang, V. Nguyen, and A. Eriksen. Automatic feature selection for unsupervised image segmentation. *Applied Physics Letters*, 77(8):1230 1232, 2000.

[14] G. Grandjean and H. Durand. Radar unix: a complete package for GPR data processing. *Journal of Computers and Geosciences*, 25:141–149, 1999.

[15] W. Al-Nuaimy, H. Lu, S. Shihab, and A. Eriksen. Automatic mapping of linear structures in 3-dimensional space in ground penetrating radar data. *Proceedings of IEEE/ISPRS Joint Workshop on Remote Sensing and Data Fusion Over Urban Areas*, Rome, Italy, 2001.

[16] L. Capineri, P. Grande, and J. Temple. Advanced image processing technique for real-time interpretation of ground penetrating radar images. *International Journal of Imaging Systems and Technology*, 9(1):51–59, 1998.

[17] J. Kruk and J. Zeeman. Multicomponent imaging of different objects with different strike orientations. *in Ninth International Conference on Ground Penetrating Radar, Steven K. Koppenjan and Hua Lee, Editors, Proceedings of SPIE*, 4758:150–155, 2002.

[18] D. Smith and P. Brown. Advances in directional borehole radar data analysis and visualisation. *in Ninth International Conference on Ground Penetrating Radar, Steven K. Koppenjan and Hua Lee, Editors, Proceedings of SPIE*, 4758:251–255, 2002.

[19] R. Roberts and D. Cist. Enhanced target imaging in 3D using gpr data from orthogonal profile lines. *in Ninth International Conference on Ground Penetrating Radar, Steven K. Koppenjan and Hua Lee, Editors, Proceedings of SPIE*, 4758:256–261, 2002.

[20] B. Scheers, M. Acheroy, and A. Vorst. Migration technique based on the time-domain model of the ground penetrating radar. *in Subsurface and Surface*

Sensing Technologies and Applications, Cam Nguyen, Editor, Proceedings of SPIE, 4491:111–119, 2001.

[21] J. Binningbo, E. Eide, and J. Hjelmstad. 3D migration of GPR array antenna data. *in Eighth International Conference on Ground Penetrating Radar, Proceedings of SPIE*. 4084:459–463, 2000.

[22] H. Hayakawa, A. Nadamoto, and S. Uesaka. 3D imaging of buried objects using arbirary scanning GPR. *in Eighth International Conference on Ground Penetrating Radar, Proceedings of SPIE*, 4084:273–276, 2000.

[23] J. Kruk and E. Slob. Effective source wavelet determination. *in Ninth International Conference on Ground Penetrating Radar, Steven K. Koppenjan and Hua Lee, Editors, Proceedings of SPIE*, 4758:144–149, 2002.

[24] H. Lee. Synthetic-aperture GPR imaging with pulse-echo and step-frequency FMCW systems. *in Ninth International Conference on Ground Penetrating Radar, Steven K. Koppenjan and Hua Lee, Editors, Proceedings of SPIE*, 4758:130–134, 2002.

[25] R. Brown, B.Himed, E. Lynch, and M. Wicks. Spatially adaptive ground penetrating radar. *in Eighth International Conference on Ground Penetrating Radar, Proceedings of SPIE*, 4084:168–173, 2000.

[26] C. Stolte and K. Nick. Eccentricity-migration: a method to improve the imaging of pipes in radar reflection data. *The Fifth International Conference on Ground Penetrating Radar, Ontario, Canada, Expanded Abstracts, Proceedings*, pages 723–733, 1994.

[27] G. Olhoeft. Maximizing the information return from ground penetrating radar. *Journal of Applied Geophysics*, 43:175–187, 2000.

[28] W. Al-Nuaimy, H. Lu, S. Shihab, and A. Eriksen. Automatic mapping of linear structures in 3-dimensional space in ground penetrating radar data. *Proceedings of IEEE/ISPRS Joint Workshop on Remote Sensing and Data Fusion Over Urban Areas, Rome*, 2001.

[29] S. Shihab, W. Al-Nuaimy, Y. Huang, and A. Eriksen. Neural network target identifier based on statistical features of GPR signals. *in Ninth International Conference on Ground Penetrating Radar, Steven K. Koppenjan and Hua Lee, Editors, Proceedings of SPIE*, 4758:135–138, 2002.

[30] S. Shihab, W. Al-Nuaimy, and A. Eriksen. Image processing and neural network techniques for automatic detection and interpretation of ground penetrating radar data. *Proceedings of 6th WSEAS International Multi-conference on Circuits, Systems, Communications and Computers*, 2002.

[31] S. Shihab, W. Al-Nuaimy, and A. Eriksen. Image processing and neural network techniques for automatic detection and interpretation of ground penetrating radar data. *WSEAS Advances in Circuits, Systems and Signal Processing*, pages 360–363, 2002.

[32] S. Shihab, W. Al-Nuaimy, Y. Huang, and A. Eriksen. Neural networks classifier for detecting subsurface objects. *Proceedings of IEE/EPSRC Joint National Conference PREP2002, Nottingham*, 2002.

[33] W. Al-Nuaimy, H. Lu, S. Shihab, and A. Eriksen. Automatic 3-dimensional mapping of features using GPR. *in Ninth International Conference on Ground*

Penetrating Radar, Steven K. Koppenjan and Hua Lee, Editors, Proceedings of SPIE, 4758:121–124, 2002.

[34] W. Al-Nuaimy, Y. Huang, S. Shihab, and A. Eriksen. Automatic target detection in GPR data. *in Ninth International Conference on Ground Penetrating Radar, Steven K. Koppenjan and Hua Lee, Editors, Proceedings of SPIE*, 4758:139–143, 2002.

[35] W. Al-Nuaimy, Y. Huang, S. Shihab, and A. Eriksen. Unsupervised segmentation of subsurface radar images. *in Ninth International Conference on Ground Penetrating Radar, Steven K. Koppenjan and Hua Lee, Editors, Proceedings of SPIE*, 4758:635–638, 2002.

[36] S. Shihab, O.Zahran, and W. Al-Nuaimy. Time-frequency characteristics of ground penetrating radar reflections from railway ballast and plant. *Proceedings IEEE 2002 High Frequency Postgraduate Student Colloquium, (IEEE catalogue no.: 02TH8642)*, Imperial College, London, UK,2002.

[37] O. Zahran, S. Shihab, and W. Al-Nuaimy. Comparison between surface impulse ground penetrating radar signals and ultrasonic time-of-flight diffraction signals. *Proceedings IEEE 2002 High Frequency Postgraduate Student Colloquium, (IEEE catalogue no.: 02TH8642)*, Imperial College, London, UK, 2002.

[38] O. Zahran, S. Shihab, and W. Al-Nuaimy. Recent developments in ultrasonic techniques for rail-track inspection. *Proceedings of the Annual Conference of the British Institute of Non-Destructing Testing NDT 2002*, pages 55-60, Southport, UK, 2002.

[39] S. Shihab, W. Al-Nuaimy, Y. Huang, and A. Eriksen. Automatic region-based shape discrimination of ground penetrating radar signatures. *Proceedings of the Symposium on the Application of Geophysics to Environmental and Engineering problems SAGEEP2003*, San Antonio, USA, 2003.

[40] S. Shihab, W. Al-Nuaimy, Y. Huang, and A. Eriksen. A comparison of segmentation techniques for targets extraction in ground penetrating radar data. *Proceedings of the 2nd International Workshop on Advanced Ground Penetrating Radar (IWAGPR)*, Delft, Netherlands, 2003.

[41] W. Al-Nuaimy, Y. Huang, and S. Shihab. Multi-channel filtering approach for unsupervised segmentation of subsurface radar images. *Environmental and Engineering Geophysics*, 8:93–101, 2003.

[42] O. Zahran, S. Shihab, and W. Al-Nuaimy. Time-frequency techniques applied to TOFD for the automation of rail-track inspection. *Railway Engineering 2003 Conference Proceedings*, UK, 2003.

[43] S. Shihab and W. Al-Nuaimy. A comparison of segmentation techniques for targets extraction in ground penetrating radar data. *Near-Surface Geophysics*, 2(1):49–57, 2004.

[44] O. Zahran, S. Shihab, and W. Al-Nuaimy. Discussion of the ability of defect classification in weld inspection using ultrasonic time-of-flight-diffraction technique. *Proceedings of the IEE/EPSRC Joint National Conference PREP2004*, UK, 2004.

[45] S. Shihab, W. Al-Nuaimy, and A. Eriksen. Radius estimation for subsurface cylindrical objects detected by ground penetrating radar. *Proceedings of the*

Tenth International Conference on Ground Penetrating Radar, 1:319–322, Delft, Netherlands, 2004.

[46] W. Al-Nuaimy, S. Shihab, and A. Eriksen. Data fusion for accurate characterisation of buried cylindrical objects using GPR. *Proceedings of the Tenth International Conference on Ground Penetrating Radar*, 1:359–362, Delft, Netherlands, 2004.

[47] S. Shihab and W. Al-Nuaimy. Radius estimation for subsurface cylindrical objects detected by ground penetrating radar. *Subsurface Sensing Technologies and Applications*, 6(2):1–16, 2005.

[48] W. Al-Nuaimy and S. Shihab. Data fusion for accurate characterisation of buried cylindrical objects using GPR. *IEEE Transactions on Geoscience and Remote Sensing*, 2005.

[49] http://www.le.ac.uk/geology/iah/research/EIGG/eigghp.html. Environmental and Industrial Geophysics Group (EIGG) Test Sites - University of Leicester.

[50] A. Papoulis. *Probability, Random Variables, and stochastic Processes.* McGraw-Hill, USA, 1984.

[51] R. Gonzalez and H. Woods. *Digital Image Processing.* Addison Wesley, 1992.

[52] W. Al-Nuaimy. *Automatic Detection of Subsurface Features in Ground-Penetrating Radar Data.* PhD thesis, University of Liverpool, 1999.

[53] E. R. Kanasewich. *Time Sequence Analysis in Geophysics*, pages 96–118. University of Alberta Press, Canada, second revised edition, 1975.

[54] M. Bartlett. Periodogram analysis and continuous spectra. *Nature*, pages 666-668, 1948.

[55] L. Cohen. *Time-Frequency Analysis.* Prentice Hall, Inc., USA, 1995.

[56] Daubechies. Time-frequency localisation and signal analysis. *IEEE Transactions on Information Theory*, 36(5):961–1005, 1990.

[57] F. Tomita and S. Tsuji. *Computer Analysis of Visual Textures.* Kluwer Academic Publishires, USA, 1990.

[58] M. Tuceryan and A. Jain. *Handbook of pattern recognition and computer vision.* Scientific Publishing Company, Singapore, 1993.

[59] j. Sklansky. Image segmentation and feature extraction. *IEEE Transactions on Systems, Man and Cubernetics*, (8):237–247, 1978.

[60] P. Ohanian and R. Dubes. Performance evaluation for four classes of textural features. *Pattern Recognition*, 25(8):819–833, 1992.

[61] W. McCulloch and W. Pitts. A logical calculus of the ideas immanent in nervous activity. *Bulletin of Mathematical Biophysics*, (7):115–133, 1943.

[62] Y. Nagashima, H. Saito, S. Kobayashi, and M. Jun-ichi. Automatic recognition of hyperbolic patterns in underground cross-sectional images. *Proceedings of the Symposium on the Application of Geophysics to Engineering and Environmental Problems*, pages 953–956, 1996.

[63] T. Sato. Automatic data processing procedure for ground probing radar. *IEICE Transactions on communications*, E77-B(6):831–837, 1994.

[64] A. Fitzgibbon, M. Pilu, and R. Fisher. Direct least-squares fitting of ellipses. *IEEE Transactions on Pattern Analysis and Machine Intelligence*, 21(5):476–480, 1999.

[65] R. Haralick and L. Shapiro. *Computer and Robot Vision.* Addison-Wesley, 1992.

[66] F. Bookstein. Fitting conic sections to scattered data. *Computer Graphics and Image Processing*, 9:56–71, 1979.

[67] J. Illingworth and J. Kittler. A survey of the hough transform. *Computer vision Graphics and Image processing*, 44:87–116, 1988.

[68] R. Dwyer. A faster divide and conquer algorithm for constructing delaunay triangulations. *Algorithmica*, 2:137–151, 1989.

[69] Mathworks. *Using MATLAB version 5.* The Math Works Inc., USA, 1999.

[70] S. Yu, R. Mehra, and T. Witten. Automatic mine detection based on ground-penetrating radar. *Proceedings of SPIE*, 3710:961–972, 1999.

[71] W. Sarle. Neural network frequently aseked questions. *Internet site, ftp://ftp.sas.com/pub/neural/faq.html.*

[72] C. Liu and H. Wechsler. Robust coding schemes for indexing and retrieval form large face database. *IEEE Transactions on Image Processing*, 9(1):132–137, 2000.

[73] P. Gader, J. Keller, and H. Liu. Landmine detection using fuzzy clustering in darpa backgrounds data collected with geo-centers ground penetrating radar. *SPIE*, 3392:1139–1149, 1998.

[74] A. Merwe and J. Gupta. A novel signal processing technique for clutter reduction in GPR mesuremants of small, shallow landmines. *IEEE Transactions on Geoscience and Remote Sensing*, 38(6):2627–2637, 2000.

[75] C. Overman and J. Kurtz. Ground penetrating radar processing in a dedicated graphical software environment. *SPIE*, 3704:95–105, 1999.

[76] S. Qian and D. Chen. *Joint Time-Frequency Analysis, Methods and Applications.* Prentice Hall PTR, 1996.

[77] J. Carcion and G. Seriani. An electromagnetic modelling tool for the detection of hydrocarbons in the subsoil. *Geophysical Prospecting*, 48:231–256, 2000.

[78] J. M. Zurada. *Introduction to Artificial Neural Systems.* West Publishing, USA, 1992.

[79] C. Kenney, Y. Deng, B. Manjunath, and G. Hewer. Peer group image enhasment. *IEEE Transactions on Image Processing*, 10(2):326–334, 2001.

[80] L. Astanina, V. Geppener, V. Kaftasjev, and M. Sokolov. Ultrawideband ground probing radar signal processing methods. *Procedings of infix-image and multidimesional digital signal processing*, pages 259–261, 1998.

[81] N. Budko, R. Remis, and P. van der Berg. Advances in GPR data processing for anti-personnel landmine detection. *IEEE International Geoscience and Remote Sensing Symposium*, 1:19–22, 2000.

[82] P. Bhattacharya, H. Liu, A. Rosenfeld, and S. Thompson. Hough transform detection of lines in 3-d space. *Pattern Recognition Letters*, 21:843–849, 2000.

[83] J. Mao and A. Jain. Artificial neural networks for feature extraction and multivariate data data projection. *IEEE Transactions on Neural Networks*, 6:296-317, 1995.

[84] Geo-Services International (UK) Ltd. Confidential data, ref.743,745. 2001.

[85] L. Stergioulas. *Time-Frequency Methods in Optical Signal Processing.* PhD thesis, University of Liverpool, 1997.

[86] B. Barkat, A. Zubir, and C. Brown. Application of time-frquency techniques for the detection of anti-personal landmines. *Proceedings of IEEE workshop on statistical signal and array (CAT No.OOJH8496)*, pages 594–597, 2000.

[87] L. Cohen. Time-frequency distributions-a review. *Proceedings of IEEE workshop on statistical signal and array (CAT No.OOJH8496)*, pages 594–597, 2000.

[88] E. Wigner. on the quantum correction for thermodynamic equilibrium. *Physical Review*, 40:749–759, 1932.

[89] E. Wigner. Quantum mechanical distribution functions revisited. *Perspectives in Quantum Theory, MIT Press*, pages 25–36, 1971.

[90] J. Ville. Theory and applications of the notion of complex signal. *Cables and Transmissions*, 2A:61–74, 1948.

[91] H. Brunzell. *Signal Processing Techniques for Detection of Buried Landmines Using Ground-Penetrating Radar.* PhD thesis, Chalmers University of Technology, Sweden, 1998.

[92] Mathworks. *Matlab Signal Processing Toolbox User's Guide, Version 5.* The Math Works Inc., USA, 2000.

[93] Mathworks. *Matlab Neural Network Toolbox User's Guide.* The Math Works Inc., USA, 1998.

[94] A. Cichoki and R. Unbehauen. *Neural Networks for Optimisation and Signal Processing.* John Wiley Sons, UK, 1993.

[95] E. Azzouz and A. Nandi. *Automatic Modulation Recognition of Communication Signals.* Kluwer Acadimic Publishers, USA, 1996.

[96] S. Mitra. *Digital Signal Processing, A computer-Based Approach.* McGraw-Hill, Singapore, 2001.

[97] Mathworks. *Statistics Toolbox For Use With Matlab.* The Math Works Inc., USA, 2000.

[98] S. Marchnd-Maillet and Y. Sharaiha. *Binary Digital Image Processing A Discrete Approach.* Academic Press, UK, 2000.

[99] I. Pitas (Editor). *Parallel Algorithms For Digital Image Processing Computer Vision and Neural Networks.* John Wiley Sons, England, 1993.

[100] A. Godrdon. *Classification.* Chapman and Hall/CRC, USA, 1999.

[101] G. Ritter and J. Wilson. *Handbook of Computer Vision Algorithms in Image Processing.* CRC Press Inc., USA, 1996.

[102] I. Pitas. *Digital Image Processing Algorithms.* Prentice Hall, UK, 1993.

[103] H. Strifors, A. Guasafsson, and G. Gaunaurd. A fuzzy cluster representation of time-frequency signatures as a means for classification of targets burried underground. *SPIE*, 3069:26–36, 1997.

[104] J. Aaltonen and J. Nissen. Geological mapping using *GPR* and *differential* GPS positioning: a case study. *in Ninth International Conference on Ground Penetrating Radar, Steven K. Koppenjan and Hua Lee, Editors, Proceedings of SPIE*, 4758:207–210, 2002.

[105] Mathworks. *Image Processing Toolbox For Use With Matlab.* The Math Works Inc., USA, 2001.

[106] Haykin and Simon Saher. *Neural networks : a comprehensive foundation.* Prentice Hall, London, 2nd edition, 1999.

[107] J. Freeman. *Neural networks: algorithms, applications, and programming techniques.* Addison-Wesley, 1991.

[108] H. Coxeter. *Introduction to Geometry.* Wiley, New York, 2nd edition, 1969.

[109] www.exploremath.com. Useful site containing a flash simulator of hyperbola.

[110] K. Kanatani. Statistical bias of conic fitting and renormalization. *IEEE Transaction on Pattern Analysis and Machine Intelligence*, 16(3):320–326, 1994.

[111] P. Rosin. A note on the least squares fitting of ellipses. *Pattern Recognition Letters*, 14:799–808, 1993.

[112] P. Sampson. Fitting conic sections to very scattered data: an iterative refinement of the bookstein algorithm. *Computer Graphics and Image Processing*, 18:97–108, 1982.

[113] S. Rao. *Optimization: Theory and Applications.* Wiley Estern, 2nd edition, 1984.

[114] G. Romeo, F. Mele, and A. Morelli. Neural networks and discrimination of seismic signals. *Computers and Geosciences*, 2:279–288, 1995.

[115] G. Markt. Subsurface characterization of hazardous waste sites using ground penetrating radar. *Second International Symposium on Geotechnical Applications of Ground Penetrating Radar*, pages 61–109, 1988.

[116] C. Balanis. *Antenna theory, analysis and design.* John Wiley sons Inc., USA, second edition, 1997.

[117] J. Kraus and R. Marhefka. *Antennas for all applications.* McGraw-Hill Higher Education, USA, third edition, 2002.

[118] P. O'Leary and P. Zsombor-Murray. Direct and specific least-square fitting of hyperbolae and ellipses. *Journal of Electronic Imaging*, 13(3):492–503, 2004.

[119] M. Azimisadjadi, D. Poole, S. Sheedvash, K. Sherbondy, and S. Stricker. Detection and classification of buried dielectric anomalies using a separated aperture sensor and a neural network discriminator. *IEEE Transactions on Instrumentation and Measurement*, 1(1):137–143, 1992.

[120] M. Azimisadjadi and S. Stricker. Detection and classification of buried dielectric anomalies using neural networks - further results. *IEEE Transactions on Instrumentation and Measurement*, 43(1):34–39, 1994.

[121] A. Balan and M. Azimisadjadi. Detection and classification of buried dielectric anomalies by means of the bispectrum method and neural networks. *IEEE Transactions on Instrumentation and Measurement*, 44(6):998–1002, 1995.

[122] S. Billings, H. Jamaluddin, and S. Chen. Properties of neural network with applications to modelling non-linear dynamical system. *International Journal Control*, 55(1):193–224, 1992.

[123] Y. Bissessur and R. Naguib. Neural networks for the detection of buried plant. Technical report, Dept. of Electrical Engineering, University of Newcastle, 1993.

[124] Y. Bissessur and R. Naguib. Neural networks for the detection of buried plant. *IEE Conference Publication*, 409:393–398, 1995.

[125] C. Chen. Applying and validating neural network technology for nondestructive evaluation of materials. *Proceedings of The IEEE International Conference on systems, Man and Cybernetics*, 3:1208–1209, 1989.

[126] L. Fausette. *Fundamentals of Neural Networks - Architectures, Algorithms and Applications.* Prentice Hall, 1994.

[127] F. Dowla, S. Taylor, and R. Anderson. Seismic discrimination with artificial neural networks: Preliminary results with regional spectral analysis. *Bulletin of Seismological Socieity of America*, 80(5):1346–1347, 1990.

[128] P. Dysart and J. Pulli. Regional seismic event classification at the noress array: Seismological measurements and the use of trained neural networks. *Bulletin of Seismological Socieity of America*, 80(6):1910–1933, 1990.

[129] J. Fitch, S. Lehman, F. Dowla, S. Lu, E. Johansson, and D. Goodman. Ship wake-detection procedure using conjugate gradient trained artificial neural networks. *IEEE Transactions on Geoscience and Remote Sensing*, 29(5):718–726, 1991.

[130] R. Gorman and T. Sejnowsky. Analysis of hidden units in a layered network trained to classify sonar targets. *Neural Networks*, 1:75–89, 1988.

[131] M. Gough. Space instrument neural network for real time data analysis. *IEEE Transactions on Geoscience and Remote Sensing*, 31(6):1264–1271, 1993.

[132] Y. Hara, R. Atkins, S. Yueh, R. Shin, and J. Kong. Application of neural networks to radar image classification. *IEEE Transactions on Geoscience and Remote Sensing*, 32(1):100–109, 1994.

[133] W. Jones and J. Hoskins. Back-propagation, a generalized delta learning rule. *Byte*, pages 155–162, 1987.

[134] B. Kosko. Constructing an associative memory. *Byte*, pages 137–162, 1987.

[135] J. Kruschke. Improving generalization in back-propagation networks with distributed bottlenecks. *IJCNN International Jt Conf Neural Network*, 1:443–447, 1989.

[136] J. Lee, R. C. Weger, S. K. Sengupta, and R. Welch. A neural network approach to cloud classification. *IEEE Transactions on Geoscience and Remote Sensing*, 28(5):846–855, 1990.

[137] T. Lee and A. Peterson. Adaptive vector quantization using a self-development neural network. *IEEE Journal on Selected Areas in Communications*, 8(8):1458–1471, 1990.

[138] R. Lippmann. An introduction to computing with neural nets. *IEEE ASSP Magazine*, pages 4–22, 1987.

[139] T. Molyneaux, S. Millard, J. Bungey, and J. Zhou. Radar assessment of structural concrete using neural networks. *NDT&E International*, 28(5):281–288, 1995.

[140] M. Maruyama, N. Tsuda, and K. Nakabayashi. A rule-embedded neural-network and its effectiveness in pattern-recognition with ill-posed conditions. *IEICE Transactions on Information and Systems*, E78d(2):152–162, 1995.

[141] J. Paola and R. Schowengerdt. Detailed comparison of backpropagation neural network and maximum-likelihood classifiers for urban land use classification. *IEEE Transactions on Geoscience and Remote Sensing*, 33(4):981–996, 1995.

[142] D. Patterson. *Artificial Neural Networks - Theory and Applications.* Prentice Hall, Singapore, 1996.

[143] M. Poulton, P. Sternberg, and C. Glass. Location of subsurface targets in geophysical data using neural networks. *Geophysics*, 57(12):1534–1544, 1992.

[144] M. Poulton, P. Sternberg, and C. Glass. Neural network recognition of subsurface em images. *Journal of Applied Geophysics*, 29:21–36, 1992.

[145] L. Rogers, F. Dowla, and V. Johnson. Optimal field-scale groundwater remediation using neural networks and the genetic algorithm. *Environmental Science and Technology*, 29(5):1145–1156, 1995.

[146] J. Ronald, R. Weger, S. Sengupta, and R. Welch. A neural network approach to cloud classification. *IEEE Transactions on Geoscience and Remote Sensing.*, 28(5):846–855, 1990.

[147] S. Serpico and F. Roli. Classification of multisensor remote-sensing images by structured neural networks. *IEEE Transactions on Geoscience and Remote Sensing*, 33(3):562–578, 1995.

[148] S. Shoukry, D. Martinelli, S. Varadarajan, and U. Halabe. Radar signal interpretation using neural network for defect detection in concrete. *Materials Evaluation*, 54(3):393–397, 1996.

[149] J. Wang and T. Teng. Artificial neural network-based seismic detector. *Bulletin of Sesmological Society of America*, 85(1):308–319, 1995.

[150] J. Wang, C. Zhu, C. Wu, and Z. He. Neural network approaches to fast and low rate vector quantization. *Proceedings of the IEEE International Symposium on Circuits and Systems*, 1:486–489, 1995.

[151] P. Wong, T. Gedeon, and I. Taggart. Improved technique in porosity prediction: A neural network approach. *IEEE Transactions on Geoscience and Remote Sensing*, 33(4):971–980, 1995.

[152] Y. Zhou and X. Wu. Use of neural networks in the analysis and interpretation of site investigation data. *Computers and Geotechnics*, 16(2):105–122, 1994.

[153] H. Beck, D. Bergondy, J. Brown, and H. Sari-Sarraf. Multiresolution segmentation of forward looking ir and sar imagery using neural networks. *SPIE Intelligent Robots and Computer Vision IX*, pages 600–609, 1990.

[154] A. Bovik, M. Clark, and W. Geisler. Multichannel texture analysis using localized spatial filters. *IEEE Transactions on Pattern Analysis and Machine Intelligence*, 12(1):55–73, 1990.

[155] A. Brink. Thresholding of digital images using two dimensional entropies. *Pattern Recognition*, 25(8):803–808, 1992.

[156] D. Clausi and M. Jernigant. Towards a novel approach for texture segmentation of sar sea ice imagery. Technical report, Department of Systems Design Engineering, University of Waterloo, 1995.

[157] D. Clausi. *Texture Segmentation of SAR Sea Ice Imagery.* PhD thesis, University of Waterloo, 1996.

[158] M. Comer and E. Delp. Parameter estimation and segmentation of noisy or textured images using the em algorithm and mpm estimation. *Proceedings of the International Conference on Image Processing*, pages 650–654, 1994.

[159] R. Conners and A. Harlow. A theoretical comparison of texture algorithms. *IEEE Transactions on Pattern Analysis and Machine Intelligence*, PAMI-2(3):204–222, 1980.

[160] K. Deguchi. Analysis of underground radar image using gen. ht tech. *Transactions of the Society for Instrumentation and Control*, 25(7):72–79, 1989. Japanese.

[161] L. Dragonette, D. Drumheller, C. Gaumond, D. Hughes, B. O'Connor, N. Yen, and T. Yoder. The application of two-dimensional signal transformations to the analysis and synthesis of structural excitations observed in acoustical scattering. *Proceedings of the IEEE*, 84(9):1249–1263, 1996.

[162] L. Du. Texture segmentation of sar images using localized spatial filtering.

International Geoscience and Remote Sensing Symposium IGARSS'90, 3:1983 1986, 1990.

[163] R. Dubes. How many clusters are best? - an experiment. *Pattern Recognition*, 20(6):645–663, 1987.

[164] A. El-Jaroudi, M. Redfern, L. Chaparro, and J. Furman. The application of time-frequency methods to the analysis of postural sway. *Proceedings of the IEEE*, 84(9):1312–1318, 1996.

[165] N. Fatemi-Ghomi. *Performance Measures for Wavelet-Based Segmentation Algorithms*. PhD thesis, University of Surrey, 1997.

[166] F. Farrokhnia. *Multi-Channel Filtering Techniques for Texture Segmentation and Surface Quality Inspection*. PhD thesis, University of Michigan, 1991.

[167] J. Fouques and P. Cohen. Partition filters : A new class of morphological operators for segmenting textured images. *Proceedings of International Conference on Acoustics, Speech and Signal Processing*, 3:1707–1710, 1989.

[168] G. Gaunaurd and H. Strifors. Signal analysis by means of time-frequency (wigner-type) distributions-applications to sonar and radar echoes. *Proceedings of the IEEE*, 84(9):1231–1248, 1996.

[169] J. Haddon and J. Boyce. Texture classification of segmented regions of flir images using nural networks. *Proceedings of the International Conference on Image Processing*, pages 660–664, 1994.

[170] R. Haralick, K. Shunmugam, and I. Dinstein. Textural features for image classi-

fication. *IEEE Transactions on Systems Man Cybernetics*, SMC-3(1):610–621, 1973.

[171] R. Haralick. Statistical and structural approaches to texture. *Proceedings of the IEEE*, 67(5):786–804, 1979.

[172] D. He and L. Wang. Texture feature extraction from texture spectrum. *International Geoscience and Remote Sensing Symposium IGARSS'90*, 3:1987–1990, 1990.

[173] D. He and L. Wang. Textural filters based on the texture spectrum. *Pattern Recognition*, 24(12):1187–1195, 1991.

[174] K. Huang, K. Fu, T. Sheen, and S. Cheng. Image processing of seismograms: (a) hough transformation for the detection of seismic patterns; (b) thining processing in the seismogram. *Pattern Recognition*, 18(6):429–440, 1985.

[175] J. Illingworth and J. Kittler. A survey of the hough transform. *Computer Vision, Graphics and Image Processing*, 44:87–116, 1988.

[176] A. Jain. A fast karhunen-loeve transform for a class of random processes. *IEEE Transactions on Communications*, 24(9):1023–1029, 1976.

[177] A. Jain and R. Dubes. Feature definition in pattern recognition with small sample size. *Pattern Recognition*, 10:85–97, 1978.

[178] A. Jain, F. Farrokhnia, and D. Alman. Texture analysis of automotive finishes. *Technical Report MS90-587*, Machine Vision Association, SME, Michigan, 1990.

[179] A. Jain and F. Farrokhnia. Unsupervised texture *segmentation* using gabor filters. *Pattern Recognition*, 24(12):1167–1186, 1991.

[180] G. Jang. A comparison of neural network performance for seismic phase identification. *Journal of the Franklin Institute*, 330(3):505–524, 1993.

[181] E. Johansson. Three-dimensional ground penetrating radar imaging using synthetic aperture time domain focusing. *SPIE*, 2275:205–214, 1995.

[182] T. Kaneko. Radar image processing for locating underground linear objects. *IEICE Transactions on Communications*, E-74(10):3451–3458, 1991.

[183] A. Laine and J. Fan. Texture classification by wavelet packet signatures. *IEEE Transactions on Pattern Analysis and Machine Intelligence*, 15(11):1186–1191, 1993.

[184] J. Lee and W. D. Philpot. A spectral-textural classifier for digital imagery. *International Geoscience and Remote Sensing Symposium IGARSS'90*, 3:2005–2008, 1990.

[185] S. Livens, P. Scheunders, G. Van de Wouwer, and V. Dyck. Wavelets for texture analysis. Technical report, Department of Physics, University of Antwerp, 1997.

[186] S. Livens. *Image Analysis For Material Characterisation (Corrosion Characterisation)*. PhD thesis, University of Antwerp, 1998.

[187] S. Madiraju and C. Liu. Rotation invariant texture classification using covariance. *Proceedings of the International Conference on Image Processing*, pages 655–659, 1994.

[188] P. Meaney, K. Paulsen, A. Hartov, and R. Crane. An active microwave imaging-system for reconstruction of 2-d electrical property distributions. *IEEE Transactions on Biomedical Engineering*, 42:1017–1026, 1995.

[189] Y. Michiguchi. Advanced subsurface radar system for imaging buried pipes. *IEEE Transactions on Geoscience and Remote Sensing*, 26:733–739, 1988.

[190] Y. Nagashima. Underground radar system utilising pattern recognition in the frequency domain. *SPIE*, 1360:1671–1681, 1990. Visual Communications and Image processing.

[191] N. Osumi and K. Ueno. Microwave holographic imaging method with improved resolution. *IEEE Transactions on Antennas and Propagation*, 33(2):152–159, 1985.

[192] N. Osumi and K. Ueno. Microwave holographic imaging method with improved resolution. *IEEE Transactions on Antennas and Propagation*, AP-32(10):1018–1026, 1994.

[193] P. Palisson, N. Zegadi, F. Peyrin, and R. Unterreiner. Unsupervised multiresolution texture segmentation using wavelet decomposition. *Proceedings of the International Conference on Image Processing*, pages 625–629, 1994.

[194] G. Ravichandran and M. Trivedi. Texture segmentation using circular-mellin operators. *Proceedings of the International Conference on Image Processing*, pages 635–639, 1994.

[195] T. Reed and H. Wechsler. Segmentation of textured images and gestalt organization using spatial/spatial-frequency representations. *IEEE Transactions on Pattern Analysis and Machine Intelligence*, 12(1):1–12, 1990.

[196] J. Ruiz del Solar and M. Koppen. Automatic generation of oriented filters for

texture segmentation. *Proceedings of the International Workshop on Neural Networks For Identification*, pages 212–220, 1996.

[197] J. Starck, Murtagh, and A. Bijaoui. *Image Processing and Data Analysis*. Cambridge University, 1998.

[198] K. Thyagarajan and T. Nguyen. A maximum likelihood approach to texture classification using wavelet transform. *Proceedings of the International Conference on Image Processing*, pages 640–644, 1994.

[199] M. Unser. Texture classification and segmentation using wavelet frames. *IEEE Transactions on Image Processing*, 4(11):1549–1560, 1995.

[200] G. Van De Wouwer. *Wavelets For Multiscale Texture Analysis*. PhD thesis, University of Antwerp, 1998.

[201] P. Vautrot, N. Bonnet, and M. Herbin. Comparative study of different spatial/spatial-frequency methods (gabor filters, wavelets, wavelets packets) for texture segmentation/classification. *Proceedings of the International Conference on Image Processing*, 3:145–148, 1996.

[202] T. Weldon and W. Higgins. Multiscale rician approach to gabor filter design for texture segmentation. *Proceedings of the International Conference on Image Processing, IEEE Computer Society Press*, pages 620–624, 1994.

[203] W. Williams. Reduced interference distributions: Biological applications and interpretations. *Proceedings of the IEEE*, 84(9):1264–1280, 1996.

[204] A. Whitney. A direct method of nonparametric measurement selection. *IEEE Transactions on Computers*, 20:1100–1103, 1971.

[205] H. Yin and N. Allinson. Self-organised parameter estimation and segmentation of mrf model-based texture images. *Proceedings of the International Conference on Image Processing, IEEE Computer Society Press*, pages 645–649, 1994.

[206] Y. Zhou and H. Longbotham. Texture segmentation by symmetric and asymmetric filters. *Proceedings of the International Conference on Image Processing, IEEE Computer Society Press*, pages 630–634, 1994.

[207] M. Sonka, V. Hlavac, and R. Boyle. *Image Processing, and Machine Vision.* Brooks/Cole Publishing Company, 2nd edition, 1999.

[208] A. Kesidis and N. Papamarkos. A windows-based inverse hough transform. *Pattern Recognition*, 33:1105–1117, 2000.

[209] J. Illingworth and J. Kittler. The adaptive hough transform. *IEEE Transactions on Pattern Pnalysis and Machine Intelligence*, 9(5):690–697, 1987.

Appendices

Appendix A

GSSI SIR® -2 Specifications

Following are the detailed specifications of Geophysical Survey Systems Inc. Surface Impulse Radar System 2 [1]:

Hardware

Radar Processor	Motorola DSP 56002
Display	21cm 640x480 Color Active Matrix LCD VGA for real-time display
CPU	80486 DX
Memory	16 Mbyte RAM
Hard Drive	Up to 450 Mbyte internal IDE
Input/Output	Antenna Input (including survey wheel) Fiber Optic Transmit Trigger Parallel: 12 V DC Input, 3 LED Indicators, Multi-Function Connector: RS-232, VGA, Keyboard, NTSC/PAL Video (optional)
Printer	Optional thermal plotter for real-time or playback hard copy of wiggle plot or gray scale line scan data

Electrical

Antennae	Operates all GSSI surface and air-coupled antennae: DIPOLES: Unshielded: 15, 20, 30, 40,80, 120 MHz Shielded: 100, 200, 300, 400, 500, 900, 1000 MHz Monostatic: 80, 100, 120, 300, 500, 900, 1000 MHz Bistatic: 15, 20, 30, 40, 80, 100, 120, 300 MHz TEM HORNS: 1.0 GHz, 2.5 GHz (bistatic, unshielded)
Dynamic Range	24 bit (144 dB unstacked)
A/D Conversion	8 or 16 bit
Input Power	12 VDC (3 Amp or 36 Watts)

Mechanical

Dimensions	29 x 27 x 14 cm WEIGHT: 6.3 kg

Operational

Temperature	0° C to +40° C (operating), -25° C to +60° C (storage)
Humidity	0-100% (RH)
Environmental	Radar control unit is environmentally sealed. Can be used in inclement weather.

Software

Data Collection	Continuous profiling with manually or survey wheel-emplaced horizontal reference marks. Point stacking either during continuous collection by stacking sequential scans or in stationary point collection mode
Display Mode	User selected: color/gray scale line scan, wiggle plot or oscilloscope formats
Range Gain	100 dB automatic or user selected; range gain prior to digitisation for maximum system dynamic range
Filters	Automatic or user selected vertical and horizontal filtering in real-time or post-acquisition processing
Stacking	Automatic or user selected
Transmit Rate	Automatic or user selected up to 64 KHz
Scan Rate	Automatic or user selected, 8 to 64 scans per second
Sampling	Automatic or user selected, 128, 256, 512, 1024, 2048 samples/scan
Range	Automatic or user selected: 5 to 2000 nanoseconds
Data Transfer	Through parallel port to PC with bi-directional parallel port
Post Processing	Optional RADAN software can be installed for additional post processing and color printing

Appendix B

Geophysical Test Site Description

The EIGG, a fully constituted Specialist Group of the Geological Society of London, maintains a Shallow Geophysics test site at Leicester, in conjunction with the Geology Department at the University of Leicester. It's purpose is to provide a facility for training, demonstrations, calibration and research for many aspects of shallow geophysical surveys and methods. Following is the description of the test site provided by the Geology Department on their web page [49].

Description

The test site lies on the summit of a gentle hill-top. The surface layer of topsoil is about 0.3 meters thick, grading down into Boulder Clay. The Boulder Clay is uniform throughout the site, containing clasts up to 200 mm set in a clay matrix. This unit is 16 to 18 meters thick, and underlain by Liassic clays and limestones. Offset Wenner

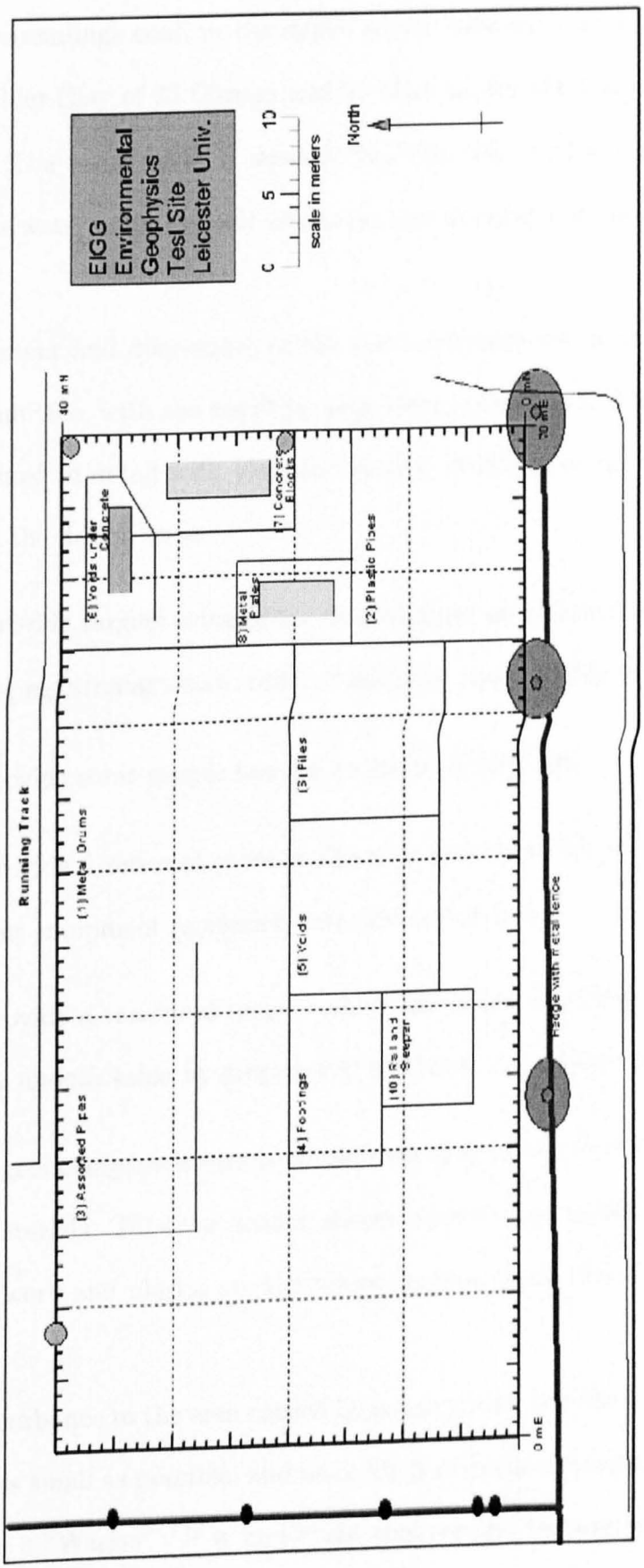

Figure B.1: Map showing test site layout

resistivity soundings confirm the depth to the boundary, and give a bulk resistivity of the Boulder Clay of 23 Ohm.m and 25 Ohm.m. for the Liassic Clay and limestone sequence. The water table is shallow, but the clay is of low permeability. During excavations water seeped slowly into most pits at depths of about 2 meters below the surface.

The content and disposition of the test structures was discussed in detail by the EIGG committee, with the resulting plan being as shown in Figure B.1. Each structure is defined in detail with plan and section drawings as necessary. Major considerations in the design were:

- To provide targets suitable for most shallow geophysical methods such as magnetics, electromagnetics, radar, resistivity and possibly gravity and seismics.
- To provide some simple targets for training purposes.
- To provide a series of more challenging targets which would test the limits of present equipment resolution and field techniques.
- To provide a variety of targets which are of practical importance, but are currently undetectable by geophysical methods, e.g. plastic pipes.

The targets comprise a variety of different shapes and sizes of objects made from different materials. Tubes or beams, sheets, spheres and cubes, made of metal, concrete, brickwork and plastic are the major targets. Sizes range from 0.3 meters to 2 meters.

The disturbance to the area caused by constructing the site was minimised. Burial holes were as small as possible, and back-filled with the extracted materials and compacted with a "Wacker". It is important that we can be sure that our measurement

responses come from the buried objects, and not from the ground disturbance caused around them. To this end some trenches are back-filled with different materials (e.g. gravel, mixed ((homogenised) extracted subsoil)) to act as controls. For practical reasons as well as to contain disturbance no excavation was deeper than 3 meters. Some soil compaction has occurred due to movement of plant. Continued maintenance may be necessary to level any further subsidence and ensure a uniform level surface with even grass cover..

Technical Description of Target Objects

Brief details of the objects present at the site. Actual users of the site can obtain detailed drawings of the areas on which they have worked. No objects are buried to depths of greater than 2 meters to their top surface.

Area 1 Metal Drums Simulation of buried waste drums. Metal waste disposal containers, and other similar objects buried from 0.5 to 2.0 meters, infilled with air or water.

Area 2 Plastic Pipes Simulation of Gas and water mains. Standard high-pressure pipes laid in trenches with back-fill of aggregates as standard for actual pipes. A real 2 inch Asbestos main also crosses this area.

Area 3 Metal and Clay Pipes Buried in cut trenches backfilled with excavated materials, not aggregates. Details of the buried pipes and their orientations may be found in Figure B.2 and Table B.

Area 4 Buried Walls and Trenches Simulation of various wall foundations and trench fills consisting of: modern concrete, corbelled brick, stone, aggregate, sand, and

peat.

Area 5 Voids Simulation of air-filled voids underground. These consist of plastic waste disposal canisters filled as appropriate and sealed. Metal clips for the lids were not fitted.

Area 6 Area 6. Simulated Piles This area has not been constructed to date. It will be built when a drill-rig comes on site to drill the control boreholes. As yet there is no definite date for this.

Area 7 Area 7. Concrete in pits Simulation of isolated blocks in trench. Concrete blocks cast in situ in a battered trench with aggregate infill.

Area 8 Area 8. Metal plates in pits. Determination of resolution of multiple buried metal objects. 6 metal plates buried in a stair-case pattern along the axis of an aggregate-filled trench 6 m long, 2 m wide and 2 m deep.

Area 9 Voids under concrete ground slab Rectangular void spaces (lined with plastic casing) underlying concrete slab, partly reinforced with standard re-bar net.

Area 10 Simulated rail track A small section of light railway track consisting of one rail and two sleepers

Table B.1: Metal, plastic and clay pipes

I.D	Depth to top (m)	Diam (m)	Length (m)	Object type	Filling	Orientation
1	0.7	0.10	6.0	Cast iron or steel pipe 6m long	Any	Horizontal
2	0.7	0.05	6.0	Cast iron or steel pipe 6m long	Any	Horizontal
3	0.7	0.10	6.0	Cast iron or steel pipe 6m long	Any	Horizontal
4	0.7	0.05	6.0	Cast iron or steel pipe 6m long	Any	Horizontal
5	0.7	0.10	9.0	Clay pipes 9m long, socketed but not sealed	Any	Horizontal
6	0.7	0.100	6.4	Plastic gas main sealed end-caps	Air	Horizontal
7	0.7	0.05	6.0	Plastic gas supply pipe sealed	Air	Horizontal

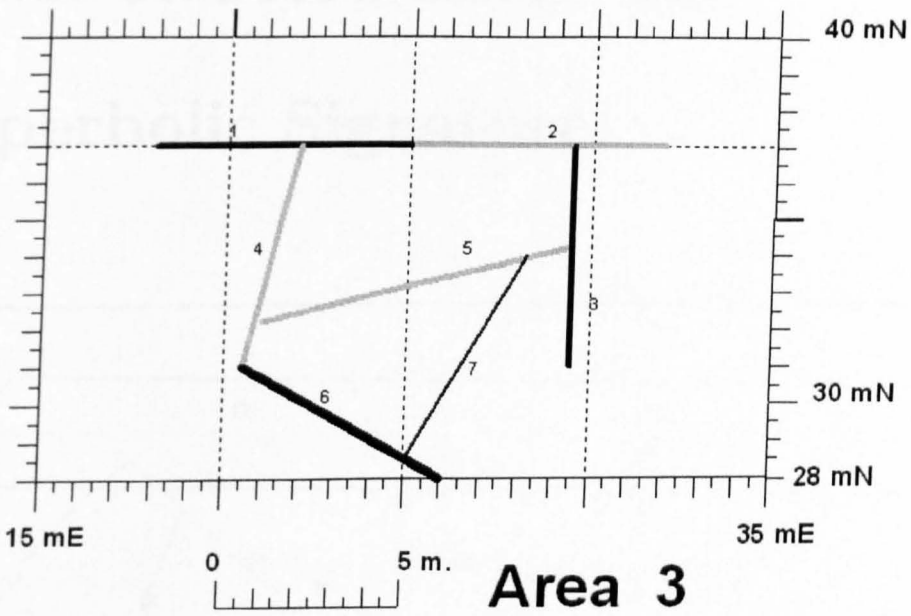

Figure B.2: Site plan of Area 3 showing layout of pipes

Appendix C

Effect of Orientations on Hyperbolic Signature

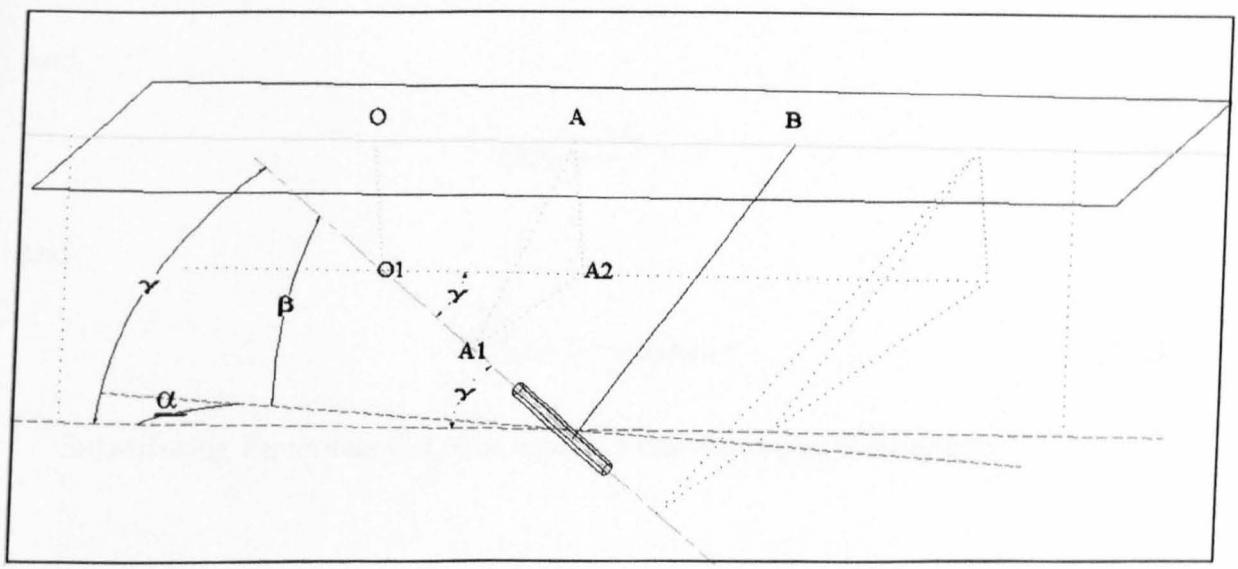

Figure C.1: 3D presentation of a buried cylinder with azimuth and vertical orientations

Figure C.1 shows a subsurface cylinder of radius R in 3D-space with an azimuth orientation angle α and vertical inclination angle β.

From Figures C.1 and C.2, from the right-angled triangle AA_1A_2:

$$(AA_1)^2 = (A_1A_2)^2 + (AA_2)^2 \tag{C.1}$$

where

$$AA_1 = Z + R \tag{C.2}$$

$$AA_2 = OO_1 = Z_0 + R \tag{C.3}$$

since $Z = \frac{vt}{2}$ then:

$$AA_1 = \frac{vt}{2} + R \tag{C.4}$$

and

$$OO_1 = \frac{vt_0}{2} + R \tag{C.5}$$

and

$$A_1A_2 = (x - x_0)\sin\gamma \tag{C.6}$$

Substituting Equations C.4, C.4, and C.4 into Equation C.1 tog get:

$$\left(\frac{vt}{2} + R\right)^2 = \left(\frac{vt_0}{2} + R\right)^2 + ((x - x_0)\sin\gamma)^2 \tag{C.7}$$

Manipulating Equation C.7 leads to:

$$\left(\frac{t + \frac{2R}{v}}{t_0 + \frac{2R}{v}}\right)^2 - \left(\frac{(x - x_0)\sin\gamma}{\frac{v}{2}t_0 + R}\right)^2 = 1 \tag{C.8}$$

It was shown in Chapter 4 that the relation between α, β, and γ is:

$$\cos\gamma = \cos\alpha\cos\beta \tag{C.9}$$

In the special case when $\alpha = 0$, then this means that the three points: A, A_1, and A_2 are aligned do not form a triangle anymore. Consequently, the relation in Equation C.1 is not valid. Instead the new assumption will be:

$$AA_1 = A_1A_2 + AA_2 \tag{C.10}$$

Substituting for the values of AA_1, AA_2, and A_1A_2 leads to:

$$\frac{vt}{2} + R = \frac{vt_0}{2} + R + (x - x_0)\sin\gamma \tag{C.11}$$

Since $\alpha = 0$ then $\gamma = \beta$, with manipulation, then Equation C.11 becomes:

$$t = \frac{2}{v}(x - x_0)\sin\beta + t_0 \tag{C.12}$$

It can be seen that Equation C.12 is of a straight line, which means that the resulting signature will not be hyperbolic and hence will not be detected as a target.

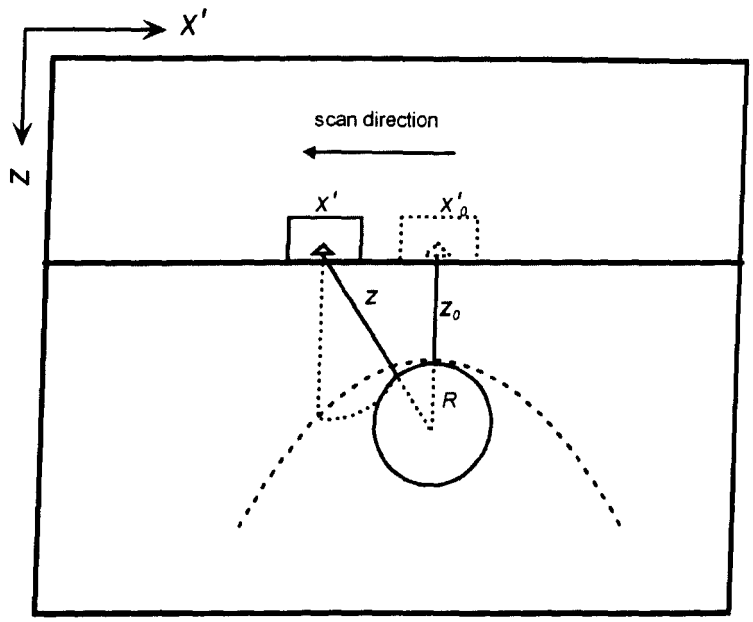

Figure C.2: Side view of the buried cylinder in Figure C.2

Appendix D

GSSI SIR® File Format

GSSI radar systems are stored in binary as a binary block of data preceded by a file header containing information about the site, the data acquisition settings, the system configuration and on-board processing parameters. The detailed format of the header structure for these files, which are given the extension *.dzt*, is given below in Tables D.1 and D.2, as published by GSSI in the RADAN®processing software manual [1]. If tightly packed, the header portion will occupy 1024 bytes (1 kilobyte) of memory.

Table D.1: DZT Date Structure

Data type	Field name			Description
unsigned	sec2	:	5	Second/2 (0-29)
unsigned	min	:	6	Minute (0-59)
unsigned	hour	:	5	Hour/2 (0-23)
unsigned	month	:	5	Day/2 (1-31)
unsigned	year	:	4	Year-1980(0-127)

Table D.2: DZT Header Structure

Data type	Field name	Description
unsigned short	dzt_hdr_id	OxOOFF if header
unsigned short	offset_to_data	Offset to data in bytes (1024)
unsigned short	samples_per_scan	Samples per scan
unsigned short	bits_per_sample	Bits per data word
unsigned short	amp_midpoint	Offset to data mid-point
float	scans_per_second	Scans per second
float	scnas_per_metre	Scans per meter
float	metres_per_mark	meters per mark
float	start_time_offset	Position (ns)
float	total_time_range	Range (ns)
unsigned short	number_passes	Number of passes for 2D files
long	create_date	Creation date and time
long	modified_date	Last modification date and time
unsigned short	offset_to_gain	Offset to range gain function
unsigned short	sizeof_rgain	Size of range-gain function
unsigned short	offset_to_text	Offset to text
unsigned short	sizeof_text	Size of text
unsigned short	offset_proc_hist	Offset to processing history
unsigned short	sizeof_proc_hist	Size of processing history
unsigned short	number_of_channels	Number of channels
float	ave_rel_diel_perm	Average dielectric constant
float	top_in_metres	Top position in metres
float	range_in_metres	Range in metres
char	reserved	Reserved
unsigned short	scans_per_pass	Scans per pass
unsigned short	line_num	line number
unsigned short	start_x	Initial line number
unsigned short	start_y	Initial station number
unsigned short	end_x	Final line number
unsigned short	end_y	Final station number
character	dtype	Data type
character	antenna	Antenna name
unsigned short	channel_mask	Active channel mask
integer	checksum	Checksum for header
character	variable	Range gain, comments & history

Appendix E

Dielectric Characteristics

The velocity of electromagnetic wave propagation is governed by the electrical permittivity of the medium material, which depends primarily upon its water content. Over the range of frequencies over which GPR operates, water has a relative permittivity ϵ_r of approximately 80, while the solid constituents of most soils have dry relative permittivities between 2 and 9. Although these permittivities vary to an extent with frequency, they remain relatively constant for most materials in the microwave frequency range. Table E.1 shows the conductivity and relative permittivity of a number of common materials, measured at 100 MHz [2, 115].

Table E.1: Typical range of dielectric characteristics of various materials

Material type	**Conductivity (S/m)**	**Relative permittivity**[§]
Air	0	1
Asphalt, dry	$10^{-3} - 10^{-2}$	$2 - 4$
Asphalt, wet	$10^{-2} - 10^{-1}$	$6 - 12$
Clay, dry	$10^{-3} - 10^{-2}$	$2 - 6$
Clay, saturated	$10^{-1} - 1$	$15 - 40$
Coal, dry	10^{-2}	3.5
Coal, wet	10^{-1}	8
Concrete, dry	$10^{-3} - 10^{-2}$	$4 - 10$
Concrete, wet	$10^{-2} - 10^{-1}$	$10 - 20$
Freshwater	$10^{-4} - 10^{-2}$	81
Freshwater ice	10^{-3}	4
Granite, dry	$10^{-8} - 10^{-6}$	5
Granite, wet	$10^{-3} - 10^{-2}$	7
Limestone, dry	$10^{-9} - 10^{-6}$	7
Limestone, wet	$10^{-2} - 10^{-1}$	8
Permafrost	$10^{-5} - 10^{-2}$	$4 - 8$
Rock salt, dry	10^{-4}	$4 - 7$
Sand, dry	$10^{-7} - 10^{-3}$	$4 - 6$
Sand, saturated	$10^{-4} - 10^{-2}$	$10 - 30$
Sandstone, dry	$10^{-9} - 10^{-6}$	$2 - 3$
Sandstone, wet	$10^{-5} - 10^{-6}$	$5 - 10$
Seawater	4	81
Seawater ice	$10^{-2} - 10^{-1}$	$4 - 8$
Shale, saturated	$10^{-2} - 10^{-1}$	$6 - 9$
Snow, firm	$10^{-6} - 10^{-5}$	$8 - 12$
Soil, sandy, dry	$10^{-4} - 10^{-2}$	$4 - 6$
Soil, sandy, wet	$10^{-2} - 10^{-1}$	$15 - 30$
Soil, loamy, dry	$10^{-4} - 10^{-3}$	$4 - 6$
Soil, loamy, wet	$10^{-2} - 10^{-1}$	$10 - 20$
Soil, clayey, dry	$10^{-4} - 10^{-1}$	$4 - 6$
Soil, clayey, wet	$10^{-1} - 1$	$10 - 15$

§ The permittivity of free-space, $\epsilon_0 = 8.854 \times 10^{-12}\,\mathrm{Fm}^{-1}$